2011

DEVELOPMENTAL REMODELING OF RELAY CELLS IN THE DORSAL LATERAL GENICULATE NUCLEUS (dLGN) OF THE MOUSE AND THE ROLE OF RETINAL INNERVATION

Rana El-Danaf
Virginia Commonwealth University

DEVELOPMENTAL REMODELING OF RELAY CELLS IN THE DORSAL LATERAL GENICULATE NUCLEUS (dLGN) OF THE MOUSE AND THE ROLE OF RETINAL INNERVATION

A dissertation submitted in partial fulfillment of the requirements for the degree of Doctor of Philosophy at Virginia Commonwealth University.

By

Rana El-Danaf
Bachelor of Science
Virginia Commonwealth University, 2006
Master of Science
Virginia Commonwealth University, 2008

Director: William Guido, Ph.D.
Professor, Department of Anatomy and Neurobiology

Virginia Commonwealth University
Richmond, Virginia
September, 2011

Acknowledgments

I would like to thank my advisor Dr. William Guido for accepting me as a student in his laboratory. For the past four years, Dr. Guido was very patient and taught me valuable lessons. His advice and encouragement made the completion of this research possible. I would like to thank Dr. Jason Chen for accepting to serve as a member of my advisory committee, as well as for allowing me to use his laboratory resources. I would like to extend my gratitude to Dr. Michael Fox for all his help with genotyping, immunohistochemistry and RT-PCR analysis and for accepting to serve as a member of my advisory committee. I would like to thank Dr. Scott Henderson for training me and teaching me techniques in 3-dimensional cellular imaging as well as the use of Volocity software. In addition, I would like to thank him for being a member of my committee. I would like to thank Dr. Babette Fuss for accepting to be a member of my advisory committee. I would like to thank Dr. Steve Wang for providing the *math5*-null mice and Dr. Martha Bickford for the EM analysis.

I would also like to acknowledge all the past and present members of the Guido lab. I want to thank Dr. Thomas Krahe for always being ready to help whenever I had any problems or questions, especially with electrophysiology and statistical analysis. More importantly, I want to thank him for recording and filling cells in the WT mouse, an essential part of this study. I would also like to thank Dr. Emily Dilger and Tania Seabrook for all their help, support and

advice throughout these years. I would also like to thank Dr. Chris Jurgens who recently joined the lab.

I would like to thank Dr. Jianmin Su and Dr. Frank Chen for all their help and advice in genotyping and PCR.

Most importantly, I would like to thank my parents Dr. Naja and Hind, my siblings Omar, Ghady and Reem, my grandmother Bariziah, my aunts Daad, Leila, Ghada, Ghunwa and Abir, and all my extended family and friends in the United States and Lebanon. They were always there for me. Their courage and support extended beyond the boundaries that separate us.

Lastly, I would like to dedicate this work to the memory of my grandfather Salim El-Danaf, who always encouraged me to aspire for the best in life. He was looking forward to my graduation, but unfortunately death took him away from us. I hope that he is proud of me. I also would like to dedicate this research to the memory of my cousin Imad "Eddie" El-Awar. They will never be forgotten.

TABLE OF CONTENTS

LIST OF TABLES

LIST OF FIGURES

LIST OF ABBREVIATIONS

BDNF	Brain-derived neurotrophic factor
bHLH	Basic helix-loop-helix
ChAT	Cholinergic acetyl transferase
CTB	Cholera toxin subunit B
dLGN	Dorsal lateral geniculate nucleus
DO*i*	Dendritic orientation index
E	Embryonic day
EPSP	Excitatory postsynaptic potential
GABA	γ-aminobutyric acid
GCL	Ganglion cell layer
GFP	Green fluorescent protein
INL	Inner nuclear layer
ISI	Interstimulus interval
LTS	Low-threshold calcium spike
NRT	Thalamic reticular nucleus
NMDA	N-methyl-D-aspartate- type
ONL	Outer nuclear layer
ORN	Olfactory receptor neurons
P	Postnatal day
PBS	Phosphate buffer solution
PFA	Paraformaldehyde
PN	Projection neurons
PPR	Paired-pulse ratio
RGC	Retinal ganglion cell
RLP	Round vesicles, large profile, pale mitochondria
RSD	Round vesicles, small profile, dark mitochondria
RLD	Round vesicles, large profile, dark mitochondria
RT-PCR	Reverse transcription polymerase chain reaction
SCN	Suprachiasmatic nucleus
τ	Tau
trk	Receptor tyrosine kinase
TTX	Tetrodotoxin
VCN	Ventral cochlear nucleus
VGluT2	Vesicular glutamate transporter2
vLGN	Ventral lateral geniculate nucleus
WT	Wild-type

Abstract

DEVELOPMENTAL REMODELING OF RELAY CELLS IN THE DORSAL LATERAL GENICULATE NUCLEUS (dLGN) OF THE MOUSE AND THE ROLE OF RETINAL INNERVATION

By Rana El-Danaf, M.S.

A dissertaion submitted in partial fulfillment of the requirements for the degree of Doctor of Philosophy at Virginia Commonwealth University.

Virginia Commonwealth University, 2011

Major Director: William Guido, Ph.D.

Professor, Department of Anatomy and Neurobiology

The dorsal lateral geniculate nucleus (dLGN) has become an important model for studying many aspects of visual system development. To date, studies have focused on the development of retinal projections and the role of activity in shaping the pattern of synaptic connections made with thalamocortical relay cells. By contrast, little is known about relay cells and the factors that regulate the growth and establishment of their dendritic architecture. In many systems, such growth seems consistent with the synaptotrophic hypothesis which states that synapse formation and dendritic growth work in a concerted fashion such that afferent input and the establishment of functional synapses are needed to shape the maturation of dendritic arbors. To address this,

we characterized the development of relay cells in the dLGN of wild-type (WT) mouse. By adopting a loss of function approach, we assessed the manner in which growth and maturation of relay cells were affected by retinal innervation. For this, we made use of the *math*-null (*math5*$^{-/-}$) mouse in which progenitors fail to differentiate into retinal ganglion cells (RGCs), and exhibit a ≥95% cell loss. Anterograde labeling of RGC axons with cholera toxin subunit B (CTB), immunolabeling of RGC-specific presynaptic machinery in dLGN (e.g. vesicular glutamate transporter 2), and ultrastructural analysis at the electron microscopy level demonstrated that the dLGN is devoid of retinal innervation. We examined the functional and morphological characteristics of relay cells in WT and *math5*-nulls during early postnatal life by conducting *in vitro* whole cell recordings in slices containing dLGN. Individual relay cells were labeled by intracellular injection of biocytin, and imaged by confocal microscopy to obtain the 3-D reconstructions of their dendritic trees. Morphometric analysis revealed that relay cells in WT undergo two growth spurts: an early one where cell class specification and dendritic complexity are established and a later one marked by an increase in dendritic field and length. Following the third week, relay cells growth was stabilized. In *math5*-nulls, relay cells maintained their morphological identity whereby cells could be classified in three groups (Y: spherical, X: bi-conical, W: hemi-spherical). However, the dLGN was highly reduced in size, and relay cells showed disrupted growth spurts. Relay cells had smaller somata and exhibited fluctuations in dendritic complexity and field extent compared to age-matched WTs. Exuberance in dendritic branching was noted in week 2, and by week 5, relay cells had significantly smaller surface area resulting from a loss of dendritic segments and a reduction in dendritic field extent. Control experiments using RT-PCR revealed that these changes were not due to the loss of *math5* in the dLGN. Whole cell recordings and voltage responses to square wave current pulses showed that

math5-nulls possess the full compliment of intrinsic membrane properties, such as relay cells displayed both burst and tonic firing modes. A cross of the *math5*-null with a transgenic mouse that expresses GFP in layer VI cortical neurons revealed a dense plexus of corticogeniculate terminals throughout the mature dLGN. However, the rate of corticogeniculate innervation was highly accelerated and was complete a week earlier than WT. Electric stimulation of cortical axons revealed that synapses are functional and responses were indistinguishable from WT. Taken altogether, these observations suggest that retinal innervation plays an important trophic role in the maturation of dLGN and is necessary for the continued maintenance of relay cells' structural integrity. However, the general form and function of relay cells seem largely unaffected by the loss of retinal innervation.

Introduction

The thalamus is an important structure that allows for the transmission of information from peripheral sense organs to the cortex. It consists of many modality specific nuclei, and perhaps the best studied is the visual relay, the dorsal lateral geniculate nucleus (dLGN) (see Sherman, 2005). It is a central visual structure that receives its primary driver input from the retina, but also input from the cortex, brainstem and thalamic reticular nucleus (NRT). The dLGN has been extensively investigated in carnivores and primates. However, with the advent of mouse transgenics, this species has emerged as a system of choice for exploring many aspects of visual system function and development (see Guido, 2008). For the latter, most of the focus has been directed towards understanding the mechanisms that lead to the formation and maturation of retinal projections and connections in the dLGN (see Huberman, 2007; Guido, 2008).

Retinal ganglion cells (RGCs) arising from the nasal and upper quadrant of the temporal retina, cross at the optic chiasm and terminate in the contralateral dLGN; whereas axons originating in the lower temporal retina terminate in the ipsilateral anterior medial sector of dLGN (Godement et al., 1984). Initially, projections from both eyes are diffuse, overlapping and share terminal space (Jaubert-Miazza et al., 2005). For example, between postnatal days (P) 3-7, there is around 57% overlap between ipsilateral and contralateral axons. However, an extensive period of refinement is noted between P8-10, whereby ipsilateral projections recede, sharing only 18% of the total area of dLGN with contralateral projections. Pruning continues so that by P14 -

the time of natural eye opening- retinal terminals are completely segregated into eye-specific domains, where contralateral and ipsilateral axons occupy around 90% and 10% of the total area of the dLGN, respectively. This refinement is accompanied by changes in the pattern of retinogeniculate connectivity (see Guido, 2008). During the first postnatal week, a single relay cell receives weak binocular inputs from as many as 10 different RGCs. However, many of these inputs are pruned so that by P14-21, a given relay cell receives only 2-3 inputs from one eye. The pruning of these connections is accompanied by the strengthening of the remaining ones (Chen and Regehr, 2000; Jaubert-Miazza et al, 2005; Žiburkus and Guido, 2006).

A crucial element of this pathway is the targets of RGCs, the relay cells of the dLGN. These cells play an important role in the relay of information between the retina and visual cortex. Up until recently, very little was known about relay cells morphological maturation in the mouse. Moreover, it remains unknown whether their growth is timed with respect to the arrival or the remodeling of retinogeniculate connections.

Preliminary studies from our lab examining the architecture of relay cells in the mouse showed that by P7 cells exhibit complex dendritic arbors that seem to resemble adult-like profiles (see Appendix I-Krahe and El-Danaf et al., 2011, submitted; El-Danaf and Krahe et al., 2009). This investigation identified the presence of three morphologically distinct cell types that displayed strong regional preferences in the dLGN. These were termed X-, Y- and W- cells because they bear a striking resemblance to those previously identified in the cat (Friedlander et al., 1981; Stanford et al., 1981, 1983). Y-cells have radially symmetric dendritic arbors and are found throughout the nucleus in a central band parallel to the optic nerve. X-cells have a bi-conical morphology and are located within the monocular segment of the dLGN, and W-cells have a hemispherical shape and are situated along the borders of the nucleus. Other reports also

showed that relay cells possess different voltage-gated membrane conductances that emerge during early postnatal life, and dictate how they integrate and transmit neuronal signals (MacLeod et al., 1997; Jaubert-Miazza et al., 2005; Dilger et al., 2011). Many of these properties, while present at birth, are somewhat immature, and their maturation is attained by the third postnatal week (MacLeod et al., 1997).

These structure-function relationships of relay cells were thoroughly studied in cat dLGN. These can be divided into three morphologically and physiologically separate cell types forming distinct parallel pathways that are essential for dissecting different aspects of the visual scene (Friedlander et al., 1981; Stanford et al., 1981, 1983). For example, moving stimuli are captured through the Y- pathway, while X- cells are important for analyzing details. In rodents, it was uncertain whether parallel channels exist. Recently, a host of transgenic mice permitted the identification of functionally distinct classes of RGCs each with unique central projections. For several classes of mouse RCCs, these transgenic lines revealed lamina-specific projections to dLGN, which correspond to the regional preferences of relay cells (Hattar et al., 2006; Huberman et al., 2008; Kim et al., 2008; Badea et al., 2009; Huberman et al., 2009; Siegert et al., 2009; Ecker et al., 2010; Kim et al., 2010; Kay et al. 2011; Rivlin-Etzion et al., 2011). These findings provided strong evidence supporting the presence of parallel pathways in the mouse visual system similar to the ones found in higher mammals. Taken together, relay cells appear to be structurally and functionally mature at early postnatal ages. Given the adult-like characteristics of these neurons, it seems that they provide a template for retinogeniculate remodeling. Nonetheless, the mechanisms that govern the functional and structural growth of relay cells remain largely unexplored.

The role that afferent inputs play in the development of their postsynaptic targets has been a subject of interest. The steps involved in the formation of functional synaptic connectivity include: axonal outgrowth, target selection and initial contact between growing axonal and dendritic processes, differentiation and recruitment of pre- and post-synaptic elements, and lastly synapse maturation and refinement (Fox and Umemori, 2006; Fox, 2008). Synapse formation has been thought to play a role in dendritic maturation. This idea is consistent with the synaptotrophic hypothesis (Vaughn, 1989; see Cline and Hass, 2008). It suggests that synapse formation and dendritic maturation occur in a concerted fashion, and that these pre- and post-synaptic interactions are necessary for shaping the features of the dendritic architecture of neurons. This hypothesis was proposed by Vaughn from his work on the developing neurons of the motor spinal cord (Vaughn et al., 1988; Vaughn, 1989). He reported that neurons direct their dendritic processes towards synaptically rich regions. He also noted that dendritic growth cones differentiate and acquire adult-like characteristics after making synaptic contacts with their afferent inputs. Other investigations have shown that key cellular events that have been implicated in the formation of functional synapses also influenced many aspects of dendritic tree growth, including initial elaboration and continued maintenance of their dendritic arbors, such as adhesion molecules, N-methyl-D-aspartate- type (NMDA) receptors, and calcium signaling (see Cline and Haas, 2008). For example, in the developing retinotectal system of the *Xenopus,* the blockade of NMDA receptors of immature tectal neurons with APV resulted in smaller dendritic fields and sparsely branched processes (Rajan and Cline, 1998). A more recent study in the same system combining *in vivo* time lapse imaging and electron microscopy showed that mature synapses were associated with stable dendritic processes (Li et al., 2011).

Interestingly, functional maturation and relay cell specification coincide with a dynamic period of retinal innervation, synaptogenesis and remodeling. During early postnatal life, retinal axons are the only terminals and exclusive source of synapses present in the dLGN (Godement et al. 1984; Jaubert-Miazza et al., 2005; Bickford et al., 2010; Seabrook et al., 2010). Studies have shown that RGCs target the dLGN at perinatal ages, whereby innervation from the contralateral retina starts at embryonic day (E) 16 and ipsilateral projections enter the nucleus at E21-P1 (Godement et al., 1984). There is also evidence of trophic support provided by retinal axons. For example, it has been shown that RGCs terminating in the dLGN release the brain derived neurotrophic factor (BDNF), which bind to their receptors localized on postsynaptic dendrites (see Cohen-Corry and Lom, 2004). Moreover, enucleation studies result in profound effects on dLGN, such as reduced size and distorted shape of the nucleus (Cullen and Kaiserman-Abramof, 1976; Heumann and Rabinowicz, 1980; Williams et al., 2002). Taken all together, this suggests that retinal innervation, synaptogenesis, and subsequent remodeling may be needed for the morphological and functional maturation of relay cells, as well as for the overall structural organization of the dLGN.

A number of studies have tried to examine the relationship between retinal input and relay cells development. However, results from these studies are open to interpretation largely because they were limited by the techniques employed to remove retinal input. In these, some of the methods included deafferentation of the optic nerve through postnatal enucleation or blockade of retinal activity by tetrodotoxin (TTX). In ferrets, early postnatal bilateral enucleation was performed (Sutton and Brunso-Bechtold, 1993). In this study, the timing of the manipulations seems inappropriate since it occurred 10 days after retinal axons had already innervated the dLGN. The enucleation was done too late and did not rule out the perinatal effects

of retinal innervation and synaptogenesis. Similar timing issue is apparent in a study done in fetal cats after blocking voltage gated Na^+ channels with TTX (Dalva et al., 1994). Although this was done prenatally, TTX was administered 9 days after RGCs axons had entered the dLGN (Shatz, 1983). Moreover, neurotransmitter release can occur spontaneously in the presence of TTX, which could potentially lead to postsynaptic activation of relay cells. In rodents, similar technical limitations were apparent. In the rat, retinal activity was blocked unilaterally with TTX through a long term treatment that began at P5 and relay cells dendrites were examined at P21 (Riccio et al., 1987). In the mouse, monocular enucleation was performed at birth and dendritic arborization was assayed at P31 (Brandes, 1971). As in the case of cats and ferrets, these manipulations were done after the arrival of RGC axons to the dLGN, which begins embryonically in the mouse (Godement et al., 1984). Additionally, differentiation of dLGN neurons begins at E13, and by birth these cells are remarkably complex (Angevine et al., 1970; see Appendix I- Krahe and El-Danaf et al., 2011, submitted). Furthermore, manipulations were monocular and did not rule out any compensatory interactions that could be provided by the intact eye. Moreover, the analyses did not survey the developmental time course of relay cells, since they were done at one specific time point. In general, these manipulations had minimal influence on relay cells development. Perhaps, the most substantial were those reported in ferrets after binocular enucleation which led to reduced soma size and a delay in the elimination of dendritic appendages. In order to examine the development of relay cells in the complete absence of retinal innervation, manipulations as the ones stated above cannot be employed in the mouse.

Perhaps the utility of the mouse model is to employ a genetic form of deafferentation. In part, the anophthalmic mouse (ZRDCT or eyeless) is the first example of how this could be used.

In this strain, there is an arrest in the growth of the optic vesicle at E10 which prevents the formation of an optic cup (Chase and Chase, 1941). As a result, 90% of animals in this strain exhibit bilateral eyelessness by E13, and have no optic nerve formation. In these mutants, the eyeless phenotype is a prime example of "multifactorial inheritance" in mice, which indicates that several genetic and environmental factors might play a role in the emergence of this trait (Tucker et al., 2001). In mice, one of the causes of anophthalmia was identified as a mutation in the homeobox gene *Rx/rax* (Tucker et al., 2001). Moreover, in human cases of anophthalmia, multiple genes were implicated such as *Pax6*, *Sox2*, *Otx2* and many others (Verma and Fitzpartick, 2007). Because multiple factors contribute to the etiology of this mutation, using these mice as an experimental tool to assess the role of retinal input in the development of relay cells is highly problematic. The genetic ambiguity would make it difficult to evaluate whether any changes at the level of relay cells growth would be a direct effect of the absence of retinal input or an indirect result of the unrelated genetic defects in this mutant.

To overcome these obstacles, we took advantage of a transgenic mouse model, the *math5*-null (*math5*$^{-/-}$) mutant. *Math5* is a murine basic helix-loop-helix (bHLH) gene that is expressed in the retina starting at E11 and is essential for the differentiation of retinal progenitor cells into RGCs (Brown et al., 1998). As a consequence, *math5*-nulls exhibit greater than 95% loss of RGCs (Wang et al., 2001; Brown et al., 2001; Moshiri et al., 2008). Reports show that retinal axons of surviving cells fail to form an optic nerve that project into the brain (Brown et al., 2001; Wee et al., 2002; Brzezinski et al., 2005). As a result, this form of genetic deafferentation will not expose the dLGN to retinal input, and precedes the timing when these normally enter the nucleus. These mice will provide a good model for assessing whether the maturation of relay cells relies on retinal innervation.

The objective of this study was to explore the development of relay cells in the dLGN of the mouse and whether their maturation requires retinal innervation. The early postnatal structural and functional characteristics of relay cells were studied in WT mouse, as well as in the complete absence of retinal innervation using *math5*-nulls. This was done with the use of *in vitro* whole cell patch clamp recording in thalamic slices of dLGN. Various protocols of current pulse injections were applied to assess the presence as well as the properties of various voltage-gated conductances. Following recording, intracellular injection of biocytin was made in order to visualize individual relay cells, and their 3-dimensional structure was obtained with confocal microscopy. Various morphometric characteristics were examined with the use of Volocity software. In addition to cellular maturation, overall structural organization of the dLGN may require retinal innervation and synaptogenesis. Analysis of the dLGN in terms of cytoarchitecture, area and cell density were made with the use of cresyl violet nissl stain.

Finally, we examined whether the absence of retinal innervation has an impact on the development of other non-retinal circuits in the dLGN. Relay cells receive and integrate signals from different brain regions. These inputs include feed-forward inhibition from dLGN intrinsic interneurons, feed-back inhibition from NRT, as well as cholinergic input from brainstem. The majority of the synapses made on relay cells arise through the feedback excitation from layer VI of visual cortex. The emergence of these inputs is delayed compared to retinogeniculate connectivity. Both anatomical and electrophysiological studies reveal that corticogeniculate, cholinergic, and intrinsic connections between interneurons and relay cells do not occur until the second postnatal week (Ballesteros et al., 2005; Bickford et al., 2010; Seabrook et al., 2010). This is the time when eye-specific segregation of retinal projections is complete, and cells

receive largely monocular input (see Guido, 2008). This suggests that retinal axons might be involved in controlling the non-retinal innervation of dLGN.

Our goal here was to begin to address these issues. The largest source of non-retinal input arises from the glutamatergic connections arising from layer VI of visual cortex (Bickford et al., 2010). Recently, Seabrook et al. (2010) detailed the course of corticogeniculate innervation to dLGN with the use of the transgenic mouse model *golli*-τ-GFP (Jacobs et al., 2007). In these mice, neurons from layer VI of the cortex express a τ -GFP fusion protein under the control of the *golli* promoter element of the myelin basic protein gene (Jacobs et al., 2007). This allows for tracing and studying corticofugal projections to different targets, including the dLGN. Using the same loss of function approach, we characterized the spatial extent, as well as functional connectivity of corticogeniculate projections by crossing *math5*-nulls with *golli*-τ-GFP transgenics. For this, we examined whether corticogeniculate innervation occurs in the absence of retinal innervation. We measured the spatial extent of corticogeniculate projections in the dLGN at different postnatal ages. Moreover, we tested whether functional connectivity exists between corticogeniculate axons and relay cells by measuring responses of individual relay cells to the electric stimulation of cortical afferents.

Methods and Materials

Subjects

All procedures were performed in compliance with the Institutional Animal Care and Use Committee at Virginia Commonwealth University. Mice ranging in age between the first and fifth postnatal weeks were studied. Three strains were used: pigmented wild-type mice (WT-C57/BL6), *math5*-nulls (math5$^{-/-}$) on a C57/BL6 background provided by S. Wang (Wang et al., 2001), *golli*-τ-GFP mice on a mixed background provided by C. Campagnoni and E.C. Jacobs (Jacobs et al., 2007). *Math5*-nulls/*golli*-τ -GFP mice were generated by crossing *math5*-nulls with the *golli*-τ-GFP transgenics. Mice resided in colonies at the VCU Medical Center.

Intravitreal eye injection

Injection of the anterograde tracer cholera toxin subunit B (CTB) was performed in order to visualize retinal projections in the dLGN (Jaubert-Miazza et al., 2005). Mice were anesthetized with isoflurane vapors. Using a glass pipette, the sclera was pierced near the ora serrata and excess vitreous fluid was drained. Using another glass pipette attached to a picospritzer, 3-8 µl of CTB (1.0% solution dissolved in distilled water) conjugated to Alexa Fluor 488 or 594 dyes (Invitrogen) were then injected into the same opening. Following eye injections, animals were given a 2-day survival period to allow the tracer to travel, reach the dLGN and effectively label axon terminals.

In vitro intracellular recording

Recordings were done using methods described elsewhere (Jaubert-Miazza et al., 2005; Bickford et al., 2010; Dilger et al., 2011). Animals were anesthetized with isoflurane and decapitated. The brain was excised and placed in a 4°C oxygenated (95% O_2/5% CO_2) slicing sucrose solution (in mM: 26 $NaHCO_3$, 23.4 sucrose, 10 $MgSO_4$, 0.11 glucose, 2.75 KCl, 1.75 Na H_2PO_4, 0.5 $CaCl_2$). Slices (300 μm) were cut in the coronal or parasagittal plane on a vibratome (Leica VT1000S), and placed for 1 hour in a 35°C oxygenated solution of artificial cerebral spinal fluid (ACSF) (in mM: 124 NaCl, 2.5 KCl, 1.25 NaH_2PO_4, 2.0 $MgSO_4$, 26 $NaHCO_3$, 10 glucose, 2 $CaCl_2$). Slices containing dLGN were selected for *in vitro* intracellular recording in the whole cell current clamp mode, and were perfused in an oxygenated solution of ACSF that was kept heated at 30°C. Cells were visualized with the aid of IR-DIC optics, and were patched with electrodes made of borosilicate glass filled with an internal solution (in mM: 140 K gluconate, 10 HEPES, 0.3 NaCl, 2 ATP-Mg, 0.1 GTP-Na; pH 7.25) containing 5% biocytin (Fig. 1). Patch electrodes were vertically pulled and had a final tip resistance of 3-7 MΩ. Electrodes were connected to an amplifier (Axoclamp 2B, Axon instruments). Different protocols of square wave current pulses (± 0.01 nA, 1000ms, 0.0025 nA increments) were applied and the resulting voltage responses were measured. Neuronal activity was digitized with an interface unit (National Instruments) and stored on a computer. Data acquisition and analysis was done using Strathclyde Electrophysology Software, Whole Cell Analysis Program V3.8.2.

To examine synaptic connectivity between cortex and dLGN relay cells, corticogeniculate axonal stimulation was done in a parasagittal thalamic slice (Turner and Salt, 1998; Krahe and Guido, 2011). Bipolar sharpened tungsten electrodes were placed at the internal capsule (Tocris Bioscience), and paired-pulse (PP) stimuli were delivered at different

interstimulus intervals (ISI, 100-1000 ms). Inhibitory activity was blocked with bath application of γ-aminobutyric acid (GABA) antagonists bicuculline (25 μM, Tocris 0131) and CGP (10 μM, Tocris 1248).

After recording, slices were fixed overnight with 4% paraformaldehyde (PFA) in 0.1M phosphate buffer solution (PBS; pH=7.2) and then incubated overnight in a 0.1% solution of Alexa Fluor 647 conjugated streptavidin (Invitrogen) dissolved in PBS with 0.1% Triton X-100. Slices were washed with PBS and then mounted with ProLong Gold with DAPI (Invitrogen), cured overnight at room temperature and stored in a freezer at -20°C. Labeled sections were initially visualized and photographed with an upright epi-fluorescence microscope (Nikon E600, Photometrics Cool snap camera) to select labeled cells that were suitable for 3-dimensional imaging by confocal laser scanning microscopy (Fig. 1).

Three-Dimensional Reconstruction

Three-dimensional reconstructions were done using a multi-photon/confocal laser scanning microscope (Zeiss LSM510 NLO Meta). Fluorescence from labeled dLGN neurons was excited using 633 nm HeNe laser and emission detected, using the Meta detector, over a range of 651 – 694 nm. Targeted neurons were imaged with either a Plan-Neofluar 40x (1.3 n.a) oil immersion objective lens or a C-Apochromat 40x (1.2 n.a) water immersion objective lens and a scan resolution of 2048 x 2048 pixels. 3-D datasets were compiled from a sequential series of optical slices with a step size through the z axis of 0.48 μm (40x/1.2 n.a. lens) or 0.5-0.58 μm (40x/ 1.3 n.a. lens). 3-D Z-stack datasets were rendered and analyzed offline using Volocity software (Improvision, version 4.3.2). For 15 neurons a zoom of 0.7-0.9 was utilized, because it was not possible to obtain the entire dendritic arbor in the field of view of the objective lens.

Image sequences were deconvolved using iterative restoration technique based upon a calculated theoretical point spread function to reduce signal noise generated from outside the focal plane of interest. Thresholding values were set according to signal intensity and background noise.

Cresyl violet nissl stain

Animals were anesthetized with isoflurane vapors, and transcardially perfused with PBS for 5 minutes, followed by 4% PFA (pH 7.2) in 0.1M PBS for 15-20 minutes. Brains were excised and fixed overnight with 4% PFA. Slices containing dLGN were cut on a coronal plane with a vibratome (70 µm), and left to dry overnight. Slices were washed for 3 minutes in 95% and 75 % ethanol solutions, respectively. Slices were washed in dH_2O for 1 minute, before immersing them in cresyl violet stain for 20-30 seconds, and then were rinsed briefly with dH_2O. Sections were dehydrated for 3 minutes in 70%, 95%, 95%, 100%, 100% ethanol solutions, respectively. Finally, slices were cleared in xylene twice for 5 minutes. Slides were mounted with Permount, and visualized by light microscopy (Olympus IX 71, Photometrics Cool snap camera), and pictures were taken with a 10x objective lens. Images were analyzed with Metamorph software. Area measurements and cell density counts were obtained from 2-4 consecutive sections through the middle of the dLGN. Cell density counts were calculated from a 100 µmx100 µm region of interest that was selected from the center of each representative dLGN section.

Immunohistochemistry

Slices containing dLGN were processed using antibody that stains for VGluT2, a vesicular glutamate transporter found in retinal terminals (Fujiyama et al., 2003). Slices

containing dLGN were cut on a coronal plane with a vibratome (40 μm). The following primary antibody was used: rabbit anti-VGluT2 (1:1000 dilution, Synaptic Systems, Cat# 135-403). Before incubation, sections were rinsed in PBS, and then treated for 1 hour with blocking solution (5% NGS, 2.5% BSA and 0.1% Triton X-100). Sections were incubated overnight with the primary antibody at 4˚C, rinsed with PBS, and were then incubated in the secondary antibody for 2 hours at room temperature (1:1000 dilution; Alexa 594 conjugated goat anti-rabbit IgG; Invitrogen, Cat# A11037). Sections were rinsed in PBS, mounted with Prolong Gold with DAPI (Invitrogen) and cured overnight at room temperature. Sections were photographed with an upright epi-fluorescence microscope (Nikon E600, Photometrics Cool snap camera).

RT-PCR

Retina and dLGN tissue were harvested from C57/Bl6 mice at different embryonic and postnatal ages using methods described elsewhere (Su et al., 2011). RNA was isolated using the Bio-Rad Total RNA Extraction from Fibrous and Fatty Tissue kit (Bio-Rad). Reverse transcription and cDNA generation were made using Superscript II Reverse Transcriptase First-Strand cDNA Synthesis kit (Invitrogen). The following *math5* primer pairs were used: 5'-ATGGCGCTCAGCTACATCAT- 3' and 5'-GGGTCTACCTGGAGCCTAGC- 3'. The annealing temperature utilized was 56 ˚C.

Electron Microscopy

Analysis of dLGN ultrastructure was carried out as previously reported (Bickford el al., 2010). Mice (P21, 22) were deeply anesthetized with isoflurane vapors and perfused transcardially with 2% PFA/2% glutaraldehyde in 0.1M phosphate buffer solution for 15-20

minutes. Brains were excised and cut on a coronal plane (50–100 μm thick) using a vibratome (Leica VT100E). Sections were postfixed in 2% osmium tetroxide, dehydrated in a graded series of ethyl alcohol and then embedded in Durcupan resin. 70 nm ultrathin sections were cut, collected on Formvar-coated nickel slot grids and then were stained with uranyl acetate. Sections were examined with a Philips CM10 electron microscope, and images were collected with a digitizing camera (SIA-7C; SIA, Duluth, GA).

Thresholding analysis

Mice ranging between P2-21 were deeply anesthetized with isoflurane and transcardially perfused with PBS followed by 4% PFA in 0.1 M phosphate buffer for 15-20 minutes. The brains were postfixed in 4% PFA overnight and sectioned at 70 μm in the coronal plane using a vibratome (Leica, VT100S), and were mounted in ProLong Gold antifade reagent with DAPI (Invitrogen). Images of dLGN were acquired with a Photometrix Coolsnap camera attached to a Nikon Eclipse fluorescence microscope using a 10x objective lens. Fluorescent images of labeled sections were acquired and digitized separately (1300 × 1030 pixels/frame) using the following filter settings: Alexa 488: Exciter 465–495, DM 505, BA 515–555. To determine the spatial extent of corticogeniculate projections in the dLGN, threshold imaging protocols were used (Jaubert-Miazza et al., 2005). The boundaries of dLGN were delineated, and the spatial extent of corticogeniculate projections was determined by summing the area across 2-4 successive sections through the middle of dLGN and then expressing the labeled regions as a percentage of the total area of dLGN.

Results

Math5-null model

Math5 expression in dLGN

Math5 encodes a helix-loop helix transcription factor that specifies RGC fate (Brown et al., 1998; Brown et al., 2001; Wang et al., 2001). Embryonically, *math5* is expressed in the retina as well as the tenth cranial ganglion (Brown et al, 1998). In the retina, *math5* is developmentally regulated, first appearing at E11, continuing through birth, but is absent in the adult (Brown et al., 1998; Brown et al., 2001; Wang et al., 2001). It is also expressed in the adult tissue such as hindbrain and in a subset of neurons in the ventral cochlear nucleus (VCN; Saul et al, 2008). A closer examination of *math5* expression in central visual targets such as dLGN has been lacking. Here, we examined *math5* expression in the developing retina and dLGN using RT-PCR (Fig. 2). As expected, *math5* is expressed in the retina between E13-P3, but is absent at P13 and in the adult. Moreover, we found no evidence of *math5* expression at P2, 3, 14 and adult dLGN. Thus any reported changes observed in developing relay cells cannot be attributed to the lack of *math5* in the brain, but rather is a direct consequence of the absence of RGCs.

dLGN is devoid of retinal axons

Most studies on *math5*-nulls have been restricted to the retina. While some have noted that the optic nerve fails to form in these mutants, few studies have examined on a cellular level whether the remaining 5% of RGCs grow axons that enter the brain (Brown et al., 2001; Wang et

al., 2001; Wee et al., 2002; Brzezinski et al., 2005). In order to confirm that the dLGN does not receive any retinal inputs from these few remaining RGCs, injections of the anterograde tracer CTB conjugated to different fluorescent dyes were made (Fig. 3; Alexa fluor 488: left eye; 594: right eye). This technique allows for the visualization of retinal terminal fields in central visual structures (Jaubert-Miazza et al., 2005). By injecting different fluorescent dyes in each eye, the eye-specific patterning is revealed. For example, retinal projections arising from the contralateral eye occupy as much as 85-90% of the territory in dLGN. Whereas ipsilateral retinal axons terminate in the anterior medial sector of dLGN forming a small non-overlapping patch that occupies only 10-15% of the area of the nucleus (Jaubert-Miazza et al., 2005). In contrast, in the suprachiasmatic nucleus (SCN) projections from both eyes are intermingled. This is illustrated for WT SCN and dLGN in figures 3B and 3C, respectively. CTB injections were made in *math5*-nulls between P2-P48, and indeed there was no evidence of CTB labeling in dLGN (Fig. 3C). Moreover, we failed to detect any labeled elements in regions that correspond to optic nerve, optic tract or other retino-recipient targets such as SCN (Fig. 3A, 3B; see also Wee et al., 2002; Brzezinski et al, 2005).

To further confirm the absence of retinal innervation in the dLGN, the expression of vesicular glutamate transporter2 (VGluT2) was examined using immunohistochemistry. VGluT2 is found exclusively in retinal terminals, as well as in thalamocortical axons collaterals within dLGN (Fig.4, Fujiyama et al., 2003; Land et al., 2004; Bickford et al., 2008). At P14, there was almost a complete absence of VGluT2 in *math5*-nulls. The residual weak staining that we observed was similar to the labeling pattern seen after a 7-day binocular enucleation, and perhaps reflected terminals originating from thalamocortical axon collaterals (Fig. 4, see also Fujiyama et al., 2003; Bickford et al., 2008).

Finally, we examined the ultrastructure of dLGN in *math5*-nulls (Fig. 5). In WT, retinogeniculate terminals are characterized as having round vesicles, large profiles and pale mitochondria (RLP), whereas, corticogeniculate and brainstem terminals have round vesicles, small profiles and dark mitochondria (RSD) (Rafols and Valverde, 1973; Bickford et al., 2010). In *math5*-nulls, we examined 14 sections in dLGN. RSD profiles could be readily detected. However, we failed to detect any RLP profiles. Typically, RLP profiles constitute around 12% of the total synaptic terminals in WT (Bickford et al., 2010). Instead, we noted the presence of terminals characterized by having round vesicles, large profiles and dark mitochondria termed RLD (Fig. 5). RLD profiles have been observed in enucleated, anophthalmic and microphthamic strains of mice, but their origin is yet to be determined (Cullen and Kaiserman-Abramof, 1976; Kaiserman-Abramof, 1983; Winkelmann et al., 1985).

Taken together, these results indicate that retino-recipient targets such as dLGN are devoid of retinal innervation in *math5*-nulls. Thus, these mutants serve as a suitable model for studying the development of relay cells in the absence of retinal innervation and signaling.

Morphological characteristics of relay cells

Representative examples of biocytin filled relay cells at different postnatal ages in *math5*-*n*ulls are shown in figure 6. Several morphological features were studied including: total, somatic and dendritic surface area, dendritic field, complexity and branching patterns. In addition, cell class specification and location within dLGN were examined. A total of 58 relay cells were studied in *math5*-nulls ranging between P4-35, and their morphology was compared to WT age-matched counterparts (*n*=82). In general, *math5*-null relay cells had large somata, multipolar dendrites, and long axons that left the nucleus. At first glance, these cells appeared

similar to their WT counterparts. However, a quantitative analysis revealed differences in their growth patterns and dendritic architecture.

Surface area of relay cells

Total surface area measurement for individual dLGN relay cells were obtained on a 3-dimensional scale by selecting an area of interest that highlights the neuron and its processes in all the captured Z-stacks. Soma surface area was obtained by outlining the cell body in the X, Y and Z planes, and dendritic surface area was calculated as the difference between total and somatic surface area for each neuron. Surface area measurements were made for a total of 69 relay cells in WT (P2-35) and 55 relay cells in *math5*-nulls (P4-35).

In WT, there was a significant increase in dendritic surface area with age (Fig. 7A; one-way ANOVA, F=9.103, p<0.0001). This was manifested by roughly a 3-fold increase in dendritic surface area between the first and third postnatal weeks (n=8 week 1, $1.47x10^4 \pm 6.58x10^3$ µm^2 *vs.* n=19 week3, $5.02x10^4 \pm 6.21x10^3$ µm^2; Bonferroni *post hoc* test, p<0.0001). After this time, dendritic surface area showed no significant changes through the fifth postnatal week (n=8, $5.05x10^4 \pm 6.58x10^3$ µm^2; Bonferroni *post hoc* test, p=1). By contrast, soma surface area remained relatively constant throughout postnatal weeks 1-5 (Fig. 7B; one-way ANOVA, F=0 .444, p=0.777).

Relay cells in *math5*-nulls showed significant changes in dendritic surface area with age (Fig. 7B; one-way ANOVA, F=4.268, p<0.01). There was a steady increase in dendritic surface area that peaked by the third postnatal week and represented roughly a 4-fold increase compared to postnatal week 1 (n=7 week1, $1.35x10^4 \pm 1.08x10^4$ µm^2 *vs.* n=17 week3, $6.22x10^4 \pm 6.93x10^3$ µm^2; Bonferroni *post hoc* test, p<0.01). However, dendritic surface area declined, so that by the fifth postnatal week values were comparable to those seen at week 1 (n=8, $2.61x10^4 \pm 1.28x10^4$

μm^2; Bonferroni *post hoc* test, p=1). Soma surface area showed a similar growth pattern. The third postnatal week marked a peak in the growth of neuronal cell bodies. Whereas a significant reduction was observed during the fifth week (Fig. 7B; n=17 week3, $1.26x10^3 \pm 1.49x10^2$ μm^2 *vs.* n=5 week5, $7.31x10^2 \pm 2.76x10^2$ μm^2; Temhane *post hoc* test, $p<0.01$).

Dendritic surface area in *math5*-nulls were comparable to WT during the first, third and fourth postnatal weeks. However, *math5*-nulls showed a significant increase in dendritic surface area during the second postnatal week (Fig 7A, 7B; n=25 WT, $2.41x10^4 \pm 3.73x10^3$ μm^2 vs. n=17 *math5*-null, $4.83x10^4 \pm 6.93x10^3$ μm^2; Student's *t*-test, $p<0.01$). Such growth was not sustained and by the fifth postnatal week, relay cells in *math5*-nulls were significantly smaller than those in WT (Fig. 7A, 7B; n=8 WT, $5.04x10^4 \pm 6.58x10^3$ μm^2 vs. n=5 *math5*-null, $2.61x10^4 \pm 1.28x10^4$ μm^2; Student's *t*-test, $p<0.05$). Overall, soma surface area in *math5*-nulls was significantly smaller than WT, with the exception of week 4 (Fig. 7C; n=9 WT, $1.39x10^3 \pm 3.87x10^2$ μm^2 vs. n=8 *math5*-null, $1.37x10^3 \pm 2.18x10^2$ μm^2; Student's *t*-test, p=0.9).

Dendritic field

Different aspects of dendritic complexity were examined including dendritic field, number of branches, as well as branching patterns. First, the 3-dimensional space occupied by relay cells' dendrites was measured to obtain an assessment of their dendritic fields. This was calculated as the product of the lengths of dendritic field extent in the X, Y and Z axes. For each relay cell, Z axis was identified as the depth of the stacked image, and X and Y axes were assigned from the projection image, and they were two perpendicular lines crossing at the soma. A total of 82 relay cells were examined in WT (P1-40) and 58 relay cells in *math5*-nulls (P4-35).

In WT, relay cells underwent a progressive increase in dendritic field size until the third postnatal week (Fig. 8A; one-way ANOVA, F=16.97, p<0.0001). By the fifth postnatal week, cells exhibited about a 5-fold increase in dendritic field compared to the first week (Fig. 8A; n=10 week 1, $6.35x10^5 \pm 2.93x10^5$ µm^3 *vs.* n=10 week 5, $3.19x10^6 \pm 2.93x10^5$ µm^3; Bonferroni *post hoc* test, p<0.0001).

Relay cells showed changes in dendritic field with age in *math5*-nulls (Fig. 8A; one-way ANOVA, F=3.601, p=0.012). Dendritic field peaked by the fourth postnatal week, where there was a 3-fold increase compared to week 1 (n=8 postnatal week 1, $7.20x10^5 \pm 4.18x10^5$ µm^3 vs. n=10 postnatal week 4, $2.52x10^6 \pm 3.74x10^5$ µm^3; Temhane *post hoc* test. p<0.01). In contrast, values were not significantly different between the first and fifth weeks (n=5 postnatal week 5, $1.77x10^6 \pm 5.29x10^5$ µm^3; Temhane *post hoc* test, p=0.051).

Compared to WT, *math5*-nulls showed comparable dendritic field size throughout the first 4 weeks. However, *math5*-nulls were significantly smaller than WT at the fifth postnatal week (Student's *t*-test, p<0.01), indicating that growth stopped in *math5*-nulls while it continued in WT.

Dendritic complexity and branching pattern

Dendritic branching patterns were assessed using the centrifugal method (Fig. 9A; Fiala et al., 2008). Primary dendrites are those that stem from the cell body of the neuron. The degree of branching reflects their complexity and can be measured simply by counting the number of successive branch points on each of their identified primary dendrites (Fig. 9A). On a 3-D scale, this was done by toggling up and down through the entire 3-D rendered stack in the z-plane, identifying primary order dendrites, and counting the order as well as the number of each of their

consecutive daughter branches. The branching patterns were studied for 40 relay cells in WT (P1-P40) and 51 relay cells in *math5*-nulls (P4-35).

In WT, branching showed significant increase with age (Fig. 9B; one-way ANOVA, F=9.67, p<0.0001). Between weeks 1 and 2, relay cells displayed a 2-fold increase in the total number of dendritic branches. However, between weeks 2-5 branch numbers remained relatively stable. On average, WT cells had roughly 49.4±7.3 total branches during the first week and 98.2±3.8 thereafter. In *math5*-nulls, branching also showed significant changes with age (Fig. 9B; one-way ANOVA, F=13.557, p<0.0001). Between weeks 1-2, branch numbers increased significantly from 58.1±7.7 (n=8) to 126.5±5.6 (n=15; Bonferroni *post hoc* test, p<0.0001). However, *math5*-nulls failed to maintain these numbers between weeks 3-5, so that by the fifth week the number of dendritic branches was reduced to 82.0±10.9 (n=4; Bonferroni *post hoc* test, p<0.01).

Finally, branching patterns were assessed as a means to further characterize complexity. The number of branch points for each branch order was calculated (Fig. 9C). In *math5*-nulls and WT, most cells regardless of age had 6-7 primary dendrites and the bulk of branching occurred between the 3rd-5th orders. In WT, branching patterns were similar between weeks 2-5, with some cells branching up to the 9th order. In contrast, *math5*-nulls branched up to the 13th order and the branching pattern between different age groups was not conserved.

Compared to WT, there was no significant difference in the total number of branches during the first week in *math5*-nulls (Fig. 9B). However, a close examination of their branching patterns revealed that *math5*-nulls had increased numbers of 6th order branches (Fig. 10; n=8 WT, 1.0±0.4 vs. n=8 *math5* null, 4.0±0.9; Student's t-test, p<0.01). Moreover, *math5*-nulls showed significantly higher numbers of branches during the second postnatal week (Fig. 9B; n=

9 WT, 99.7±6.9 vs. *n*=15 *math5*-null, 126.5±5.6; Student's *t*-test, $p<0.01$). These differences were mainly due to sprouting of higher order dendrites, where *math5*-nulls had significantly more 6^{th} -10^{th} order dendritic segments (Fig.10; Student's *t*-test, branch orders 6-8 $p<0.0001$, branch orders 9-10 $p<0.01$). *Math5*-nulls underwent a loss of higher order dendrites, so that by the third and fourth postnatal weeks there were no differences in the total numbers as well as branching patterns compared to WT (Fig. 8B, 9). However, by the fifth postnatal week, relay cells had significantly fewer 2-4 order dendritic segments (Fig. 10; *n*= 5 WT vs. *n*=4 *math5*-null; Student's *t*-test, branch orders 2-4 $p<0.05$).

Taken together, these analyses showed that the increased dendritic surface area seen in *math5*-nulls during the second postnatal week can be explained by exuberance in dendritic branching, especially among higher order segments. Furthermore, the reduction in dendritic surface area seen during the fifth postnatal week is due to a reduction in dendritic field as well as a continued loss of dendritic branches.

Relay cell class specificity and location

Recently we showed that relay cells can be divided into three classes that have distinct dendritic architecture and strong regional preferences in dLGN (see Appendix I- Krahe and El-Danaf et al., 2011, submitted; El-Danaf and Krahe et al., 2009). Y-cells were found to have radially oriented dendritic trees and resided in a central band parallel to the optic tract. W-cells had a hemispherical morphology and were located along the dorso-ventral borders of the nucleus. Finally, X-cells had a bi-conical morphology and were preferentially situated in the monocular segment of the dLGN. This was done using a Sholl ring analysis where the dendritic field of every neuron was divided into equidistant regions through five concentric rings centered

on the soma, and where the fifth circle would comprise all but the tips of the most distal dendrites. Two perpendicular lines passing through the soma divide these rings into two planes. The total number of dendritic processes intersecting each ring was counted for each one of these planes. For every cell, a dendritic orientation index (DO*i*) was calculated by dividing the maximum number of intersections in one axial plane versus the other. DO*i* was then used to perform a k-clustering analysis. Distributions of DO*i* formed three distinct clusters. Cells with DO*i* between 0-0.49 had a bi-conical morphology (X-like); those with values between 0.50-0.79 had hemispheric profile, while those between 0.80-1.0 were radially symmetric. For each one of these clusters, the relative location of all the cells within the dLGN was determined. For further details see Appendix I-Krahe and El-Danaf et al., 2011, submitted (El-Danaf and Krahe et al., 2009).

Using the same approach, the dendritic architecture of 42 relay cells in *math5*-nulls was analyzed. Similar to WT, DO*i* revealed that relay cells in *math5*-nulls clustered into three groups that had dendritic architecture similar to X-, Y- and W-cell classes in WT. A total of 13 cells were classified as Y- cells, 13 as X- cells and 16 as W- cells. Figure 11A depicts representative examples of the three morphological groups, and show that in the absence of retinal innervation relay cells seem to maintain their morphological identity. As shown in figure 11B, an examination of the location of these cells within the dLGN revealed that Y- and W-cells seemed to retain their regional preference with Y-cells residing in a central band throughout the nucleus, and W-cells along the dorso-ventral borders of the dLGN. In contrast to WT, X- cells were found in a dorso-medial region of the dLGN that extended well beyond the monocular segment.

Structural organization of the dLGN

So far, the focus has been directed on cellular morphology. However, there is evidence of potential trophic support provided by retinal axons, which can have a more global effect in dLGN development including cytoarchitecture, size and cell density (Heumann and Rabinowicz, 1980; Williams et al., 2002). For this, we used nissl stain to delineate the boundaries of dLGN and surrounding nuclei, as well as to get estimates of cell numbers. Area measurements were obtained by identifying the border of dLGN in 2-4 consecutive 70 µm thick sections through the middle of the nucleus. A total of 51 sections of dLGN in WT and 79 sections in *math5*-nulls ranging between P2-35 were analyzed.

In WT, there was a 3-fold increase in dLGN area between postnatal weeks 1-3 (Fig.12; n=33 week1, $10.8x10^4$ µm^2 vs. n=7 week3, $31.2x10^4$ µm^2; Temhane *post hoc* test, $p<0.0001$), but then remained the same through the fifth week (n=4, $31.1x10^4$ µm^2). In *math5*-nulls, the dLGN and surrounding nuclei were readily apparent. The dLGN area peaked by the third postnatal week (n=35 week1, $8.9x10^4$ µm^2 vs. n=8 week3, $15.2x10^4$ µm^2; Bonferroni *post hoc* test, $p<0.0001$). Between weeks 3-5 dLGN area decreased, so that by the fifth week it measured $11.8x10^4$ µm^2 (n=7, Bonferroni *post hoc* test, $p<0.01$). Compared to WT, *math5*-nulls showed roughly a 50% reduction in overall size, and dLGN was significantly smaller in area throughout all studied age groups (Student's *t*-test; weeks1, 3-5 $p<0.0001$; week2 $p<0.01$).

Cell density counts were calculated from a 100 µmx100 µm region of interest that was selected from the center of each representative dLGN section (Fig. 12A, 13A). Measurements were restricted to neurons in which the soma and nucleus were clearly delineated. A total of 19 dLGN sections were examined in WT (P7-P35) and 38 sections in *math5*-nulls (P5-35). In WT, cell density remained stable with no significant changes occurring throughout the studied period

(Fig.13; 25-32 cells/10^4 µm^2; one-way ANOVA, F=2.723, p=0.072). In *math5*-nulls, there was roughly a 37% reduction in cell density between weeks 1-3 (n=4 week1, 58.0±1.9 cells/10^4 µm^2 vs. n=7 week3, 36.1±1.4 cells/10^4 µm^2; Bonferroni *post hoc* test, p<0.0001). Between weeks 3-5, cell density exhibited no significant change (n=9 week5, 33.4±1.2cells/10^4 µm^2; Bonferroni *post hoc* test, p=1). Since dLGN area was similar between weeks 1 and 5 in *math5*-nulls, the reduced cell density might reveal a cell loss, whether this is due to lack of retinal innervation or perhaps some delay in programmed cell death remains to be answered. Compared to WT, cell density was significantly higher in *math5*-nulls in all age groups, except at week 4 (n=4 WT, 30.62±1.5 cells/10^4 µm^2 vs. n=6 *math5*-null, 32.8±1.5 cells/10^4 µm^2; Student's t-test, p=0.43). Such increase may simply reflect the overall smaller dLGN size in *math5*-nulls which would perhaps indicate an overcrowding of dLGN cells.

Functional characteristics of relay cells of dLGN in math5 null

The intrinsic membrane properties of relay cells in *math5*-nulls were also examined by conducting *in vitro* whole cell recordings prior to filling them with biocytin (Fig. 1). Square wave current pulses of varying duration and intensity were delivered through the recording pipette (e.g. ± 0.01 nA, 1000 ms, 0.0025 nA increments), and the resulting voltage responses were obtained. These current step protocols were used to examine both passive and active membrane properties for a total of 135 relay cells ranging between P4-41 in *math5*-nulls, and were compared to previous recordings done in our lab (Dilger et al., 2011) and by others (Macleod et al., 1997). Examples of voltage responses to current steps and I-V relations are shown in figure 14 (WT) and figure 15 (*math5*-nulls). The intrinsic membrane properties of WT and *math5*-nulls are summarized in table 1.

The passive membrane properties that we examined included: resting membrane potential, input resistance and tau (τ). The resting membrane potential in *math5*-nulls was similar to WT (Table.1; <P14: *n*=54 WT, -52.2± 1.5 mV vs. *n*=73 *math5*-null, -61.4± 0.8 mV) and (≥P14: *n*=62 WT, -61.4±2.4 mV vs. *n*=62 *math5*-null, -59.7± 2.2 mV). As in WT, *math5*-nulls showed a similar decrease in input resistance with age. In both cases, data can be fit to a single exponential curve (Fig. 16A; r=0.67 WT; r=0.74 *math5*-null). However, input resistance was significantly higher in *math5*-nulls (Fig 16A; <P14: *n*=28 WT, 653.6 ± 66.2 MΩ vs. *n*=68 *math5*-null, 1254.4 ± 51.0 MΩ; Student's *t*-test $p<0.0001$) and (≥P14: *n*=34 WT, 365.4 ± 35.3 MΩ vs. *n*=63 *math5*-null, 539.5 ± 24.2 MΩ; Student's *t*-test $p<0.0001$). These differences can be in part explained by the reduced soma area seen in *math5*-nulls (Fig. 7B).

In WT, τ remained relatively stable with age (Fig. 16B; linear regression, *n*=51, r=0.26), but showed a significant reduction in *math5*-nulls. The data can be fit to a single exponential curve (*n*=61, r= 0.75). In both age groups, *math5*-nulls had a significantly shorter τ compared to WT (Table.1; Fig. 16B; <P14: *n*=23 WT, 44.0 ± 2.9 ms vs. *n*=20 *math5*-null, 35.9 ± 2.4 ms; Student's *t*-test, $p<0.05$) and (≥P14: *n*=28 WT, 38.2 ± 2.6 ms vs. *n*=41 *math5*-null, 21.3 ± 1.2 ms, Student's *t*-test, $p<0.0001$). These results might reflect smaller dendritic arbors that we observed in *math5* nulls (Fig.7A, 8).

We also examined the active membrane properties of relay cells and these included: LTS, I_h, I_A, and Na^+ spikes (Figs. 14, 15). Indeed many of the voltage-gated conductances noted in WT were also present in *math5*-nulls and their incidence prior to and after P14 is reported in table1. Activation of these membrane properties is apparent in their I-V plots (Fig. 15). Note the non-linearity in their I-V relations. For example, at hyperpolarized membrane potential, there is an inward rectification due to a large depolarizing sag in the voltage response, which is mediated

by the activation of the mixed cation conductance (I_h). At more depolarized levels, we noted an outward form of rectification which is likely due to the activation of I_A, which is mediated by a K^+ current and causes a delay in the firing of action potential. In addition, the termination of membrane hyperpolarization caused a rebound low-threshold calcium spike (LTS), which was found in nearly all the cells and is noted by a large triangular depolarization. With age, LTS is capable of stimulating a burst of action potentials that ride on top of this triangular depolarization. We also examined the firing properties of relay cells. Increasing levels of membrane depolarization lead to a train of Na^+ spikes. These spikes are relatively immature early on, but their duration at half-height is reduced with age (Table.1; <P14: *n*=57 WT, 1.6±0.2 ms vs. *n*=49 *math5*-null, 2.7±0.1 ms) and (≥P14: *n*=62 WT, 0.9±0.2 ms vs. *n*=41 *math5*-null, 1.5±0.1 ms). The change in spike duration can be fit to a single exponential curve (Table1; Fig.17; *n*=92, r=0.76). The amplitude of Na^+ spikes is established early and remained unchanged with age

Repetitive firing characteristics of relay cells in the *math5*-nulls were also investigated. This was done by injecting depolarizing current pulses with varying intensities. Representative examples from the responses of 2 relay cells at P10 and P27 are depicted in figure 18. Firing frequency increased with membrane depolarization. For every relay cell, the slope of firing frequency relative to current intensity was measured and showed that these are established early and are sustained with age (Fig. 17C; *n*=78, r=0.22). As previously indicated, relay cells show a delay in firing of action potential in response to a depolarizing current. This latency to spike firing is also established at early ages and remained constant with age (Fig. 17C; *n*=78, r=0.03), and it decreased with increasing current intensity. Finally, relay cells exhibited frequency

adaptation to spike firing indicated by an increase in the interspike interval, which is mediated by various K^+ currents (Fig. 17AB, far right panels).

Overall, these observations indicate that the development of the intrinsic membrane properties of relay cells is largely unaffected by the absence of retinal innervation. This could suggest that the expression and perhaps the maturation of these conductances occur independent of retinal input.

Corticogeniculate innervation in Math5-null

Timing and pattern of innervation

Whether the lack of retinal innervation affects the development of other circuits in the dLGN remains unanswered. One of the largest projections to dLGN arises from layer VI of visual cortex (Bickford et al., 2010). Here, we examined the corticogeniculate pattern of projection in the dLGN of *math5*-nulls by crossing them with the *golli-τ*-GFP transgenic mouse (Jacobs et al., 2007). In the latter, corticofugal projections arising from layer VI are labeled with GFP, whose expression is under the control of the *golli* promoter element of the myelin basic protein gene. Mice heterozygous for the *math5*-null allele ($math5^{-/+}$) exhibit no retinal defects (Wang et al., 2001). Therefore, littermate pups that were heterozygous for the *math5*-null gene ($math5^{-/+}$/ *golli-τ*-GFP) served as controls. Eye injections of CTB were also made to confirm that *math5*-nulls lacked retinogeniculate projections but they were maintained in controls (Fig. 19). At P14 and P21 both *math5*-null crosses and littermate controls showed a dense plexus of corticogeniculate terminals throughout the entire dLGN. Similar to *golli-τ*-GFP transgenics, the ventral lateral geniculate nucleus (vLGN) failed to receive input from layer VI of cortex (Fig.

19). Taken together, these results suggest that target selection occurs independently of retinal innervation.

The development of these inputs was further analyzed by outlining the dLGN and measuring the spatial extent of corticogeniculate projections at different postnatal ages. The progression of innervation in littermate controls was similar to that observed in *golli-τ*-GFP transgenics (Seabrook et al., 2010). Therefore, the values reported in figure 19 here have been merged. In these controls, cortical axons arrived at the ventromedial border of the dLGN at P2, entered at P4 and innervated the dLGN over the course of the next two weeks. For example, at P10 about 84.8 ± 0.75% (*n*=7) of dLGN was innervated by corticogeniculate projections. By P14 the dLGN was fully innervated (*n*=11, 92.2±0.52%). In *math5*-nulls, cortical axons arrive at the border of dLGN around the same time (P2) as in controls. However, the rate at which these axons innervate the dLGN was greatly accelerated. At P3, there was roughly a 4-fold increase in the percent area occupied by cortical axons (*n*=9, 26.04 ± 2.91%) compared to controls (*n*=8, 5.92%±0.72). At P7, 75.47±3.68% (*n*=4) of the area of the nucleus was occupied by cortical axons and reflected about a 1.5-fold difference compared to controls (*n*=7, 49.54 ± 6.40%). The spatial extent at P7 cannot be attributed to a smaller size of dLGN, since at this age the area of dLGN was similar between *math5*-nulls (0.115 ± 0.003 mm^2) and controls (0.123 ± 0.004 mm^2). By P8-9 innervation was complete roughly a week earlier than controls. Patterns of innervation for both controls and *math5*-nulls could be fit to a sigmoidal curve (controls: *n*=142, r=0.99, *math5*-nulls: *n*= 44, r=0.99). However, the slopes were significantly different (m=4.98 WT; m=3.23 *math5*-nulls). These results suggest that the accelerated rate of corticogeniculate innervation is controlled by signals derived from the retina.

Function of corticogeniculate axons

Finally, we tested whether the structural innervation is accompanied by functional patterns of connectivity between relay cells and corticogeniculate axons. For this we made use of a parasagittal slice in which corticogeniculate connections to dLGN were preserved (Turner, and Salt, 1998; Seabrook et al., 2010; Krahe and Guido, 2011). Corticogeniculate fibers were electrically stimulated by placing a bipolar stimulating electrode on the internal capsule, and evoked synaptic responses were recorded from individual dLGN relay cells in the whole cell patch clamp mode. We also assessed whether synaptic responses showed the characteristic facilitation by using different paired-pulse (PP) protocols in which the interstimulus intervals were systematically varied (ISI; 100-1000 ms). Paired-pulse ratios (PPR) were calculated by dividing the amplitude of the second evoked excitatory post synaptic potential (EPSP) by the first one.

Electrical stimulation of corticogeniculate axons evoked robust EPSPs in dLGN neurons (Fig. 20, left panel). Moreover, paired-pulse facilitation was observed at both P8 and P14, which was similar in magnitude to values reported in *golli-τ*-GFP transgenics (Fig. 20, right panel). We were able to vary ISI at P14, and found that the greatest degree of facilitation was noted at 100 ms with a PPR of 2.15±0.45, as in *golli-τ*-GFP transgenics (PPR= 2.45±0.18; Fig. 20; Seabrook et al., 2010). After 300 ISI, facilitation was barely detectable with PPR values ranging between 0.98-1.3. These results confirm the electron microscopy analysis suggesting that the RSD profiles that we observed are likely of cortical origin (Fig. 5). Taken together, these results show that the loss of retinal innervation does not affect synapse formation between cortical axons and relay cells.

Figure 1

3-D reconstruction of biocytin filled relay cells recorded in an acute thalamic slice preparation.

A. DIC image of a thalamic slice preparation containing dLGN. Shown is a patch electrode filled with biocytin. **B.** High power DIC image of the same slice showing somas of relay cells with patch pipette in whole cell patch mode. Current injection protocols were used to fill cells and examine their intrinsic membrane properties. **C.** Slices were fixed overnight, and then were washed with 0.1% solution of Alexa Fluor 647 conjugated streptavidin. Labeled sections were initially visualized with an upright epi-fluorescence microscope to select cells that were suitable for 3-D confocal imaging. Fluorescent image of the P6 biocytin labeled relay cell shown in (**B**). **D.** Sequential series of optical slices taken by confocal microscopy of a P15 dLGN neuron. Step size through the Z-axis is 0.48 µm. **E.** Maximum intensity projection image of the 3-D rendered neuron. Scale bar = 50 µm

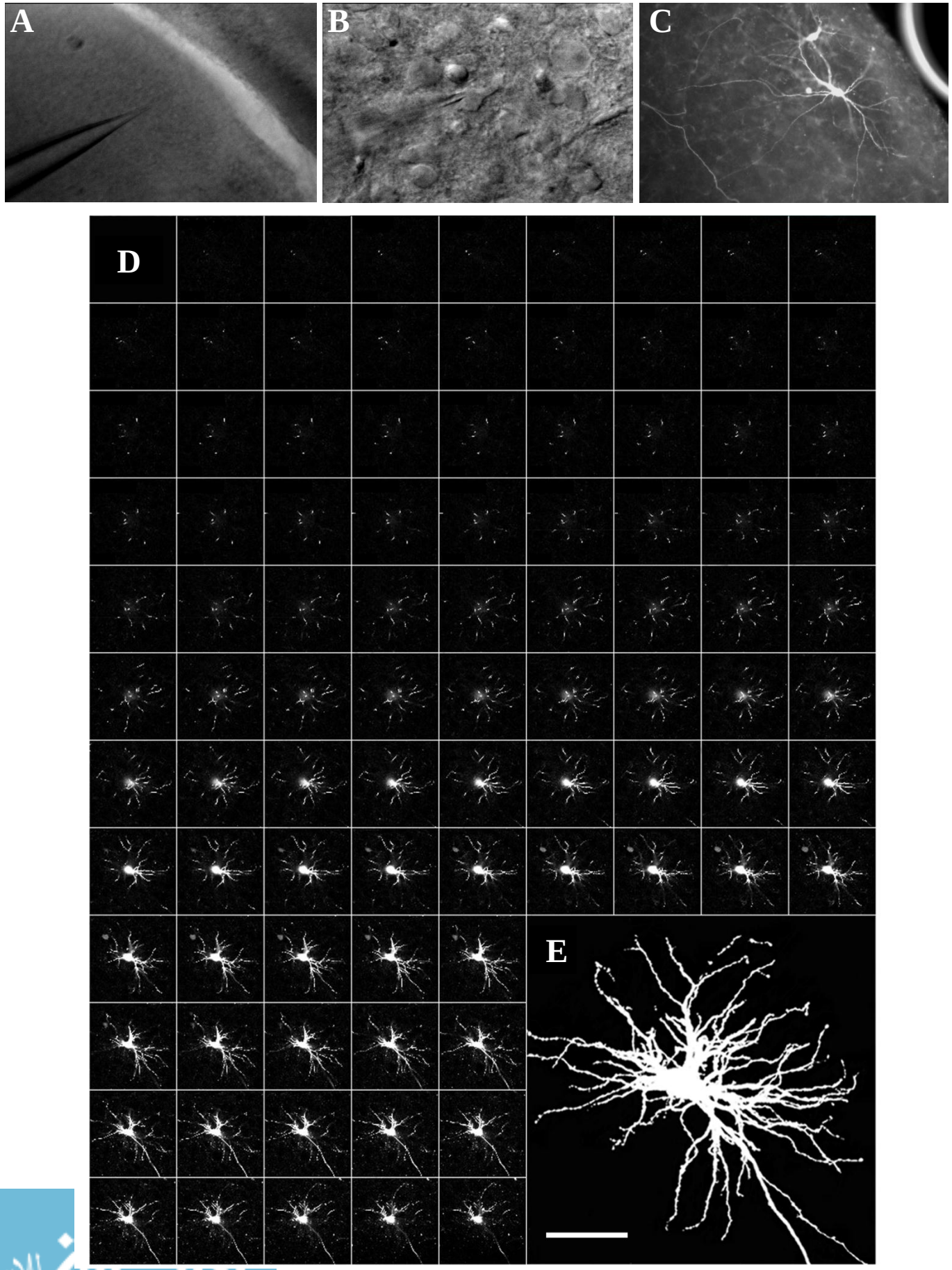

Figure 2

***Math5* expression in retina and dLGN of WT mouse.**

RT-PCR showing the expression of *math5* in WT retina and dLGN at different embryonic (E) and postnatal (P) ages. *Math5* expression is developmentally regulated in the retina appearing embryonically, continuing through birth, but is absent in the adult. Note the absence of *math5* expression in the dLGN at all studied ages.

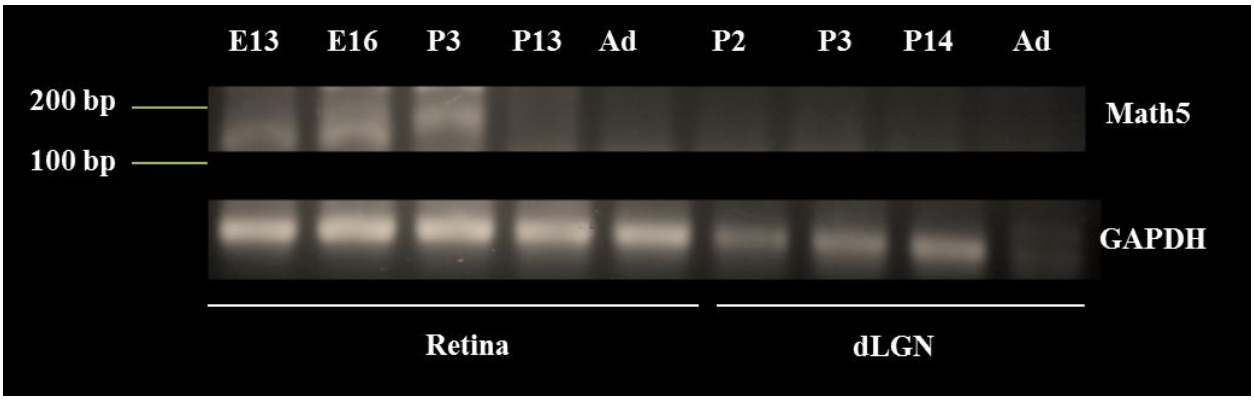

Figure 3

Anterograde labeling of retinal ganglion cells in the retina and central visual targets.

The anterograde tracer CTB conjugated to different Alexa fluor dyes was injected in the eyes of a P48 *math5*-null and several retino-recipient structures were examined (488: green, left eye; 594: red, right eye). **A.** Cryostat section through the retina of *math5*-nulls showing the different cellular layers with DAPI staining (left panel; ONL: outer nuclear layer; INL: inner nuclear layer; GCL: ganglion cell layer) and CTB labeling (green, middle panel). Far right: merged image (DAPI: blue; CTB: green). Note the faint GCL, as well as the absence of CTB labeled retinal axons. **B-C.** Coronal sections of the suprachiasmatic nucleus (SCN: top row) and dLGN (bottom row) from WT (far left panel) and *math5*-nulls (right panel). In WT, projections from both eyes are intermingled in SCN. While in dLGN, ipsilateral projections (red) terminate in the anterior medial sector of the nucleus occupying 10-15% of the area of the nucleus, whereas contralateral projections (green) occupy 85-90% of the territory in dLGN. Note the absence of CTB labeling in *math5*-nulls. High power images also failed to reveal any CTB labeling (data not shown). Dashed lines delineate the borders of dLGN and SCN. Scale bar= 200 μm.

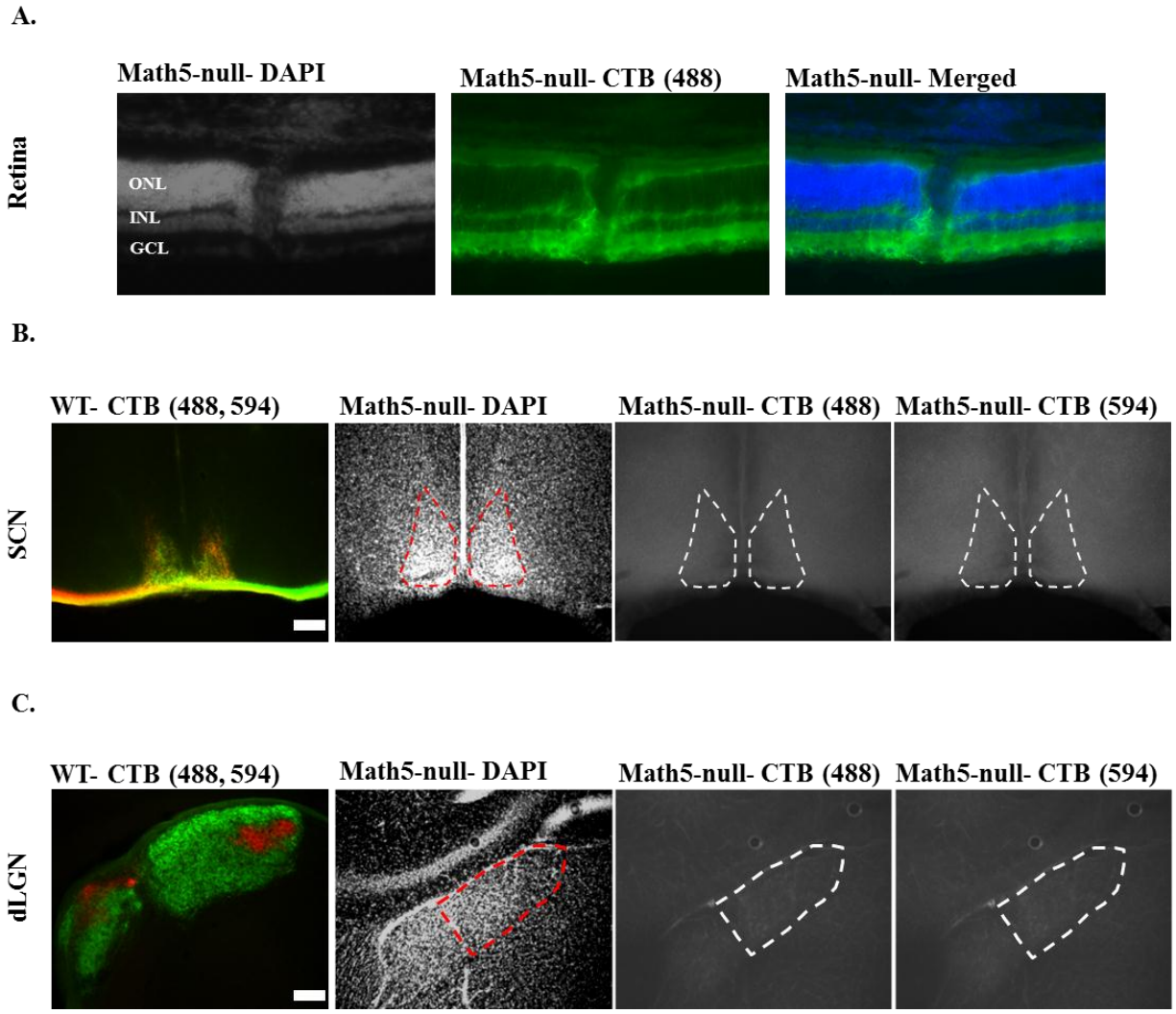

Figure 4

VGluT2 immunoreactivity in the dLGN of WT and *math5*-nulls.

Coronal sections of dLGN showing the staining pattern of the retinal terminal marker vesicular glutamate transporter 2 (VGluT2). Images were photographed with an upright fluorescent microscope. Note that there was almost a complete absence of VGluT2 immunoreactivity in P14 *math5*-null (middle column) compared to age matched WT (first column). Moreover the level of expression in *math5*-nulls was similar to that observed after a 7 day binocular enucleation (last column). Dashed lines delineate the border of dLGN. Scale bar= 200 μm.

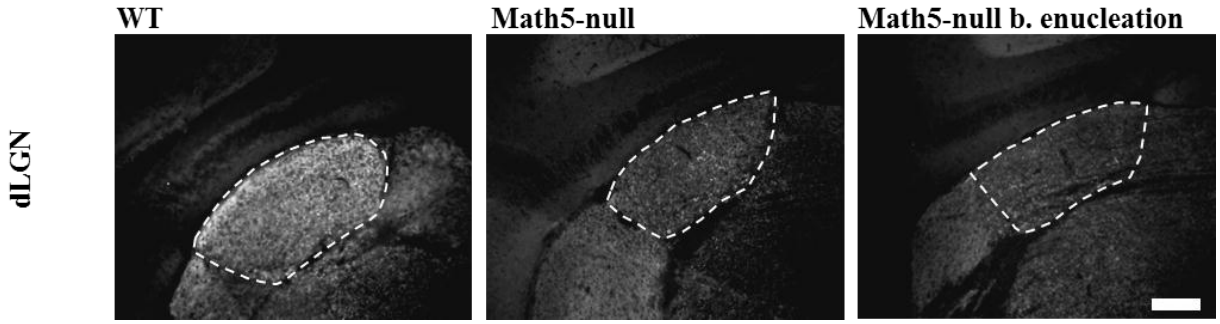

Figure 5

Ultrastructural examination of dLGN in WT and *math5*-nulls.

Electron microscopy images revealing the ultrastructure of dLGN in WT (Top panel) and *math5*-nulls (bottom panel). In WT, terminals corresponding to retina (RLP: Round, Large, and Pale), cortex and brainstem (RSD: Round, Small, and Dark) were present. No RLP profiles were found in *math5*-nulls, whereas RSDs were readily detected. Note the presence of round, large and dark terminals (RLD) in *math5*-nulls, which were not observed in WT. Dotted lines delineate each identified synaptic profile. Scale bar= 2 µm.

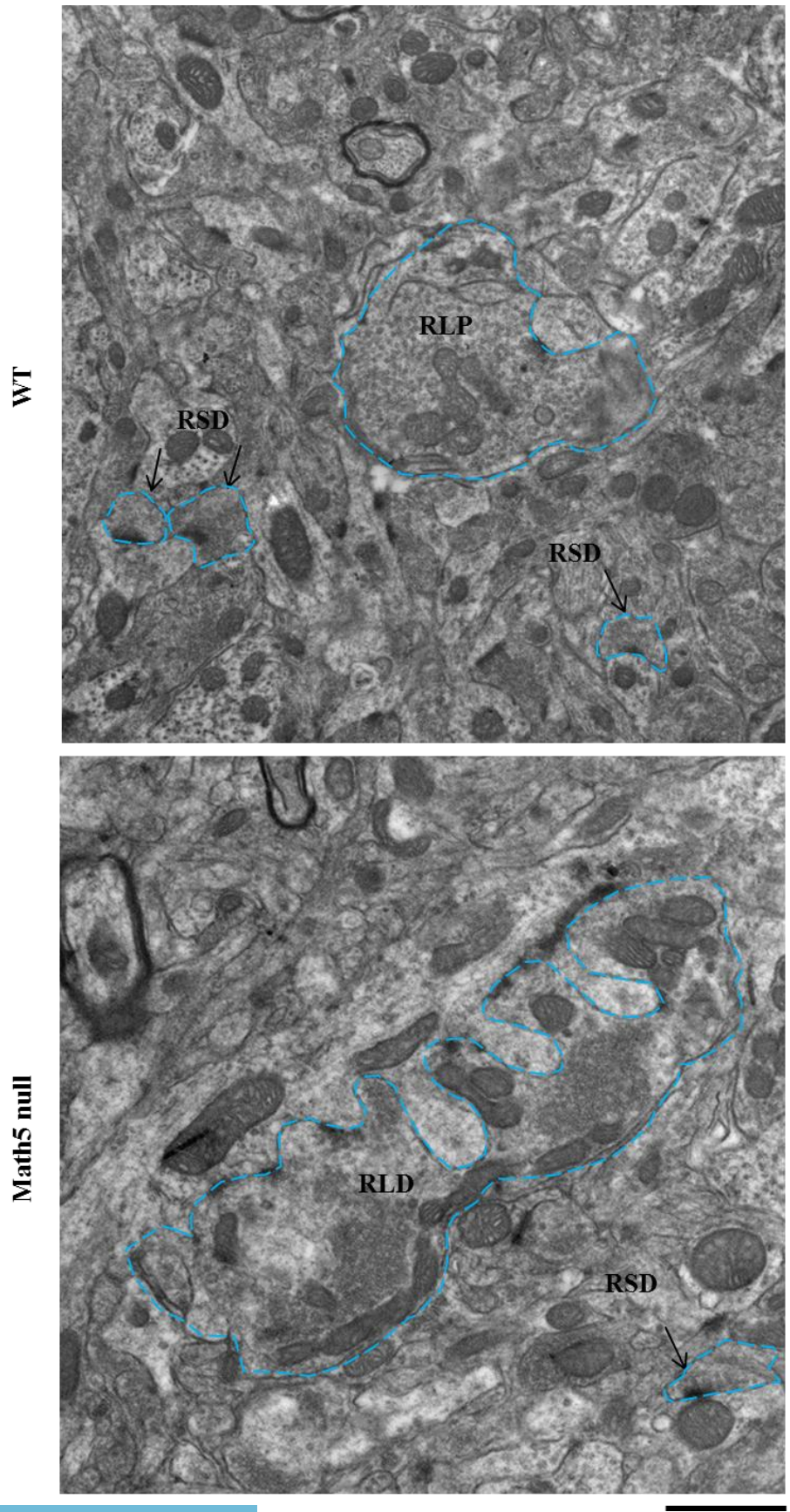

Figure 6

Biocytin filled relay cells in dLGN of *math5*-nulls.

Maximum intensity projection images of reconstructed relay cells arranged by postnatal age in *math5*-nulls. Three-dimensional reconstructions were done using a multi-photon/confocal laser scanning microscope. Targeted neurons were imaged with a C-Apochromat 40x (1.2 n.a) water immersion objective lens, and 3-D datasets were compiled from a sequential series of optical slices with a step size through the Z-axis of 0.48-0.58 μm. 3-D rendered Z-stack datasets were analyzed using Volocity software (Improvision). Scale bar= 58 μm.

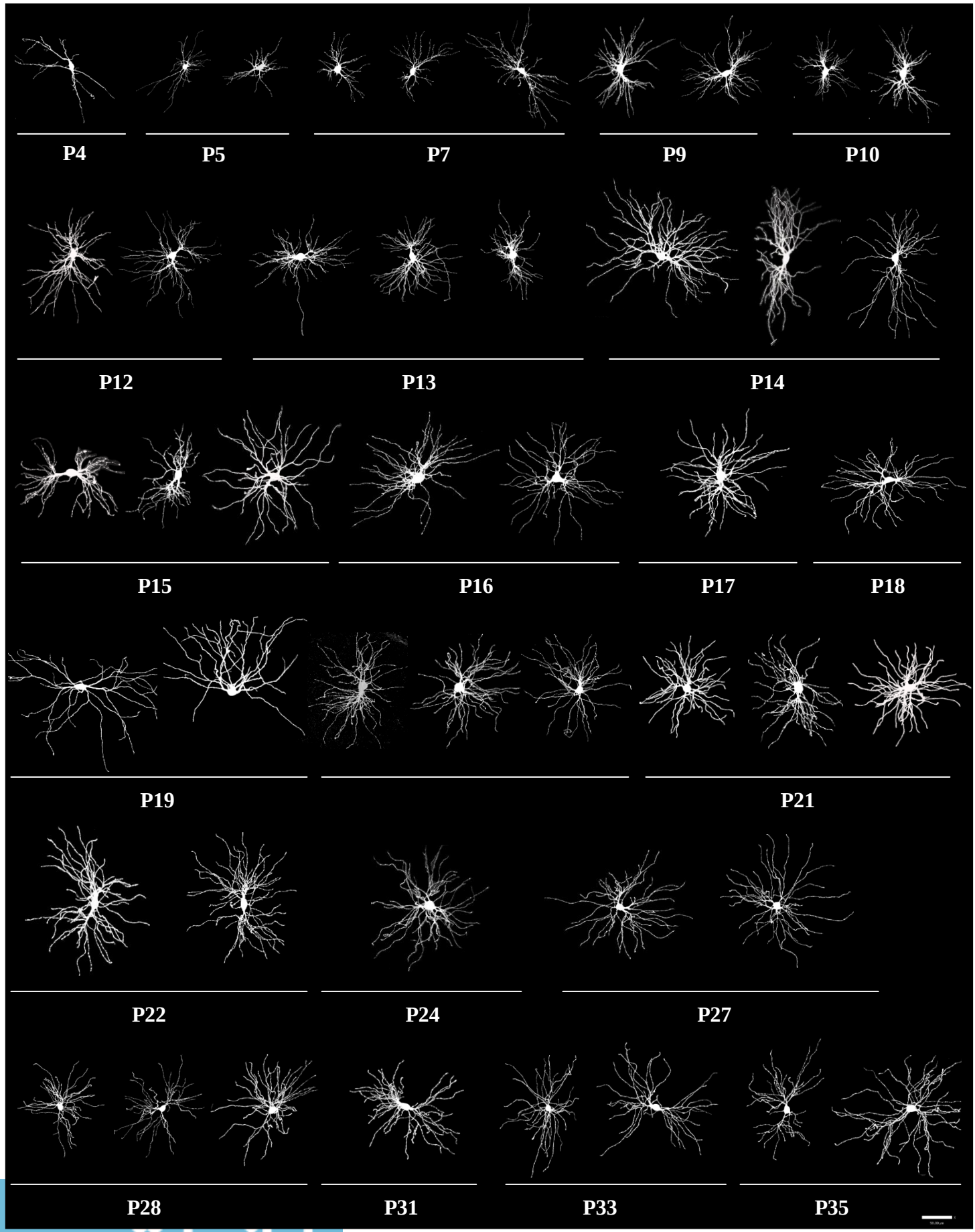

Figure 7

Analysis of dendritic and soma surface area for relay cells in WT and *math*-nulls

Left panel: scatter plots of surface area (SA) as a function of age in WT (black, *n*=69) and *math5*-nulls (red, *n*=55). Each dot represents a single relay cell. Right panel: line plots representing mean SA ±SEM as a function of postnatal week. Asterisk (*) indicates statistical significance between WT and *math5*-nulls (*t*-test, $p<0.05$)**. A**. In WT, there was a significant increase in dendritic SA between weeks 1-3, and SA stabilized thereafter. In *math5*-nulls, dendritic SA peaked by week 3 but then it was reduced in weeks 4-5. During week 2, dendritic SA was significantly higher in *math5*-nulls, but was smaller than WT in week 5. **B.** Soma SA remained constant throughout postnatal weeks 1-5 in WT. In *math5*-nulls, a peak in soma SA was apparent at week 3, with a significant reduction observed in week 5. Overall, soma SA in *math5*-nulls was significantly smaller than WT.

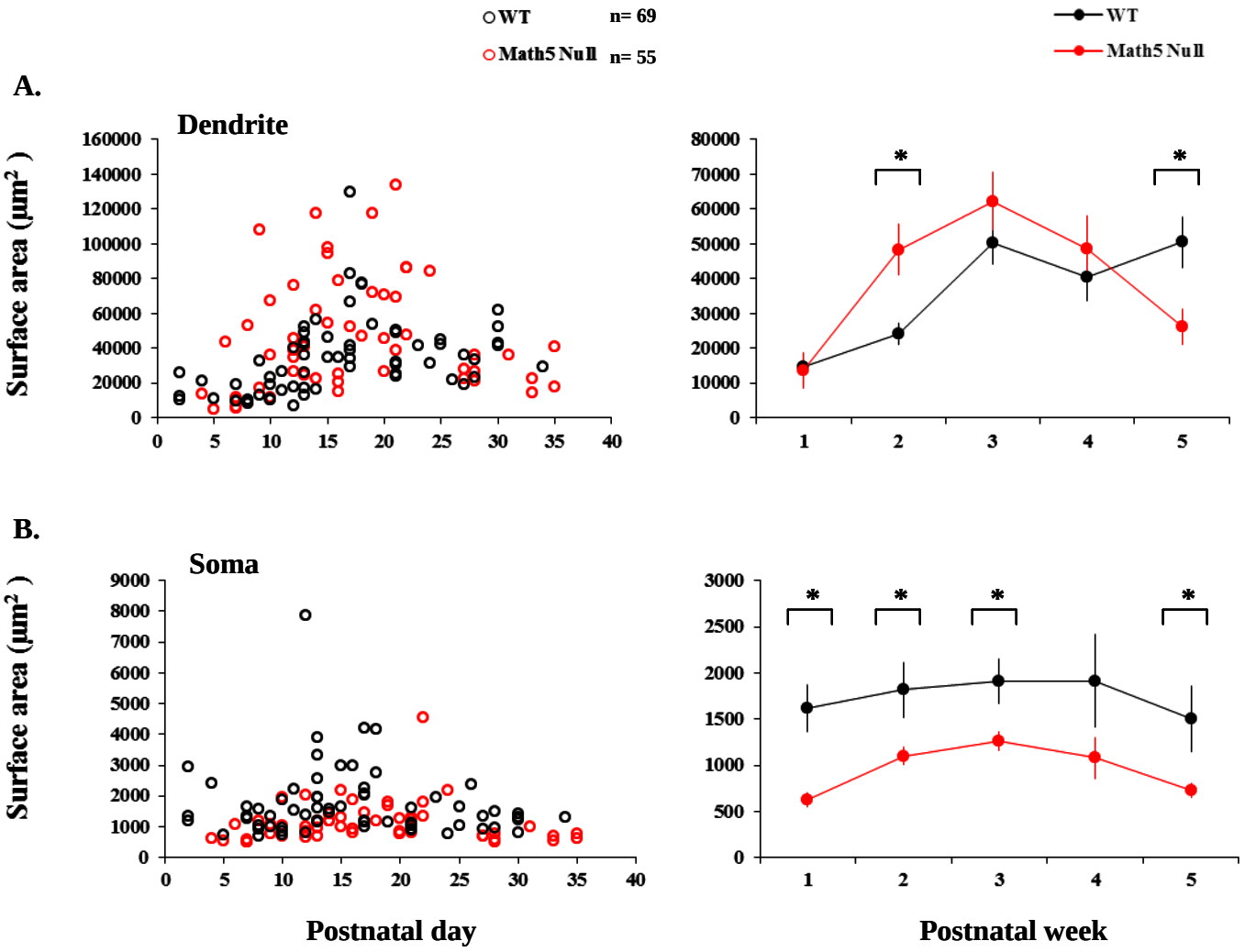

Figure 8

Analysis of dendritic field for relay cells in WT and *math5*-nulls.

Left panel: scatter plot showing dendritic field, defined as the 3-D space occupied by dendrites of a single cell, at different ages in WT (black, n=82) and *math5*-nulls (red, n=58). Each dot represents a single relay cell. Right panel: line plots depicting mean dendritic field ±SEM as a function of postnatal week. Statistical significance between corresponding age groups in WT (black) and *math5*-nulls (red) is denoted by (*, t-test, p<0.01). In WT, dendritic field increased significantly between weeks 1-3 and showed no changes afterwards. Note that WT and *math5*-nulls had similar field dimensions during weeks 1-4. By week 5, *math5*-nulls were significantly smaller than their age matched WT counterparts.

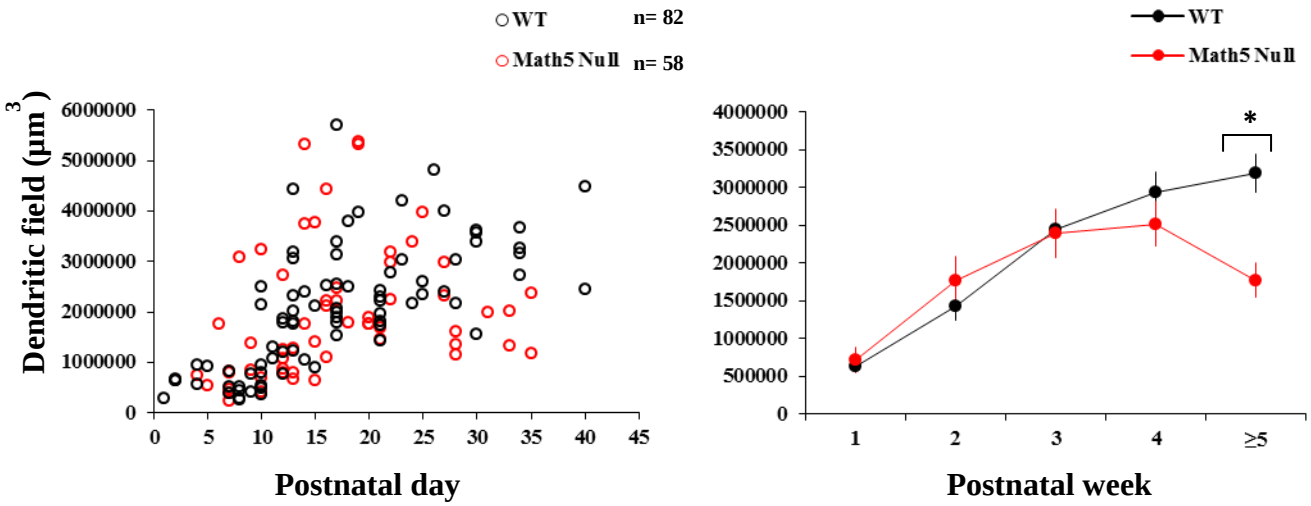

Figure 9

Analysis of dendritic complexity of relay cells for WT and *math5*-nulls.

A. Schematic depicting the centrifugal method employed for assessing dendritic complexity. This was done by counting the total number of dendritic segments as well as defining their branch order. Primary order dendrites (1º) were those that stemmed from the soma, and subsequent branching was identified as an increasing order (2º, 3º, 4º, etc.). **B**. Left panel: scatter plot of the total number of dendritic branches as a function of age in WT (black, *n*=40) and *math*-nulls (red, *n*=51). Each dot represents a single relay cell. Right panel: line plots of the mean number of branches ±SEM as a function of postnatal week. Statistical significance between corresponding age groups in WT (black) and *math5*-nulls (red) is indicated by (*, *t*-test, $p<0.05$). Note the exuberant branching in *math5*-nulls during week 2. **C.** Line plots depicting the mean number of branch points±SEM as a function of branch order at different postnatal weeks in WT (right panel) and *math5*-nulls (left panel). Branching patterns were conserved between weeks 2-5 in WT, whereas in *math5*-nulls it was highly variable. Note the increased branching in week 2.

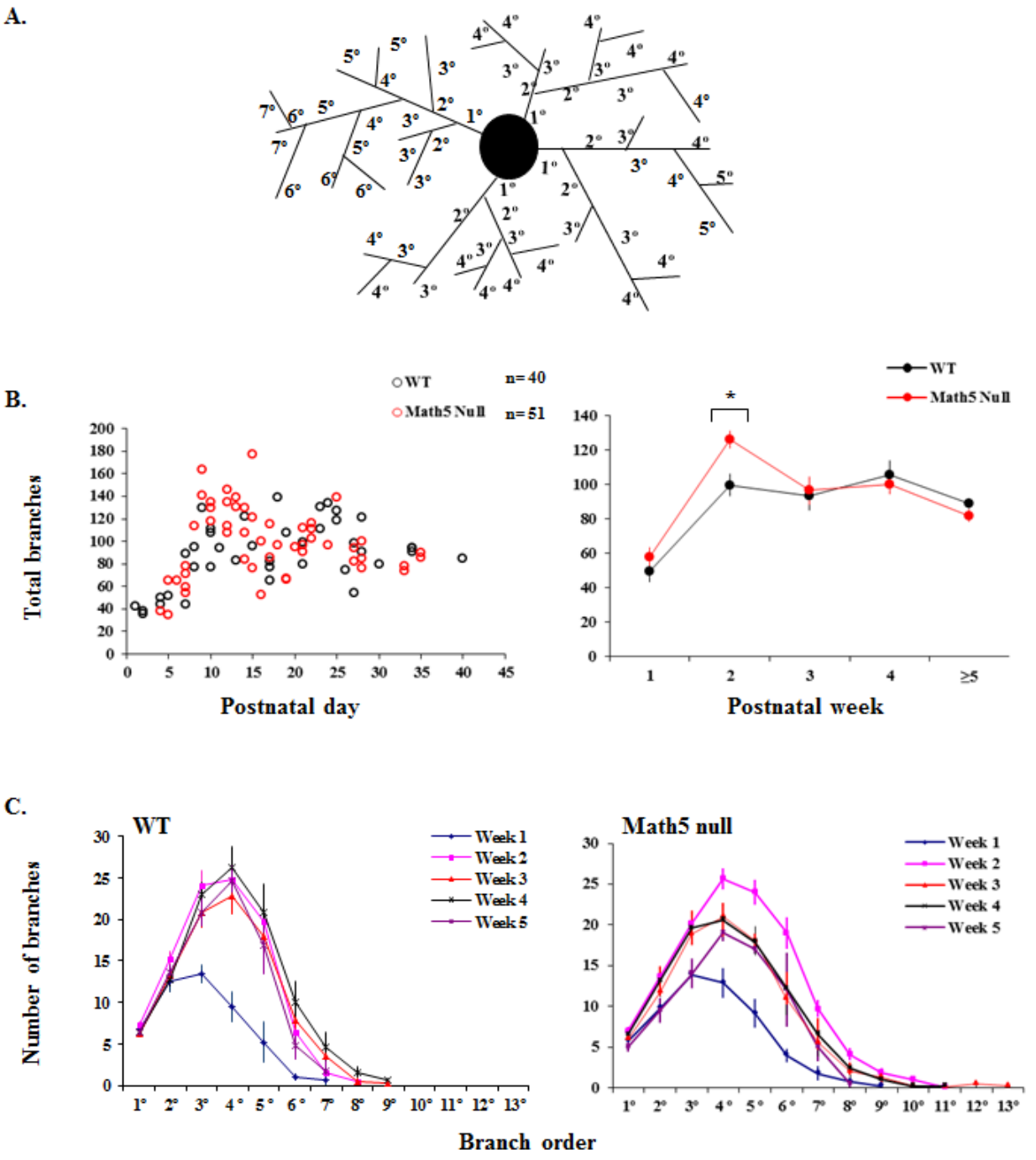

Figure 10

Analysis of dendritic branching patterns of relay cells for WT and *math5*-nulls.

Branching patterns are compared between WT (black line) and *math5*-nulls (red line) at different postnatal weeks. Statistical significance is denoted by (*, *t*-test: week 1, $p<0.01$; week2, branch orders 6-8, $p<0.0001$ and branch orders 9-10, $p<0.01$; week 5, branch orders 2-4, $p<0.05$) and error bars depict ±SEM. In both groups, relay cells had 6-7 primary dendrites, with the bulk of branching occurring between 3^{rd}-5^{th} orders. Some cells branched up to the 9^{th} order in WT. By contrast, branching order was as high as 13 in *math5*-nulls. During week 1, *math5*-nulls had increased numbers of 6^{th} order branches. During week 2, *math5*-nulls had more of the 6^{th}-10^{th} order segments. During weeks 3-4, branching patterns were similar in WT and *math5*-nulls. Whereas in week 5, *math5*-nulls had reduced numbers of 2^{nd}-4^{th} order branches.

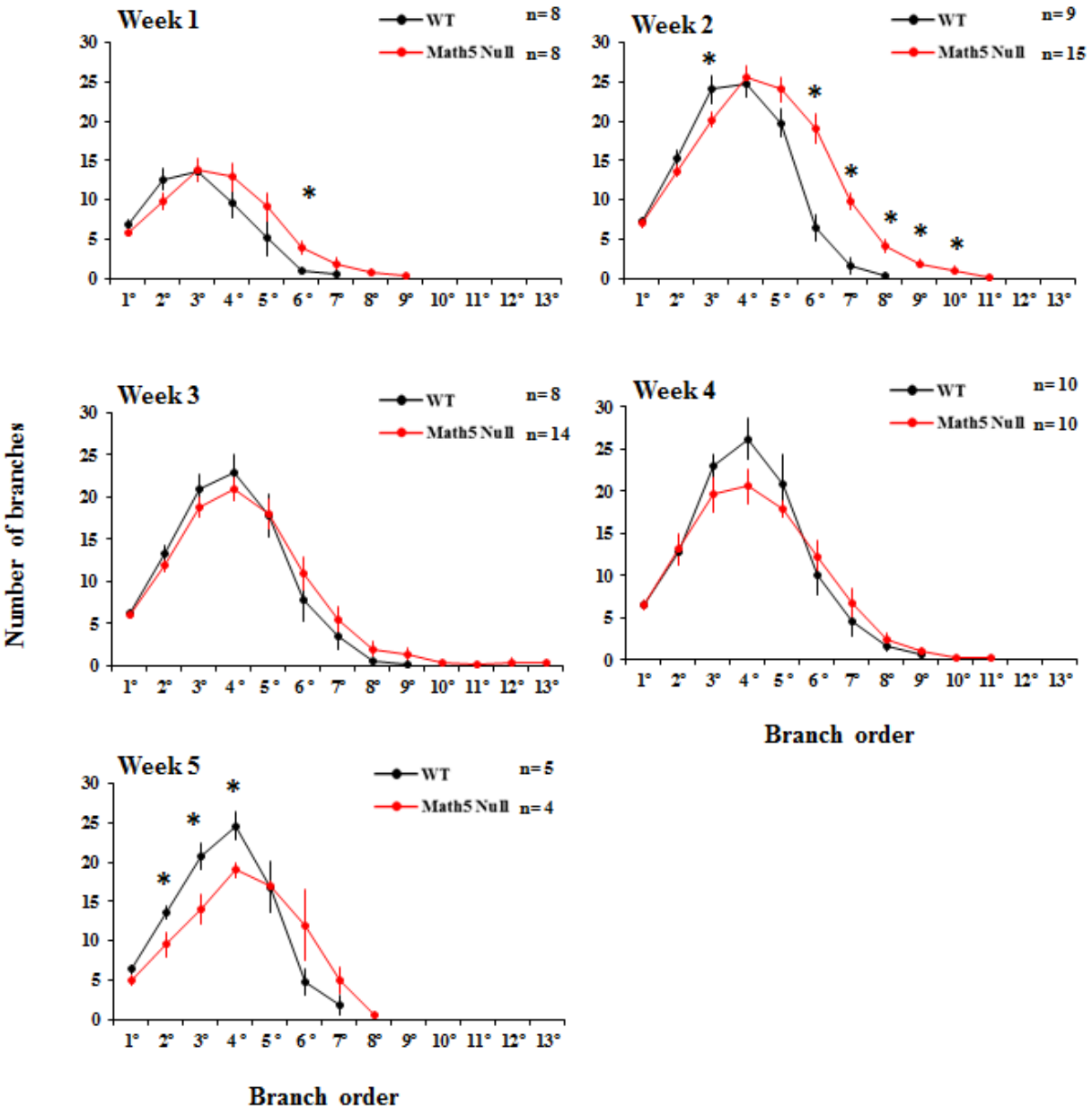

Figure 11

Cell class specificity and corresponding regional preferences in dLGN of *math5*-nulls.

A. Maximum intensity projection images of 3D rendered relay neurons in *math5*-nulls showing that the three morphologically identified cell classes in WT were present in these mutants. Left panel: Y-cells have radially oriented dendritic arbors. Middle panel: W- cells have a hemispherical morphology. Right panel: X- cells have a bi-conical morphology. Scale bar=58 µm. **B.** Scatter plot depicting the location of relay cells in the dLGN of *math5*-nulls. Dashed lines represent superimposed coronal slices (300 µm thick) delineating the outlines of dLGN. Colors depict identified cell types (Y: green; W: blue, X: red). Y- and W- cells seemed to retain their regional preferences in *math5*-nulls, where Y- cells were located in central band throughout the nucleus, and W- cells formed a shell around the dorso-ventral border of the dLGN. However, X-cells extended well beyond the monocular segment. For WT comparison, see Appendix I- Krahe and El-Danaf et al., 2011, submitted.

A.

B.

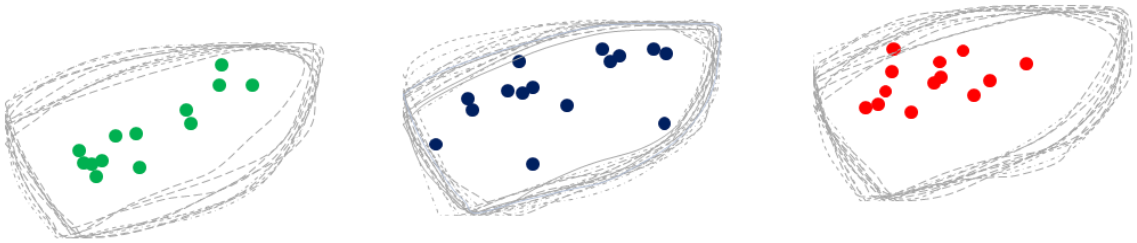

Y W X

Figure 12

Analysis of dLGN area in WT and *math5*-nulls.

A. Coronal sections of dLGN stained for nissl at different postnatal weeks in WT (top row) and *math5*-nulls (bottom row). In *math5*-nulls, dLGN boundaries were well delineated; however the nucleus was highly reduced in size compared to WT. Asterisk displays the 100 µmx100 µm region where cell density counts were made (see fig. 13; vLGN: ventral lateral geniculate nucleus). **B.** Left panel: scatter plot showing dLGN area as a function of age in WT (black, *n*=51) and *math5*-nulls (red, *n*=79). Each dot represents a single dLGN section. Right panel: line plots describing mean dLGN area ±SEM as a function of postnatal week. Statistical significance between corresponding age groups in WT (black) and *math5*-nulls (red) is demonstrated by (*, *t*-test: weeks 1, 3-5 $p<0.0001$; week2 $p<0.01$). In WT, there was a significant increase in dLGN area between weeks 1-3, but was stable in weeks 3-5. In *math5*-nulls, dLGN area peaked by week 3, but showed significant reduction between weeks 3-5. Compared to WT, dLGN was significantly smaller in area throughout all studied age groups in *math5*-nulls. Scale =200 µm.

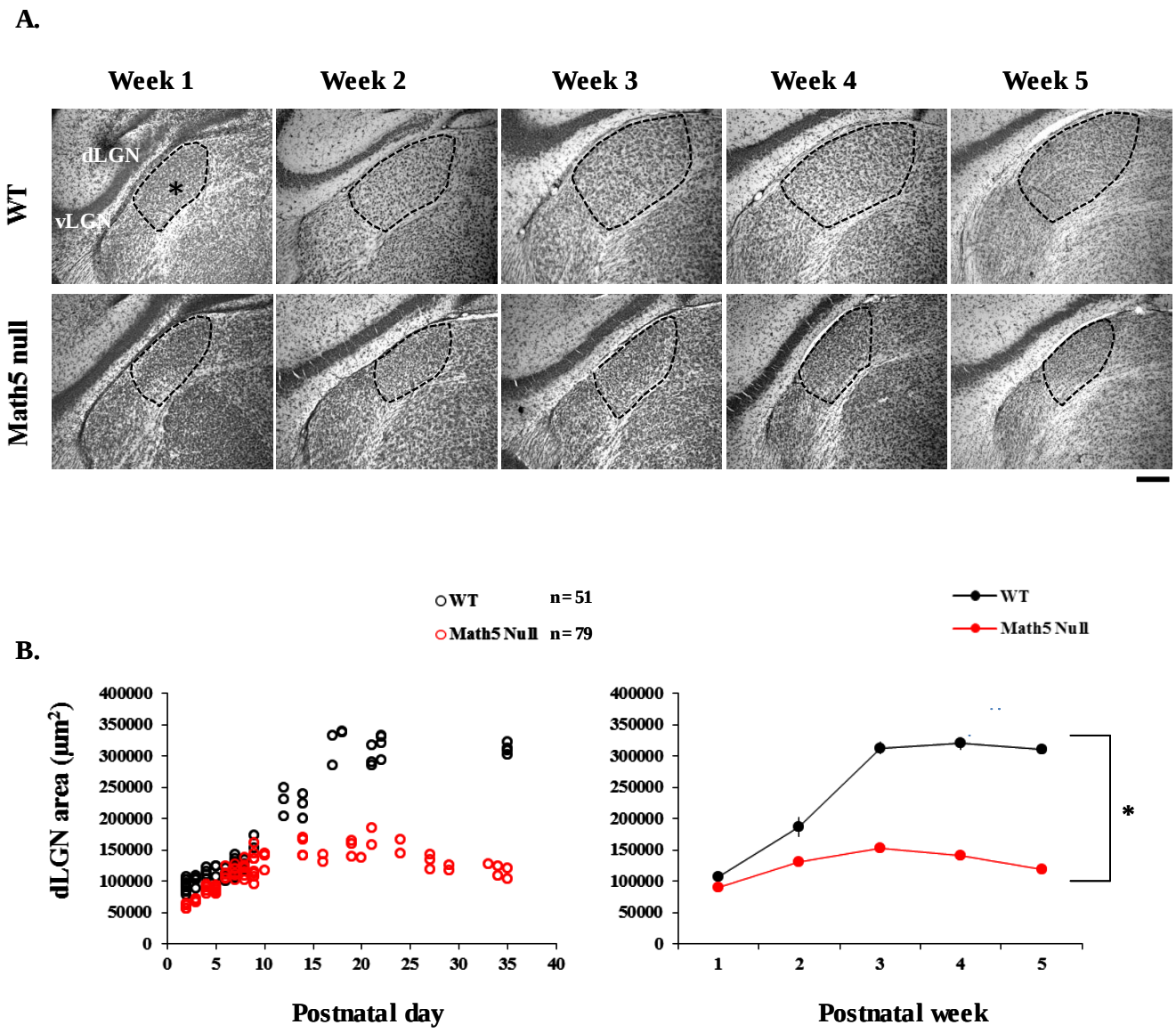

Figure 13

Cell density measurements in dLGN of WT and *math5*-nulls

A. Cell density counts were calculated from a 100 µmx100 µm region of interest that was selected from the center of representative nissl stained dLGN sections in WT (top row) and *math5*-nulls (bottom row) at postnatal weeks 1-5 (see fig. 12). **B**. Left panel: scatter plot showing cell density as a function of age in WT (black, n=19) and *math5*-nulls (red, n=38). Each dot represents a single dLGN hemisphere. Right panel: line plots describing mean cell density as a function of postnatal week. Statistical significance between corresponding age groups in WT (black) and *math5*-nulls (red) is demonstrated by (*, t-test, p<0.05) and error bars depict ±SEM. In WT, cell density counts showed no significant changes with age. In *math5*-nulls, there was a significant reduction in cell density between weeks 1-3, but remained constant between weeks 3-5. Compared to WT, cell density was significantly higher in *math5*-nulls in weeks 1-3, 5. Scale =20 µm.

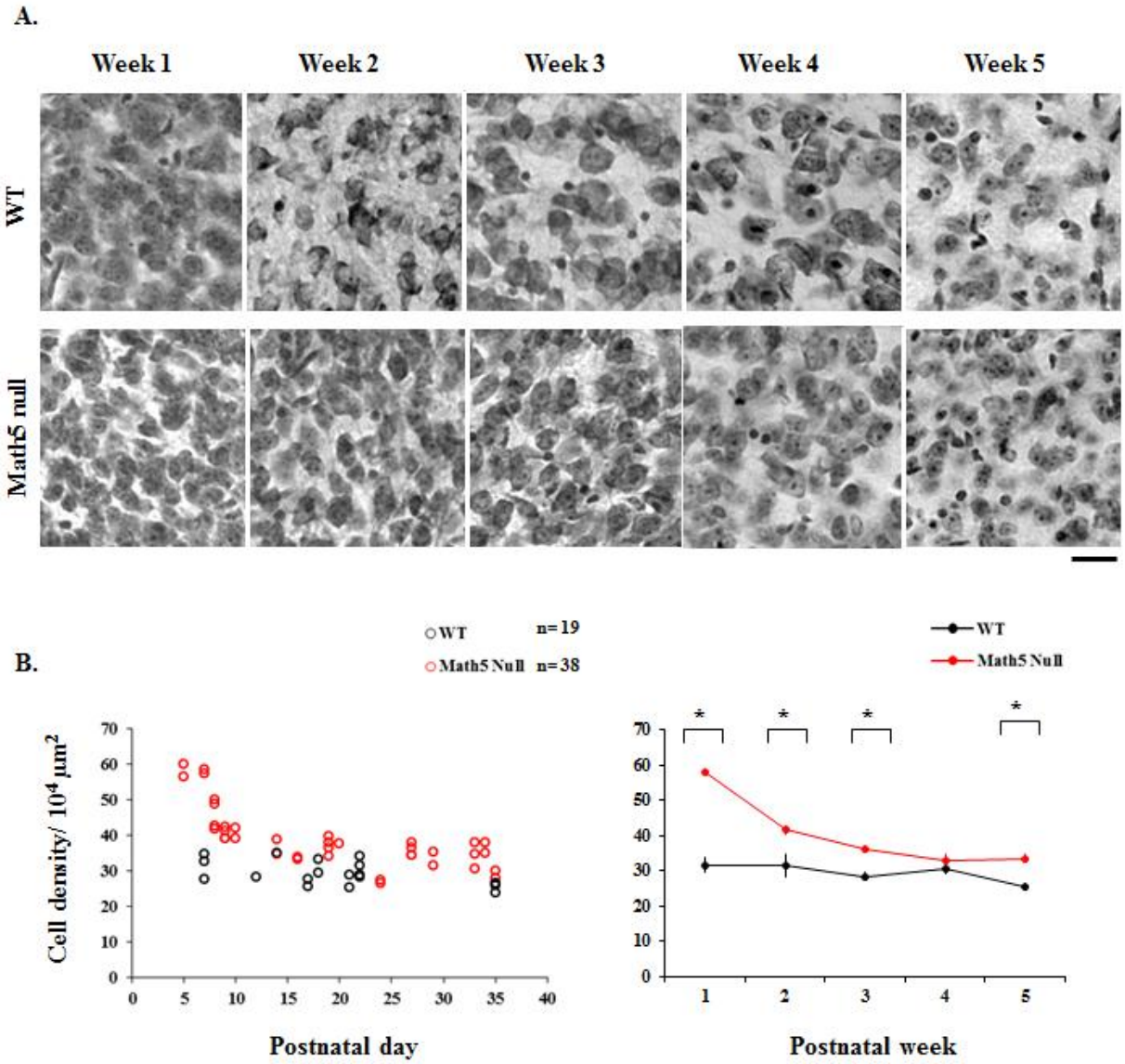

Figure 14

Active membrane properties of relay cells in WT.

Examples of voltage responses to current injections and I-V relations of relay cells in WT mouse. As early as week 1, hyperpolarization elicited a large depolarizing sag mediated by the mixed cation conductance (I_h). A low threshold Ca^{2+} spike (LTS) was observed after termination of hyperpolarization. High and sustained depolarization elicited a train of action potentials. However, with age, there was an emergence of outward rectification (I_A) which caused a delay in the firing of action potential, as well as spike frequency accommodation, both of which were observed during week 3. Far right panel: I-V relations that correspond to cells shown in left measured at steady state. Note the difference in the slope between weeks 1 and 3, which can be explained by reduction in membrane resistance (see Fig. 16). Also note the inward and outward rectification during hyperpolarization and depolarization which correspond to I_h and I_A, respectively.

WT

Week 1

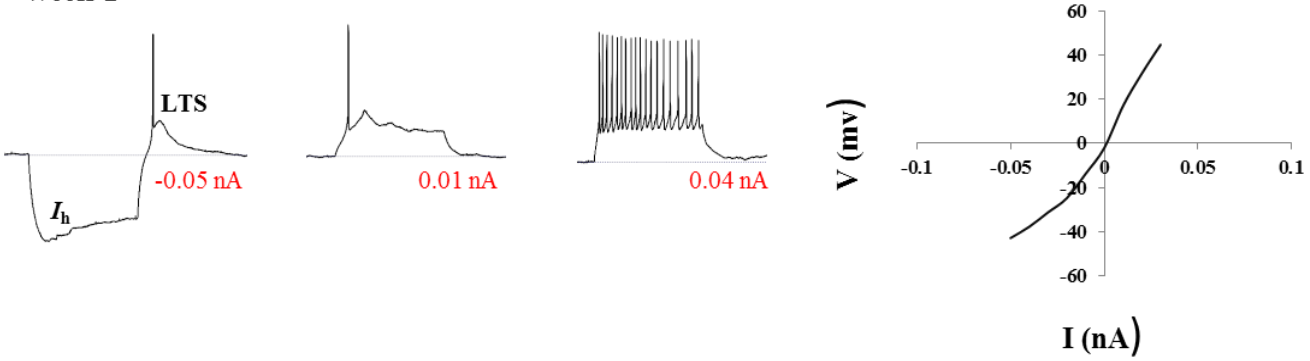

Week 3

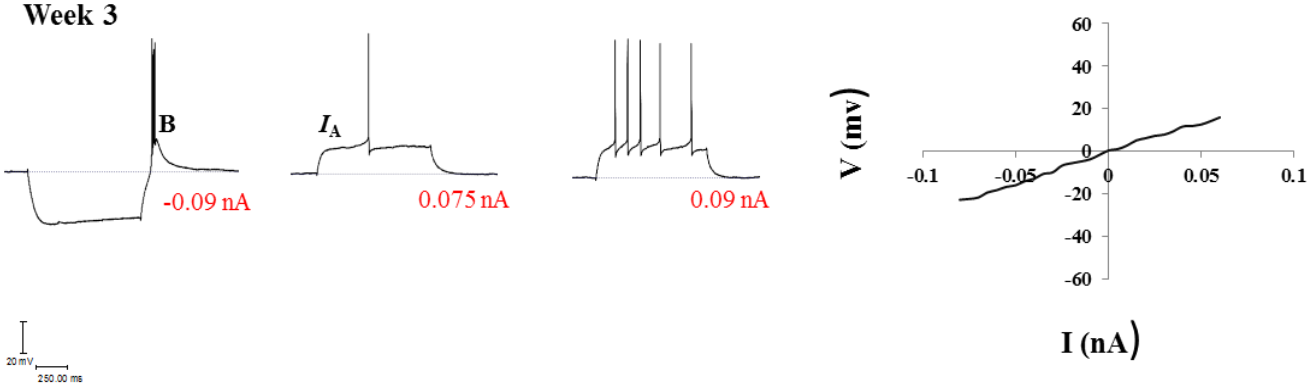

Figure 15

Active membrane properties of relay cells in *math5*-nulls.

Examples of voltage responses to current injection of relay cells in *math5*-nulls at postnatal weeks 1-5. *Math5*-nulls possess the full complement of membrane properties that are seen in WTs. At week 1, hyperpolarization activated mixed cation conductance (I_h), low threshold Ca^{2+} spike (LTS) and a train of Na^+ spikes were observed. By week 3, burst firing (B) was evident, as well as the emergence of the outward rectifying K^+ conductance (I_A), and spike frequency accommodation. Far right panel: I-V relations that correspond to cells shown in left (blue) measured at steady state and compared to values grouped by postnatal week (red). Note the steepness of the slope during weeks 1-2, indicating high input resistance (Fig. 16). Also note the presence of inward (during hyperpolarization) and outward (during depolarization) rectification that correspond to I_h and I_A, respectively. Overall, the development of the intrinsic membrane properties was spared in *math5*-nulls.

Math5 null

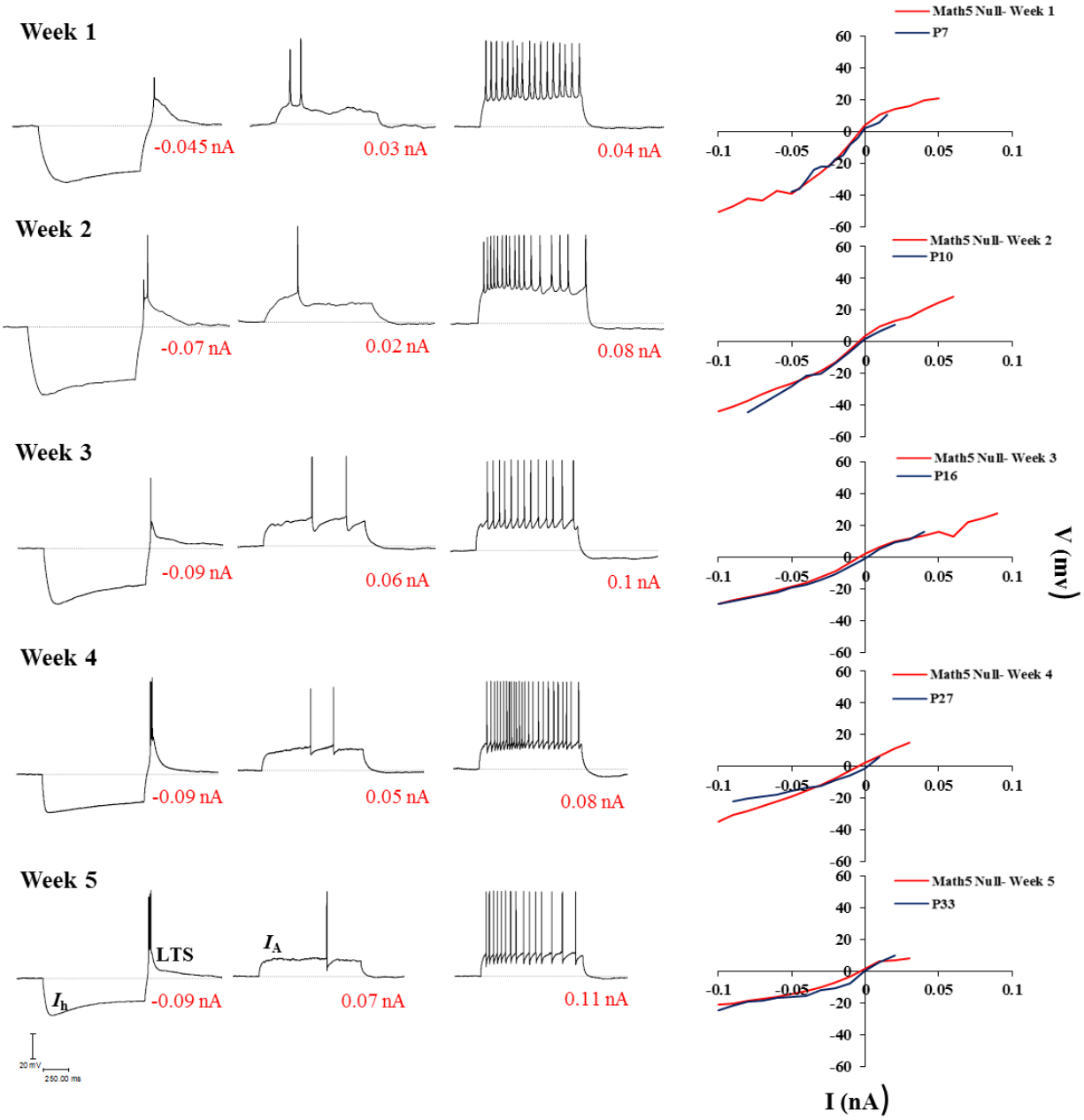

Table 1

Intrinsic membrane characteristics of relay cells in WT and *math5*-nulls.

A comparison of various active and passive membrane properties of relay cells between WT and *math5*-nulls at <P14 and ≥P14. Resting membrane potential, spike height and spike duration in WT were compiled from Macleod et al. (1997) and are denoted by †, where the values reported for before and after P14 correspond to P6-15 and P16-35, respectively. The remaining characteristics in WT were obtained from Dilger et al. (2011). The mean ±SEM and percent incidence of each property was calculated, and the total number of cells is indicated in parentheses. Statistical significance between WT and *math5*-nulls is indicated by (*; means: *t*-test, $p<0.05$; percent incidence: χ^2 test).

Table 1. Intrinsic membrane properties		
Property	WT	Math5 null
Tau (ms)		
Before P14 *	44.0 ± 2.9 (23)	35.9 ± 2.4 (20)
After P14 *	38.2 ± 2.6 (28)	21.3 ± 1.2 (41)
Input resistance (MΩ)		
Before P14 *	653.6 ± 66.2 (28)	1254.4 ± 51.0 (65)
After P14 *	365.4 ± 35.3 (34)	539.5 ± 24.2 (63)
Resting membrane potential (mV)		
Before P14	-52.2 ± 1.5 (57)	-61.4 ± 0.8 (73)
After P14	-61.4 ± 2.4 (62)	-59.7 ± 2.2 (62)
Spike height (mV)		
Before P14	41.0 ± 1.6 (57)	44.2 ± 1.5 (49)
After P14	46.4 ± 2.2 (62)	47.3 ± 2.0 (41)
Spike duration (ms)		
Before P14	1.6 ± 0.2 (57)	2.7 ± 0.1 (49)
After P14	0.9 ± 0.2 (62)	1.5 ± 0.1 (41)
Low-threshold Ca^{2+} spike		
Before P14	94.8% (36)	90.6% (64)
After P14	100.0% (31)	100.0% (59)
Low-threshold Ca^{2+} burst		
Before P14 *	41.9% (31)	32.8% (64)
After P14 *	54.3% (35)	61.0% (59)
Mixed cation conductance		
Before P14	77.12% (35)	87.5% (56)
After P14	86.7% (30)	79.7% (59)
A-type K^+ conductance		
Before P14 *	85.7% (35)	38.7% (62)
After P14	87.3% (24)	80.4% (51)

Figure 16

Passive membrane properties in WT and *math5*-nulls.

A. Scatter plot showing changes in cell resistance by postnatal age in WT (left column, black, *n*=63) and *math5*-nulls (middle column, red, *n*=135). Each dot represents a single cell. Input resistance decreased with age, and in both cases, data could be fit with an exponential curve (WT: r= 06.7; *math5* nulls: r=0.74). Right column: bar graphs showing mean input resistance +SEM in WT (black) and *math5*-nulls (red) at <P14 and ≥P14. Asterisk denotes statistical significance (*, *t*-test, $p<0.0001$). Overall, *math5*-nulls had higher input resistance compared to WT. **B.** The decay constant tau (τ) was determined by a single exponential fit to a -0.01 nA current injection for the first 200 ms of recording. In WT, τ was relatively stable with age (far left panel, black, *n*=51), but showed significant reduction in *math5*-nulls and data could be fit to a single exponential curve (middle panel, red, *n*=61, r= 0.75). Far right panel: *math5*-nulls (red) had a significantly shorter τ compared to WT (black) prior to and after P14. Asterisk denotes statistical significance (*, *t*-test: <P14, $p<0.05$; ≥P14, $p<0.0001$).

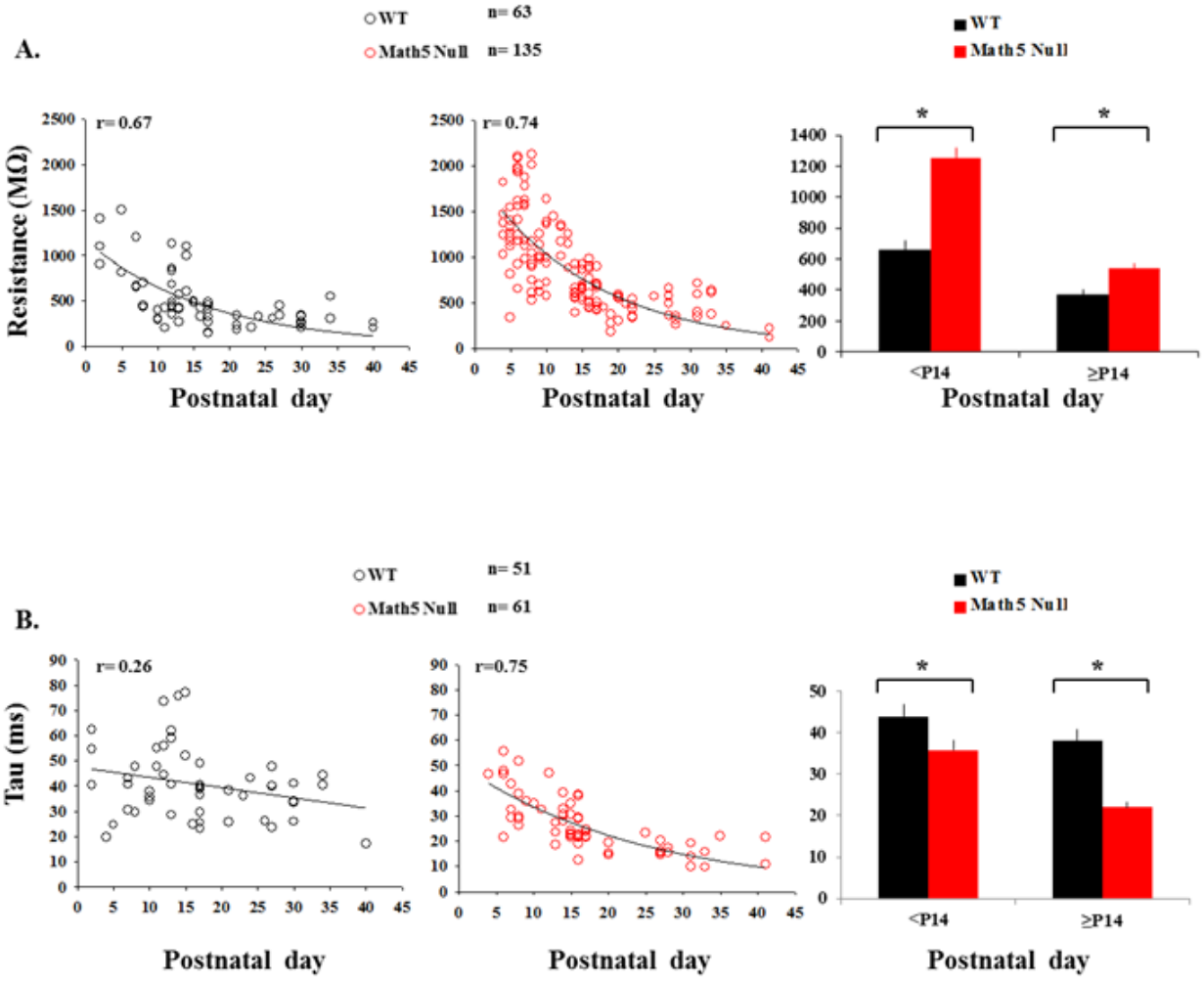

Figure 17

Characteristics of action potential in *math5*-nulls.

A. Representative examples of Na^+ spikes seen after membrane depolarization in *math5*-nulls at P5, 15, and 31. **B**. Duration of spikes at half-height decreased with age and data could be fit with a single exponential curve (left panel, *n*=92, r=0.76). In contrast, amplitude was established early and remained constant with age (right panel, *n*=92, r=0.2). In both scatter plots, each dot represents a single relay cell.

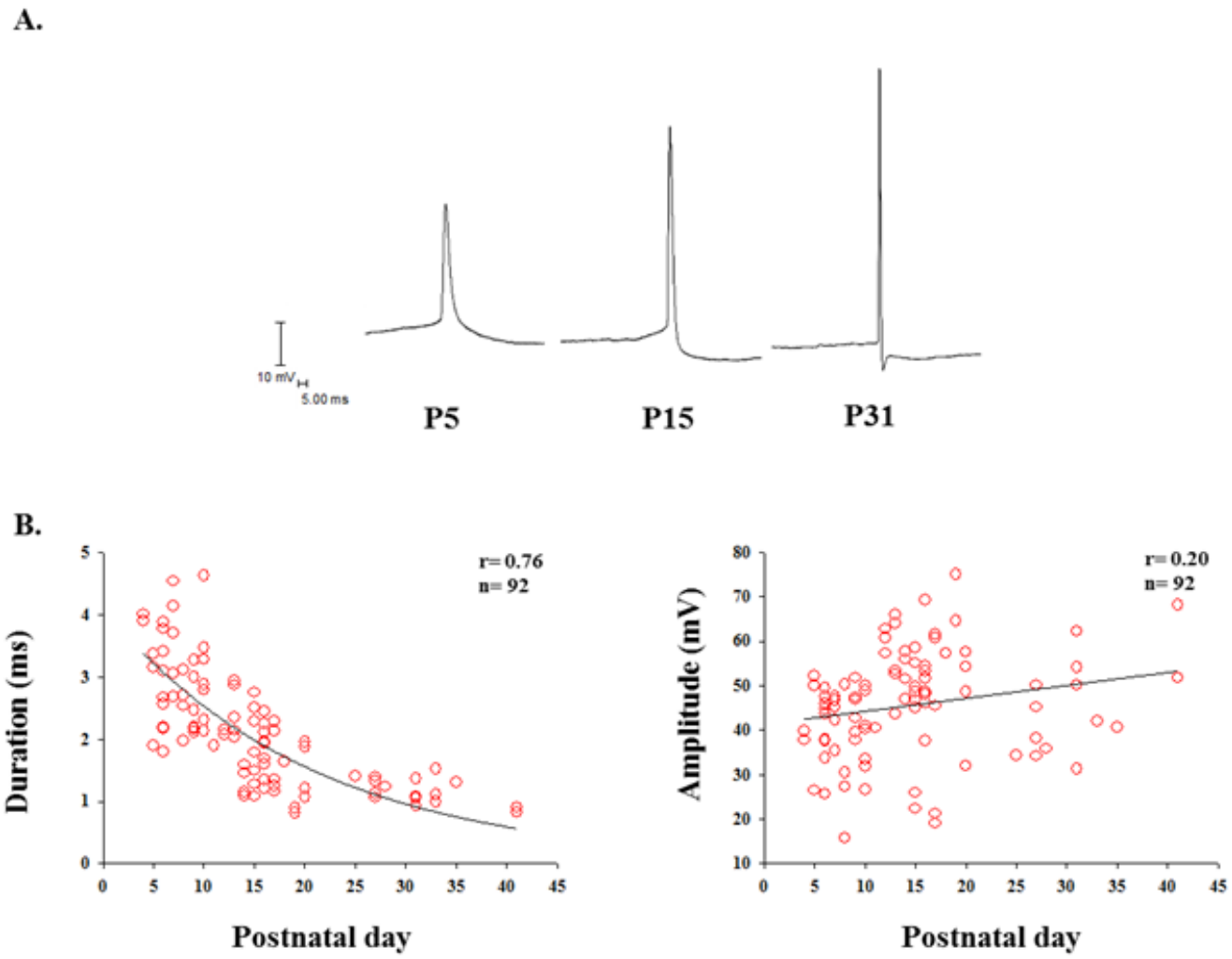

Figure 18

Frequency and latency analysis of voltage responses to a wide range of current pulses that elicited action potential firing.

A-B. Examples of repetitive firing characteristics in *math5*-nulls in response to increasing current intensity at P10 and P27 (top panels). Beneath each trace are plots describing different characteristics of action potential firing. Far left column: Line plot depicting firing frequency as a function of current intensity, showing that frequency increased with membrane depolarization. Middle column: Line plot of latency as a function of current intensity. Latency to spike firing decreased with increasing current intensity. Far right column: Line plot of the interspike interval as a function of spike number at different current intensities. Relay cells showed frequency adaptation to spike firing. **C**. Scatter plots showing the slope of firing frequency as a function of current intensity (far left) and latency to spike firing by age (right column). These characteristics were established early and remained constant with age. Each dot represents a single relay cell (n=78).

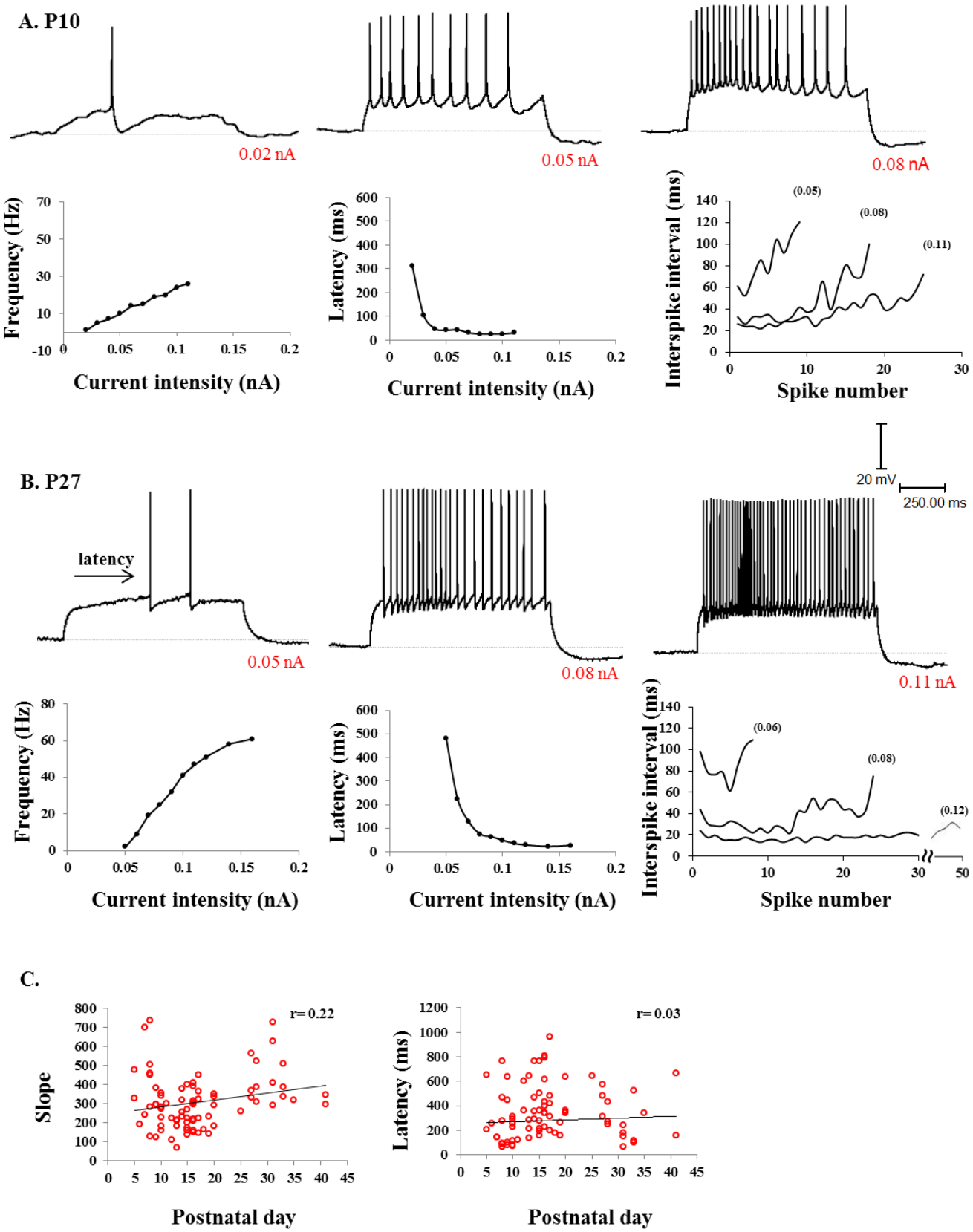

Figure 19

Spatial extent of corticogeniculate projections.

A. *Math5*-nulls were crossed with the *golli*-τ-GFP mouse in order to visualize corticogeniculate projections arising from layer VI (Jacobs et al., 2007). Coronal sections of the dLGN showing cortical terminals labeled with τ-GFP (green) in *math5*-null crosses (bottom row) and age matched littermate controls (top row). Dashed lines delineate the border of dLGN (vLGN: ventral lateral geniculate nucleus). Far right: insets depicting retinal projections labeled with CTB (Alexa Fluor 594). Note the absence of CTB labeled retinal terminal fields in *math5*-nulls. **B.** Scatter plot illustrating the spatial extent of corticogeniculate axons in dLGN as a function of age in *golli*-τ-GFP and littermate controls (black) and *math5*-null crosses (red). Error bars represent ±SEM. In both cases, data can be fit with a sigmoidal curve (r=0.99). In *math5*-nulls, innervation was highly accelerated (m=4.98 WT; m=3.23 *math5* nulls). Values for *golli*-τ-GFP transgenics were obtained from Seabrook et al. (2010). Scale = 200 μm.

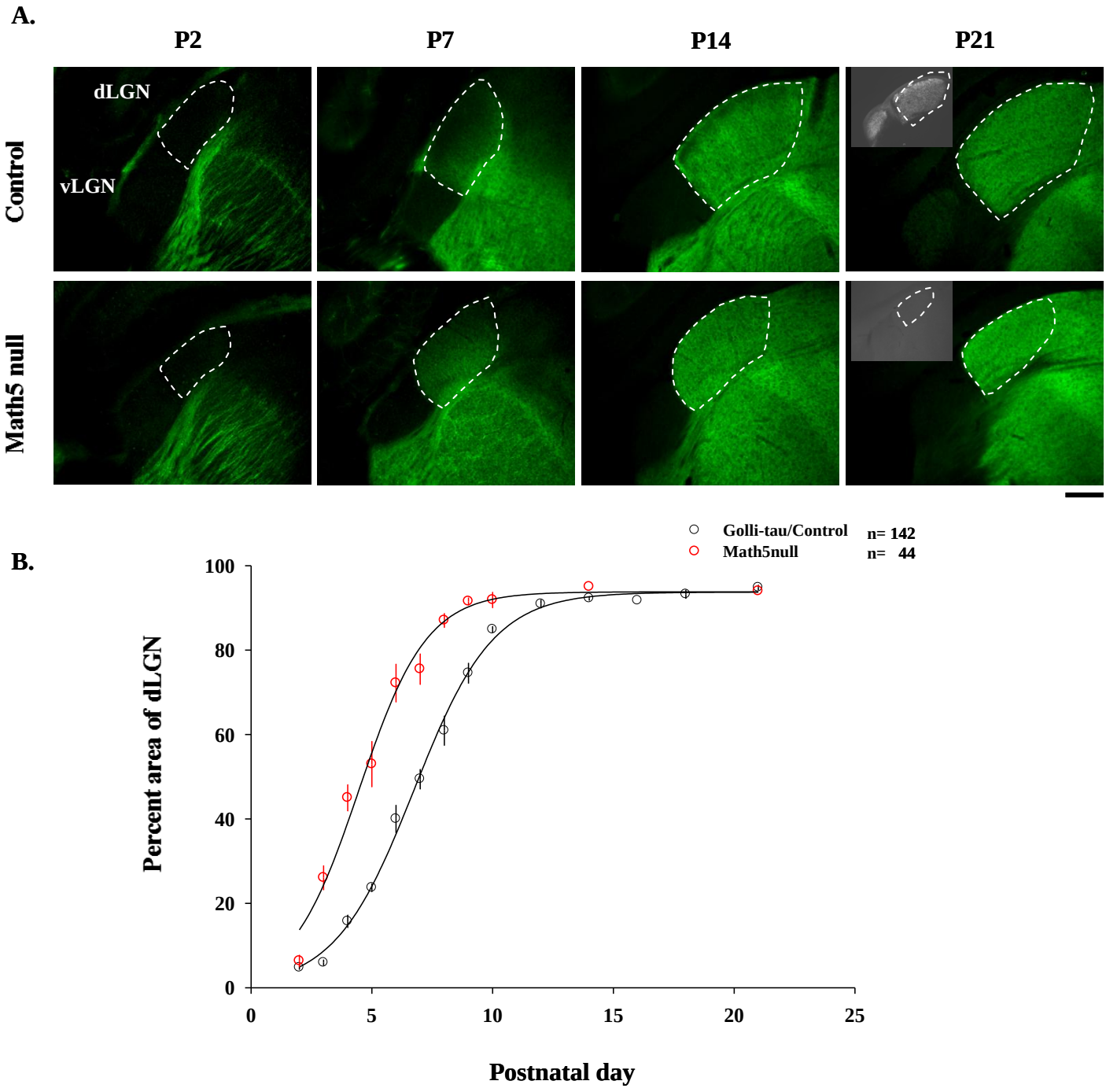

Figure 20

Functional connectivity of corticogeniculate terminals in *math5*-nulls.

A. Synaptic responses recorded from relay cells evoked by stimulation of corticogeniculate afferents. Paired-pulses were delivered with an inter-stimulus duration of 100 ms, and paired-pulse ratios (PPR) were calculated. Typically, corticogeniculate stimulation elicited facilitation, meaning that the amplitude of the second evoked EPSP was greater than the first one. Left panel: representative examples of paired-pulse facilitation seen after corticogeniculate axon stimulation at P8 and 14. Right panel: Scatter plot showing that the magnitude of paired-pulse ratio (PPR) in *golli*-τ-GFP transgenics (black) and *math5*-nulls (red) was similar. Each dot represents a single relay cell. **B**. Left panel: examples of paired-pulse recordings at variable inter-stimulus intervals (ISI) at P14 in *math5*-nulls. Right panel: Line plot showing the degree of facilitation as a function of ISI. The highest degree of facilitation occured at an ISI of 100 ms in both *golli*-τ-GFP transgenics (black) and *math5*-nulls (red). There was a progressive decrease in paired-pulse facilitation so that between ISI of 300 ms-1000 ms, PPR was roughly equal to 1. Taken together, these results indicate that the formation of corticogeniculate synapses is spared in the absence of retinal innervation. Values for *golli*-τ-GFP transgenics are obtained from Seabrook et al. (2010).

A.

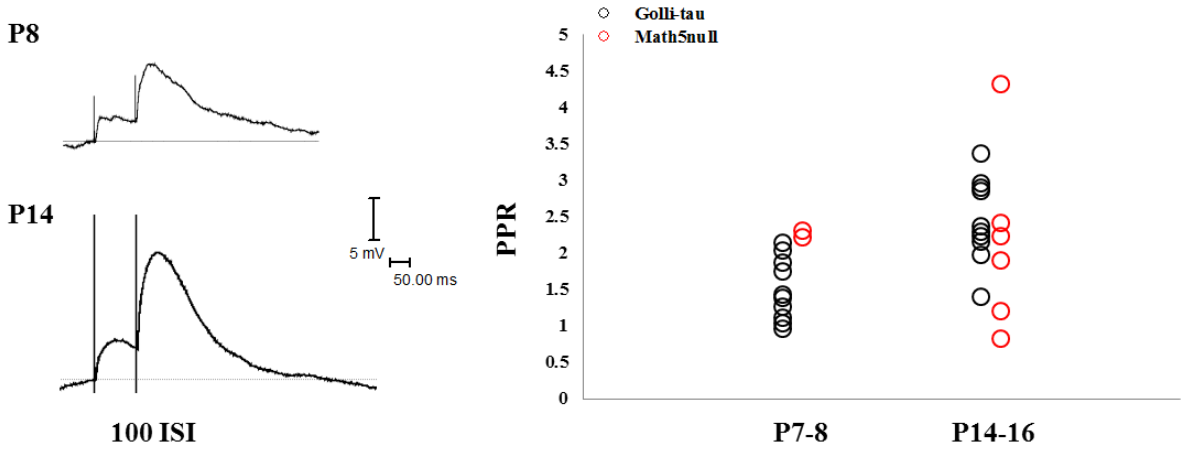

B.

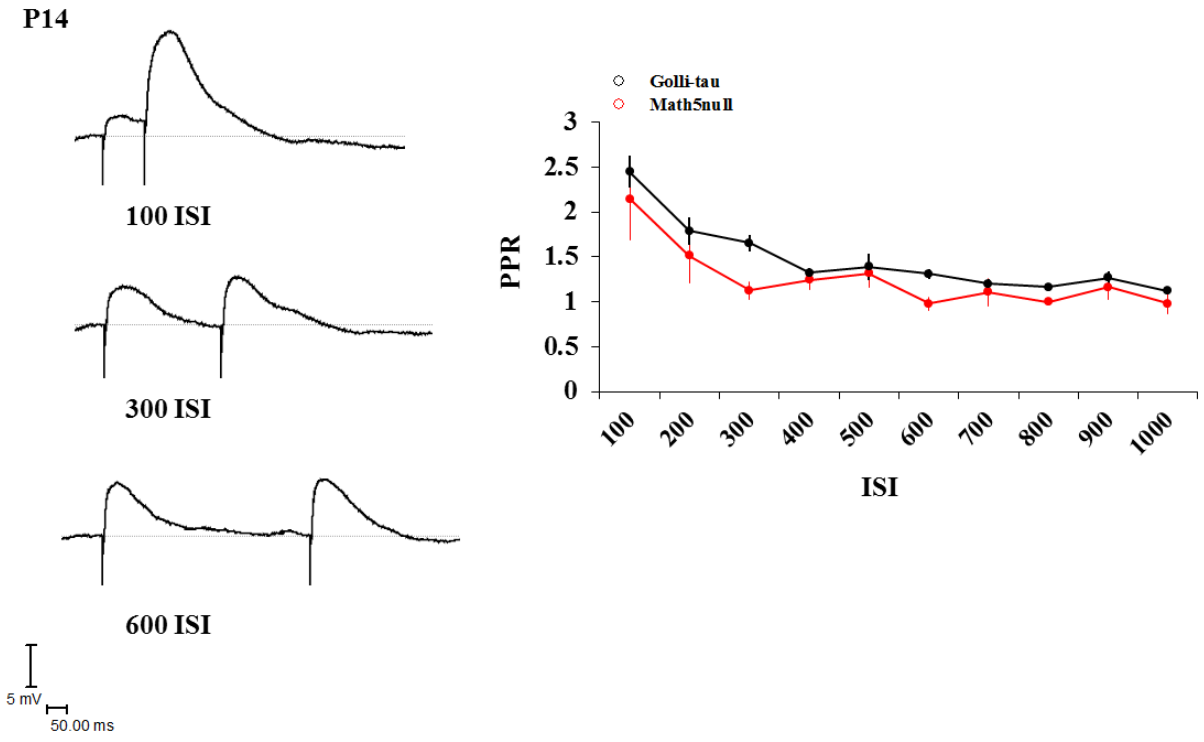

Discussion

In this study we characterized the development of relay cells in the dLGN. By adopting a loss of function approach utilizing the *math5*-null, we were also able to assess the manner in which growth and maturation of relay cells were affected by retinal innervation. Finally, we assayed the patterns of corticogeniculate innervation by crossing *math5*-nulls with *golli*-τ-GFP transgenics.

Development of relay cells in WT mouse

The development of mouse dLGN relay cells is summarized in figure 21. We show that relay cells undergo two growth spurts. The first one takes place at the end of the first postnatal week where cell class specificity and complexity are established. This is reflected by a 2-fold increase in the total numbers of dendrites, mainly those belonging to higher order segments (Fig. 9B, left panel). Moreover, cell class specification was established as early as P7 a time where cells take on distinct and highly stereotypic morphology (see Appendix I- Krahe and El-Danaf et al., 2011, submitted). In fact, they resemble the dendritic architecture of well-known relay cell types identified in such animals as cats, ferrets and primates. Perhaps, they are most similar to those reported in cat, for this reason we refer to them as X, Y and W (Friedlander et al., 1981; Stanford et al., 1981, 1983). For example, X- cells have a biconical morphology with dendrites stemming from opposite directions of the soma. Y-cells have radially symmetric dendrites that

branch out in all directions of the soma, and W- cells have hemispherical dendritic arbors (Fig. 11A). Following the second week, branching patterns are stabilized and resemble adult-like profiles. On average, relay cells have 6-7 primary dendrites, branch up to the 9th order, with the bulk of branching occurring between the 3rd and 4th orders (Fig. 9C, left panel). The second growth spurt starts at the second week and continues through the third week, where there is a gradual increase in dendritic field and length (Fig. 8). By the third postnatal week, relay cells exhibit roughly a 3-fold increase in their dendritic surface area, and their overall growth is stabilized (Fig. 7A). By contrast, soma size showed no significant differences with age (Fig. 7B). During these first few postnatal weeks, the spatial extent of the dLGN also increases. There is a 3-fold expansion in the area of dLGN that stabilized by the third postnatal week (Fig. 12). Moreover, cell density remains constant throughout this period, suggesting that developmental apoptosis occurs at earlier ages (Fig. 13; Heumann and Rabinowicz, 1980). Lastly, our results for dLGN area and cell density confirmed what has been previously reported in the mouse (Heumann and Rabinowicz, 1980; Jaubert-Miazza et al., 2005; Dilger et al., 2011).

Many of the changes reported here for mouse are similar to those found in the rat (Parnavelas et al., 1977). For example, relay cells in the rat showed that their growth occurs in two phases. An early one at P4-6, where there was a marked increase in dendritic complexity as well as a 2-fold increase in dendritic length. The second growth spurt started at P14-15 and lasted until the end of the third postnatal week, where cells showed a remarkable increase in soma size and dendritic branching. Moreover, neurons that ranged from P20-35 were indistinguishable from adults. Perhaps the most notable difference is that in the rat soma size grew progressively with age, whereas in mouse, while somata were variable in size, they failed to show systematic increase with age. This is probably due to differences in the techniques

employed in the two studies, where in the rat the Golgi-Cox method was used to label neurons and assessment of cell body size were based on qualitative descriptions and not on quantitative measurements. Conversely, our results were obtained from 3-dimensional reconstruction of the soma and dendritic processes.

Our findings suggest that there is an orderly relationship between dendritic maturation and retinogeniculate remodeling. Perhaps, one of the first requirements is that some sort of semblance of dendritic architecture is needed so that synapses can begin to form in an orderly fashion. In fact, perhaps dendrites serve as a template for remodeling. In the mouse, the different stages of relay cell growth are concurrent with an active period of retinal innervation and remodeling. RGCs provide the driver input to relay cells, and retinal axons arising from the contralateral eye reach the dLGN embryonically, whereas those originating from the ipsilateral eye arrive perinatally (Godement et al., 1984; Jaubert-Miazza et al., 2005). Moreover, studies have shown that by birth retinogeniculate synapses are functional. For example, as early as P0-4, stimulation of RGCs axons elicit robust EPSPs in dLGN cells (Mooney, 1996). Moreover, at early ages, axons from both eyes are diffuse but refine to form completely segregated eye-specific domains (Jaubert-Miazza, 2005; Guido, 2008). The first growth spurt of relay cells which is marked by the establishment of cell class specification and dendritic complexity is coincident with the initial phase of course pruning of retinogeniculate terminals (Huberman, 2007; Jaubert-Miazza, 2005). Between P3-7, there is roughly 57% overlap between ipsilateral and contralateral axons. However, between P8-10, there is a substantial recession of ipsilateral terminals so that only 18% of terminal area in the dLGN is shared between the two eyes. Pruning continues and by P14 retinal terminals are completely segregated into eye-specific domains. During the period of axon segregation, changes in the patterns of retinogeniuclate

connectivity occur (Chen and Regehr, 2000; Jaubert-Miazza et al., 2005; see Huberman, 2007; see Guido, 2008). Prior to eye opening, geniculate cells are binocularly innervated, and receive as many as 10 separate inputs from RGCs. However, by P14-21 there is substantial pruning, synapse elimination, and the strengthening of the remaining inputs, so that cells receive just 1-3 inputs. This period of fine-scale functional refinement of retinogeniculate terminals occurs concurrently with the second phase of relay cells development which is indicated by an increase in dendritic field and length. This is also the period when non-retinal sources of input start to emerge including corticogeniculate input from layer IV of cortex, cholinergic input from brainstem and inhibitory input from NRT and intrinsic interneurons (Ballesteros et al., 2005; Jacobs et al., 2007; Bickford et al., 2010; Seabrook et al., 2010). Finally, pruning of retinogeniculate terminals is followed by a period of fine-scale maintenance which coincides with a stable and mature dendritic profile. Such observations are consistent with a recent study in the visual system of the *Xenopus* tadpole (Li et al., 2011). It was shown that immature retinotectal synapses were concentrated on dynamic dendritic branches, whereas mature synapses were found on stable dendrites.

The closely linked development time-points between the maturation of retinogeniculate synapses and relay cells growth indicate that perhaps these events are interrelated. The idea that afferent input plays a role in the development of their recipient targets has been widely explored in many systems and provides the basis of the synaptotrophic hypothesis (Vaughn, 1989; McAllister, 2000; Cline and Haas, 2008). Many studies demonstrated the mutual relationships between pre-and postsynaptic elements suggesting that similar scenarios could be present in the mouse dLGN as well. Different experimental approaches were previously undertaken to explore the role of retinal input in the development of relay cells. In these investigations, deafferentation

of retinal axons and activity blockade were used to eliminate retinal signaling (Brandes, 1971; Riccio et al., 1987; Sutton and Brunso-Bechtold, 1993; Dalva et al., 1994). However, these manipulations were done after RGCs have already innervated the nucleus, and thus failed to prevent early interactions between retinal axons and relay cells dendrites. Indeed, such nascent interactions could potentially have profound effects on dendritic morphology. For example, growing processes sample their surroundings, and periodically form adhesive junctions. This first step in largely mediated by adhesion molecules. A class of these molecules, N-cadherin, was found to play a role in synapse formation and dendritic tree stabilization in *Drosophila* olfactory system (Zhu and Luo, 2004). Olfactory receptor neurons (ORN) communicate with their postsynaptic partners known as the second order olfactory projection neurons (PN). In N-cadherin $^{-/-}$ ORN, the refinement of olfactory projections neurons PN does not persist and their arbors become diffuse and dispersed within many glomeruli, thereby disrupting spatial odor maps. In the mouse, cadherins have been recently implicated in RGC axonal targeting to different subcortical regions, but their role in synapse formation remains largely unexplored (Osterhoust et al., 2011).

Math5-null model

To eliminate retinal input to dLGN, we employed a genetic form of deafferentation from the time that RGCs are born and never leave the retina, by making use of *math5*-nulls. In these mutants, retinal progenitors fail to differentiate into RGCs, and thus exhibit more than 95% cell loss (Wang et al., 2001; Brown et al., 2001; Moshiri et al., 2008). More importantly, *math5* is found almost exclusively in the retina (Brown et al., 1998). While there have been some reports of *math5* expression in central structures such as VCN and cerebellum, we showed that dLGN is devoid of *math5* expression in perinatal and through adult ages (Fig. 2; Saul et., 2008).

Moreover, we confirmed that the few remaining RGCs fail to project and innervate central visual structures using a variety of techniques. Typically, axons can be readily visualized by intravitreal injections of the anterograde tracer CTB. In *math5*-nulls surviving RGCs were labeled but we failed to detect axonal labeling in SCN, dLGN or other retino-recipient targets (Fig. 3). Our results are consistent with others who show absence of anterograde labeling in retino-recipient structures (Wee et al., 2002; Brzezinski et al., 2005). Behavioral studies also confirm the lack of central projections, such as *math5*-nulls show no photic entrainment (Wee et al., 2002; Brzezinski et al., 2005). While this is limited to a subclass of RGCs and non-image forming structures, perhaps further tests that make use of visually evoked potentials would provide a more definite assay of image forming structures such as dLGN and visual cortex. Furthermore, we found the presence of very few puncta expressing VGluT2, which has been used as a presynaptic marker for retinal terminals in the dLGN. However, such level of expression is similar to what has been previously reported in binocularly enucleated rats, suggesting that VGluT2 expressing terminals are of non-retinal origin such as the superior colliculus or axon collaterals of relay cells (Fujiyama et al., 2003; Bickford et al., 2008). Finally, strong evidence supporting the absence of retinal terminals in the dLGN of *math5*-nulls was obtained from ultrastructural analysis at the electron microscopy level. In WT, terminals of retinal origin are the largest in the dLGN (Rafols and Valverde, 1973; Sherman, 2005; Bickford et al., 2010). In our limited sampling of electron microscopy sections we failed to detect any RLP profiles. However, we noted the presence of RLD terminals. These profiles were previously described in dLGN mice following enucleation, and in microphthamic and anophthalmic strains of mice (Cullen and Kaiserman-Abramof, 1976, Kaiserman-Abramof, 1983; Winkelmann et al., 1985). While these terminals do not arise from the retina, their origin

has been a great question of interest and still remains unresolved. One possibility is that they are the result of compensatory response arising from the cortex or brainstem (Kaiserman-Abramof, 1983). Thus, it is our belief that the utilization of the *math5*-nulls will be one the first ways to directly test the relationship between retinal signaling and relay cells development.

Development of relay cells in math5-nulls

Thus, we sought to assess the development of dLGN relay cells in the absence of retinal innervation using *math5*-nulls. These results are summarized in figure 21. Our morphological analysis revealed that the growth spurts dLGN relay cells are disrupted in *math5*-nulls. Overall, relay cells exhibit smaller somata and fluctuations in dendritic complexity and field extent. For example, during the second week when branch complexity is established in WT, *math5*-nulls continue to grow additional branches that reach up to the 11^{th} order. Such exuberant branching leads to a dramatic increase in dendritic surface area (Figs. 7, 9, 10, 21). However, by the third week, these additional higher order branches are lost (6^{th}-10^{th}) and complexity is comparable to age-matched WT. At the same time there is an expansion in dendritic field and length, so that during the third and fourth weeks, *math5*-nulls show comparable growth compared to WT (Figs. 7, 8, 9, 10, 21). Additionally, during the fifth postnatal week, relay cells exhibited a reduction in total surface area which is demonstrated by a reduction in their dendritic field, as well as loss of proximal dendritic branches (2^{nd}-4^{th} order segments) (Fig. 7, 8, 11, 21).

In sum, we identified the following aberrations in relay cells dendritic development in *math5*-nulls: (1) - During the second week, dendrites exhibit exuberant increase in the total number of dendritic branching. (2)- This branching is not maintained and the additional dendritic segments are lost during the third week. (3)- There is a continued decline in the number of

proximal dendrites as well as shrinkage and retraction of dendritic processes, leading to an overall reduction in dendritic surface area during the fifth week.

This scenario is at odds with other reports that either employed enucleation or TTX to assess role of retinal signaling in relay cells growth. While some have noted minimal changes in the growth patterns of relay cells, other studies showed no effect at all. Early postnatal bilateral enucleation in ferrets resulted in a delay in the elimination of spine-like appendages (Sutton and Brunso-Bechtold, 1993). There was also a report of a reduction in relay cell body size, which is consistent with our results. While in the cat, relay cells of the dLGN exhibited high spine density after blockade of voltage gated Na^+ channels with TTX (Dalva et al., 1994). In the rat, unilateral blockade of retinal activity through a long term treatment of TTX showed no change in relay cells morphology or branching patterns (Riccio et al., 1987). Similar results were obtained in the mouse where monocular enucleation at birth had no effect on the growth of relay cells. At P31, dendritic arborization in deafferented animals was indistinguishable from normal ones (Brandes, 1971). These discrepancies further underscore how enucleation and TTX fall short in this loss of function approach. Additionally, the rodent studies were done at one time point, and have failed to uncover the early phase of abundant dendritic branching and the late phase of atrophy that we observed during the second and fifth postnatal weeks, respectively.

It is important to note the extent to which our results conform to the synaptotrophic hypothesis. Our results suggest that retinal innervation might be necessary for constraining and stabilizing the dendritic complexity of relay cells, by providing them with a framework for other connections. Moreover, retinal signaling is required for the continued maintenance of relay cells dendritic form. These findings are in agreement with the synaptotrophic hypothesis (Vaughn, 1989; McAllister, 2000; Cline and Haas, 2008). One of the major tenants of this hypothesis is

that dendritic processes sample their environment and extend into regions where prospective synaptic afferents are found (Vaughn et al., 1974, 1988). The extensive dendritic branching that we observed in relay cells could be a compensatory response to the absence of retinal input. This branching could be an active process that dendrites engage in to seek synaptic partners. By increasing their dendritic surface area, these neurons would potentially augment the likelihood of finding synaptic partners. While exuberant branching was not apparent until the second postnatal week, a time that is well past the period when retinal axons normally invade and form synapses in dLGN (Godement et al., 1984; Mooney et al., 1996). Such compensation to the loss of presynaptic input has been observed in many studies (reviewed in McAllister, 2000). For example, dLGN neurons in neonatal ferrets were examined after blockade of NMDA receptors with APV antagonist (Rocha and Sur, 1995). This treatment resulted in an increase in dendritic branching, dendritic field expansion, and an increase in the number of spine-like appendages.

Another key element of the synaptotrophic hypothesis states that growing neuronal processes are stabilized after the establishment of synaptic junctions (Vaughn, 1989; McAllister, 2000; Cline and Haas, 2008). This idea is consistent with our findings since in the absence of retinal innervation, branching patterns of relay cells were not maintained. There was rapid and continued loss of dendritic segments, as well as retraction and reduction in dendritic field, resulting in relay cells that were significantly smaller than WT age-matched counterparts. These results suggest that RGCs provide trophic support that sustains the development of relay cells. Similar results were demonstrated in different brain structures following deafferentation including the cerebellum and VCN, the postsynaptic target of the auditory nerve fibers. For example, Purkenje cells of the cerebellum attain their mature morphological form concurrently with the establishment of synaptic contacts with parallel fibers (see Sotelo and Dusart, 2000).

Various experiments, such as genetic mutations or X irradiation, have shown that loss of parallel fibers leads to dystrophic effects on Purkenje cells dendritic arbors, as well as defects in their dendritic orientation. In another example, destruction of the cochlea hinders the growth and complexity of neurons in the VCN, such as cells had atrophied dendritic field, due to stunted growth of their branch tips (Trune, 1982). In another deafferentation example, the axo-dendritic interactions were analyzed in the vestibular system of amphibians (Ambystoma mexicanum; Kimmel et al., 1977). Mauthner cells (M-cell) developed without their vestibular supply, after the embryonic unilateral excision of the otic vesicle. This treatment was completed before the formation of dendrites and neuronal junctions, and it led to the complete loss of the vestibular ganglion and its fibers. As a result, M-cells' deprived dendritic regions developed simpler and thinner arbors, with very few branches.

Another result supporting a neurotrophic role of retinal innervation in the development of dLGN is apparent in examining the cytoarchitecture of the nucleus. Although the boundaries of dLGN are well defined and could be readily delineated from adjacent nuclei, there was roughly a 50% reduction in overall area compared to WT (Fig. 12). Moreover, reduced soma size was apparent throughout the studied ages (Fig. 7B). Taken together, these results suggest that retinal innervation might provide trophic support for the induction and maintenance of the overall structural integrity of the dLGN. Such trophic effect for retinal axons on the growth of relay cells has been previously described in anophthalmia and enucleation studies in mice, where increased cell death and smaller dLGN size have been reported (Cullen and Kaiserman-Abramof, 1976; Heumann and Rabinowicz; 1980). Moreover, studies in ferrets have revealed that postnatal monocular enucleation leads to a reduction in the overall size and distortion in the shape of the dLGN (Williams et al., 2002). Such role could be mediated by BDNF (Cohen-Corry and Lom,

2004). In the rat, it was shown that BDNF is employed by retinal afferents (Avwenagha et al., 2006). Other studies have also demonstrated that it is synthesized in the retina and can be transported anterogradely, and bind to their high affinity receptor tyrosine kinase (trkB) located on dLGN dendrites (Caleo et al., 2003; Menna et al., 2003; Avwenagha et al., 2006). Ablation of terminals in one eye, leads to a loss of BDNF immunoreactivity (Avwenagha et al., 2006). Moreover, both BDNF and trkB were associated with retinogeniculate terminals (Avwenagha et al., 2006).

There is some evidence that regional preferences of identified cell types were disrupted. In WT, Y- cells resided in a central band parallel to the optic tract, W- cells were located along the dorso-ventral borders of the nucleus, and X- cells were preferentially situated in the monocular segment of the dLGN (see Appendix I- Krahe and El-Danaf et al., 2011, submitted). In *math5* nulls, Y- and W- cells are found in relatively similar regions, while X- cells extended more medially and well beyond the monocular segment (Fig. 11B). Such positioning is very important for the assembly of parallel pathways. There is an emerging evidence suggesting that different classes of RGCs terminate in distinct lamina in dLGN that correspond with the location of the dendritic fields of identified relay cells (Hattar et al., 2006; Huberman et al., 2008; Kim et al., 2008; Badea et al., 2009; Huberman et al., 2009; Siegert et al., 2009; Ecker et al., 2010; Kim et al., 2010; Kay et al. 2011; Rivlin-Etzion et al., 2011). Thus, retinal signaling may be important for the formation of these distinct parallel channels.

Even though dendritic growth was disrupted in *math5*-nulls, it is important to note that a number of morphological and physiological features were maintained. For example, cell class specificity was largely unaffected. This further indicates that RGCs are not required for the early differentiation of these neurons. This is necessary to mention since cellular differentiation of

dLGN neurons starts at E10-13, and by E15 the nucleus is clearly visible with Nissl stain, at about the same time that RGCs axons are beginning to arrive (Angevine, 1970; Godement et al., 1984; see Guido, 2008). An assessment of the dendritic architecture of relay cells revealed that cell class specificity seems to be maintained in *math5* nulls (Fig. 11A). Relay cells fell into three categories that corresponded to the X-, Y- and W- cell types that we described in WT mouse (see Appendix I- Krahe and El-Danaf et al., 2011, submitted). An examination of relay cells functional characteristics shows that they possess all the active and passive membrane properties that have been described in WTs (Fig. 14,15; MacLeod et al., 1997; Jaubert-Miazza et al., 2005; Dilger et al., 2011). For example, cells are able to generate action potentials, show low-threshold calcium spike and burst responses, large "depolarizing sag" mediated by the hyperpolarization activated mixed cation (I_h) conductance, and the appearance of outward rectification mediated by depolarization activated K^+ conductance (I_A) that delays the firing of action potentials (Table, 1; Fig. 15). However, some subtle changes were noted such as high input resistance and lower τ (Fig. 16). These may simply reflect altered soma size and fluctuations of dendritic surface area. Taken together, this suggests that perhaps these characteristics of relay cells are mediated by other intrinsic or genetic cues that are unrelated to retinal input. For example, the idea that the general form of neurons is programmed by intrinsic cues was tested in isolated cultures of neurons (reviewed in McAllister, 2000). In these studies, the identification of specific types of neurons was possible, whereby the general dendritic characteristics were maintained. Moreover, in other systems, transcription factors were discovered to play a role in determining many features of the dendritic architecture, especially in the case of Purkenje cells in the cerebellum (Sotelo and Dusart, 2009). It is known that Purkenje cells dendritic arbors undergo several stages of remodeling before attaining their mature form. The activation of the transcription

factor retinoid-related orphan receptor alpha (RORα) is essential for the induction of the early developmental phases. Thus our results suggest that the structure-function relations are maintained and perhaps are mediated by such elements. However, the molecular basis of relay cells' development is largely unknown and remains to be explored.

In sum, the elements that seem immune to the loss of retinal input included general morphological form and function, such as cell class specification and intrinsic membrane properties. Furthermore, the time when dendritic branching and field expansion occur also seems to be maintained.

Potential role of non-retinal input

Even though RGCs provide the driver input to relay cells, retinogeniculate terminals only comprise about 10% of the total synapses in dLGN (Bickford et al., 2010). The overwhelming majority of input arises from non-retinal sources. These include glutamatergic input from layer IV of visual cortex, cholinergic input from brainstem, and inhibitory input from intrinsic interneurons and NRT. In many systems, there is evidence to suggest that such input could contribute to the dendritic form and function of relay cells.

Corticogeniculate innervation

Perhaps the largest input that relay cells receive arises from the feedback excitation of corticogeniculate afferents of layer VI of visual cortex (Bickford et al., 2010). These make up more than 50% of the total synaptic contacts in the mouse dLGN (Bickford et al., 2010). In contrast to retinogeniculate afferents, detailed information pertaining to the course of corticogeniculate innervation to dLGN was lacking, until recently. Seabrook et al. (2010)

addressed these issues by making use of the transgenic mouse model, *golli*-τ-GFP (Jacobs et al., 2007). The dLGN is the last thalamic nucleus to be innervated by cortical axons (Jacobs et al., 2007). Corticogeniculate projections arrive at the ventromedial border of the dLGN at P2, however they don't invade the nucleus until P4, and innervation is not complete until P10-P14 (Seabrook et al., 2010). Electrophysiological analysis showed that these make functional synapses with relay cells at P7, but synaptic maturation is not attained until the third postnatal week (Seabrook et al., 2010). Interestingly, this study revealed that layer VI cortical axons do not invade the dLGN until retinal axons from both eyes had innervated the nucleus. Moreover, corticogeniculate innervation is not complete until the segregation and refinement of retinal axons into eye specific domains is achieved (see Guido, 2008). This timing is coincident with the second phase of relay cells growth and suggests that corticogeniculate connections might play a role in the elongation and maintenance of relay cells dendritic processes. Additionally, a trophic role for corticogeniculate connections has been reported (Schoups et al., 1995). For example, in the rat, cortical infusion of the neurotrophic factors NT4-5 and NGF caused a dramatic increase in relay cells size. Furthermore, NT4-5 treatment was sufficient to speed up the growth of younger neurons, allowing them to mature at a faster pace.

While there is evidence of trophic support from cortex, it is not known if such role occurs independently of retinal innervation. Moreover, it is not known if corticogeniculate innervation to dLGN is disrupted. To test this, we crossed *golli*-τ-GFP transgenics with *math5*-nulls (Fig. 19, 20). In the absence of retinal innervation, cortical innervation to dLGN occurs, and target selection is maintained. However, the rate of innervation is highly accelerated and is complete by at least a week earlier than what occurs in WT. Moreover, not only innervation occurs but also functional synapses are formed between corticogeniculate axons and relay cells.

Ultrastructural analysis revealed the presence of RSD profiles, and our *in vitro* recordings revealed that synapses are functional and responses are indistinguishable from WT (Fig. 5, 20). These findings suggest that retinal innervation plays a role in dictating the timing of cortical innervation to the dLGN, acting as a brake, when present input is delayed until after refinement. However, when absent, so called brake is released and corticogeniculate innervation occurs more rapidly. How this is accomplished remains unanswered. Our results also suggest that cortical axons may contribute trophic support for sustaining relay cells growth, but a more specific role in regulating dendritic branching is unlikely. Since the accelerated rate of innervation did not necessarily lead to a concomitant shift in relay cells growth.

Cholinergic input

Another major source of excitatory input to dLGN arises from cholinergic afferents of the parabrachial region of the brainstem (Ballesteros et al., 2005). This input is necessary for modulating the relay of visual information to cortex by changing the firing patterns of relay cells between tonic and bursting modes.

Evidence supporting the role of cholinergic input in the maintenance and development of neuronal structures is found throughout the brain, and more specifically in the cortex (Sherren and Pappas, 2005). Basal forebrain nuclei provide most of the cholinergic innervation to cortex. This innervation starts at birth, and mature patterns of innervation are attained by P16. The implications of cholinergic deafferentation were studied in the visual cortex of the rat. Early postnatal loss of cholinergic neurons was achieved through the infusion of the selective immunotoxin 192 IgG-saporin. This resulted in a reduction in cortical thickness, as well as a reduction in cell body size of pyramidal neurons. These changes were also accompanied by a reduction in the number as well as spine density of apical dendrites.

In addition, cholinergic activity plays a major role in retinal development. During the first postnatal week, cholinergic starburst amacrine cells are responsible for the generation and propagation of stage II spontaneous retinal waves (Huberman et al., 2008). This activity is necessary for the refinement of retinogeniculate projections in the dLGN. Acetylcholine released from starburst amacrine cells exerts its function on RGCs through the pentameric nicotinic receptors (nAChR). These channels are made up for 12 different subunits, more specifically the β2 subunit was found to be implicated in the formation of waves (Bansal et al., 2000). Mice knockout for this subunit lack retinal waves during the first postnatal week. Moreover, RGCs exhibited a delay in the stratification and refinement of their dendrites. Another study in the developing chick retina demonstrated that increased levels of intracellular Ca^{2+} in RGC dendrites were mediated by nicotinic receptor transmission (Lohmann et al., 2002). This activity was necessary for stabilizing RGCs dendrites by preventing them from retracting.

In the dLGN of the mouse, there is an increase in the density of cholinergic acetyl transferase (ChAT) positive fibers with age, starting at P5 and through P12 (Ballesteros et al., 2005). At this time, cholinergic axons were found to form clusters marking the first evidence of synapse formation. Cholinergic terminals are found within triadic synaptic arrangements and along dendritic shaft of relay cells (Erisir et al., 1997; Bickford et al., 2010). As in the case of corticogeniculate terminals, cholinergic innervation to dLGN occurs after retinal fibers had innervated the nucleus. Moreover, the location of these inputs on proximal dendrites and their proximity to retinal input suggests that cholinergic innervation might influence the maturation of dendritic arbors of relay cells. However, the first cholinergic synapses occur after the completion of the two growth phases noted for relay cells. This could suggest that this input is not needed for the induction but could play a role in stabilization and maintenance of dendritic

processes, since the presence of cholinergic synapses coincide with the period when we noted a dystrophic loss of dendritic branching and corresponding retraction in dendritic field and surface area. In *math5*-nulls, there is evidence that this form of input is present in the dLGN through the presence of RSD profiles at the electron microscopy level. However, we were not able to distinguish whether these are of cortical or brainstem origin, and more analysis is required to confirm this (Fig. 5).

Inhibition

Another form of connectivity in the dLGN arises from interneurons intrinsic to dLGN and neurons of the NRT (Bickford et al., 2010). Both use γ-aminobutyric acid (GABA) as a neurotransmitter, and such input are necessary for sharpening retinal signals by influencing the gain of retinogeniculate transmission and help shaping the on/off antagonist center surround receptive field organization. Inhibitory connections make up around 18% of total synapses in dLGN (Bickford et al., 2010). Mature GABAergic profiles are apparent at P14 and make synapses with dendrites of relay cells, comprising triadic arrangements. Functionally, optic tract stimulation elicits inhibitory postsynaptic potentials in relay cells. This form of connectivity is first apparent at P9 but does not reach full maturity until the end of the second postnatal week. This period coincides with the second growth phase of relay cells, suggesting a potential role of GABAergic elements in induction and maintenance of relay cells dendritic elongation.

Many studies have shown that GABA plays different roles in dendritic development and maintenance (reviewed in Belhage et al., 1998). For example, prolonged extracellular infusion of GABA in the superior cervical ganglion of the rat had a profound effect on dendritic architecture of ganglion neurons. This was manifested by an increase in the number of processes

as well as an increase in the number of postsynaptic membrane thickenings, which precede the establishment of synaptic contacts. It was also shown that GABA is essential for neurite outgrowth and complexity in several brain regions, such as hippocampus, cerebellum and cortex. For example, neurite elongation was enhanced in cultures of cerebellar granular cells in the presence of GABA. Moreover, blockade of GABA receptors in hippocampus or depletion of GABA in cortex prevent neurite outgrowth.

In different regions of the immature brain, such as hippocampus and hypothalamus, there is evidence that GABA activity elicits depolarization in postsynaptic neurons before switching to hyperpolarization (reviewed in Belhage et al., 1998). It was also shown that GABA receptor-mediated depolarization indirectly activates voltage-gated calcium channels that in turn increase intracellular levels of calcium, leading to the activation of many second messenger cascades that induce transcription of several genes involved in neural differentiation, synaptogenesis and development. Interestingly, cellular differentiation of dLGN neurons starts at E10-13, and relay cells could be easily identified from interneurons after 12 hours of birth (Angevine, 1970; Parnavelas et al., 1977). Moreover, GABA could be detected in the dLGN of the mouse way before inhibitory synapses are formed (Arcelli et al., 1997; Bickford et al., 2010). These events precede the growth spurts of relay cells, and might suggest that GABA plays a role in relay cells differentiation, functional characteristics, survival as well as dendritic branching and field extent. Although GABA may play a role in relay cell development, it remains to be seen whether inhibitory elements are affected by the elimination of retinal innervation.

Conclusions

This is the first in depth study of relay cells development in the dLGN of the mouse. Moreover, it is also one the first investigations of the mechanisms that influence the maturation of these neurons. We found that retinal innervation plays an important trophic role in the maturation of dLGN and is necessary for the continued maintenance of relay cells structural integrity. While non-retinal sources of input may play a contributing role in relay cells growth, they are not sufficient by themselves to regulate cell maturation.

Many factors could be implicated in the development of relay cells. With the availability of multiple tools, we would be able to dissect all the contributing elements and understand how they work in concert to develop a functional circuitry. For example, the role of cholinergic activity in the development of dLGN neurons could be studied with the use of the transgenic mouse model (Chat-cre). In this mouse, the choline acetyltransferase drives the expression of cre recombinase. By crossing these mice with other reporter mouse lines, these projections can be visualized and traced. In fact, these mice are currently employed in our lab to study the patterns of cholinergic innervation to dLGN. Moreover, we can study how these inputs are affected by the loss of retinal innervation by crossing them to *math5*-nulls. Similar experimental approaches could be used to study the effects of inhibition on development, as well as the role of retinal innervation in the connectivity patterns using the GAD67 and GAD65 transgenic mouse models (Tamamaki et al., 2003; López-Bendito et al., 2004). In these mice, GFP-expressing neurons could be easily targeted for electrophysiological as well as morphological studies. Lastly, further experiments should be performed in the *math5-null*/*golli*-τ- GFP crosses to gain a better understanding of the corticogeniculate connectivity in dLGN of *math5*-nulls.

We mapped the developmental time course of relay cells in the dLGN; however the molecular mechanisms underlying these events remain unknown. Using techniques such as microarray analysis, we can start identifying genes that could be implicated in relay cells maturation, as well as dendritic branching, elongation and stabilization. Knowing the time points of relay cells growth spurts, we can search for genes that could be up/ or down-regulated during these developmental periods, and perhaps compare the expression patterns to ones seen in *math5*-nulls.

Lastly it is important to consider these results in a clinical context, especially in situations where RGCs are degenerating or completely lacking. In *math5*-nulls, the overall form and function of relay cells seem relatively preserved, and it appears that they are able to receive and convey signals. Therapeutic measures that would be taken to restore vision either through prosthetics or stem cells research should be done in accordance with the developmental changes that we noted. For example, during weeks 1, 3-4, the dendritic architecture of relay cells is similar between *math5*-nulls and WTs. Moreover, more measures need to be taken such as trophic support to insure proper growth and development of relay cells and dLGN.

Figure 21

Development of relay cells in WT and *math5*-nulls.

Schematic summarizing the development of relay cells in WT (top row) and *math5*-nulls (bottom row). In WT, relay cells undergo two growth spurts. The first one occurs during the first postnatal week, where cell class specification and complexity are established. Relay cells can be classified in three groups based on their morphological profiles: Y-radial, W-hemispheric, and X-biconical. The second growth spurt starts during the second week and continues through the third week, where there is an extensive increase in dendritic length and field extent. Following the third week, the overall growth of relay cells is stabilized. Moreover, corticogeniculate innervation is not complete until the end of the second postnatal week. Corticogeniculate patterns of innervation are illustrated in green. In the absence of retinal innervation, relay cells maintain their general form and function. However, dLGN is highly reduced in size, and relay cells exhibit disrupted growth spurts having smaller somata and fluctuations in dendritic complexity and field extent. An exuberant dendritic branching is noted in week 2. These additional branches are lost during week 3. Finally, by week 5, an overall reduction in relay cells surface area is observed in *math5*-nulls which results from a continued loss of dendritic segments, as well as shrinkage and retraction of dendritic processes. Moreover, corticogeniculate innervation is highly accelerated and is complete a week earlier than WT. These results are further illustrated in the scatter plots examining the different aspects of relay cells growth: (Top: dendritic surface area; bottom, left panel: dendritic branching; bottom right panel: dendritic field). The increased dendritic surface area seen in *math5*-nulls during the second postnatal week can be explained by exuberance in dendritic branching (blue dotted area). Whereas, the reduction in dendritic surface area observed in the fifth postnatal week is due to a

retraction in dendritic field as well as a continued loss of dendritic branches (Orange dotted area). Images are drawn to scale (scale bar= 100 μm).

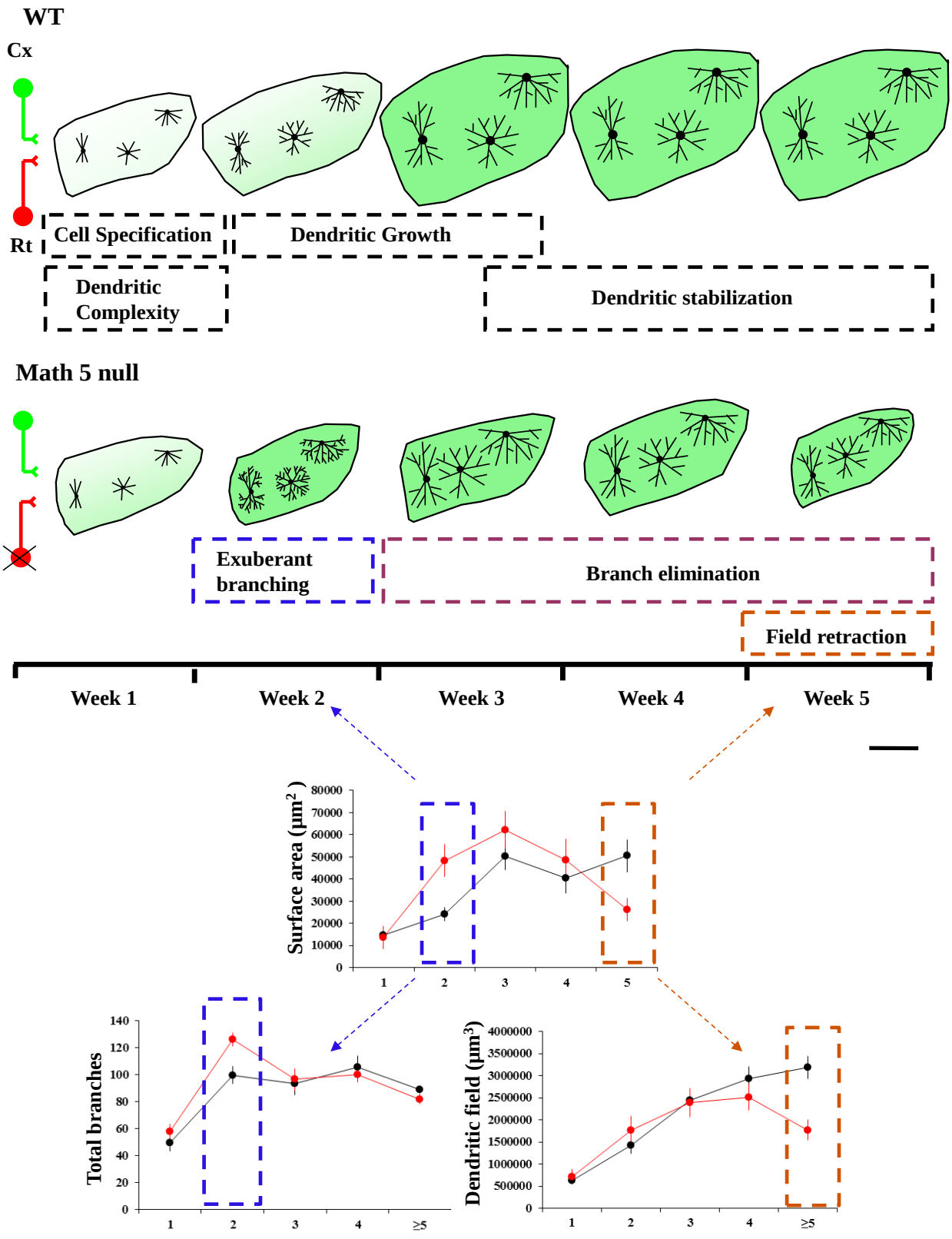

Literature Cited

Angevine, J. B. (1970) Time of neuron origin in the diencephalon of the mouse. An autoradiographic study. *J Comp Neurol.* 139, 129-188.

Arcelli, P., Frassoni, C., Regondi, M.C., De Biasi, S., and Spreafico, R. (1997). GABAergic neurons in mammalian thalamus: a marker of thalamic complexity? *Brain Res Bull,* 42(1):27-37.

Avwenagha, O., Bird, M.M., Lieberman, A.R., Yan, Q., and Campbell, G. (2006). Patterns of expression of brain-derived neurotrophic factor and tyrosine kinase B mRNAs and distribution and ultrastructural localization of their proteins in the visual pathway of the adult rat. *Neuroscience, 140*: 913-28.

Badea., T.C., Cahill, H., Ecker, J., Hattar, S., and Nathans, J. (2009). Distinct roles of transcription factors brn3a and brn3b in controlling the development, morphology, and function of retinal ganglion cells. *Neuron,* 61:852-864

Ballestero, J.M., Van Der List, D.A., and Chalupa, L.M. (2005). Formation of eye-specific retinogeniculate projections occurs prior to the innervation of the dorsal lateral geniculate nucleus by cholinergic fibers. *Thalamus Relat Syst*, 3(2):157-163.

Bansal, A., Singer, J.H., Hwang, B.J., Xu, W., Beaudet, A., and Feller, M.B. (2000). Mice lacking specific nicotinic acetylcholine receptor subunits exhibit dramatically altered spontaneous activity patterns and reveal a limited role for retinal waves in forming ON and OFF circuits in the inner retina. *J Neurosci.* 20(20):7672-81.

Belhage B, Hansen GH, Elster L, Schousboe A. (1998). Effects of gamma-aminobutyric acid (GABA) on synaptogenesis and synaptic function. *Perspect Dev Neurobiol,* 5(2-3):235-46.

Bickford, M.E, Slusarczyk, A, Dilger, E.K, Krahe, T.E, Kucuk, .C, Guido W. (2010). Synaptic development of the mouse dorsal lateral geniculate nucleus. *J Comp Neurol*, 518(5):622-35.

Bickford, M.E, Wei, H., Eisenback, M.A., Chomsung, R.D., Slusarczyk, A.S, and Dankowsi, A.B. (2008). Synaptic Organization of Thalamocortical Axon Collaterals in the Perigeniculate Nucleus and Dorsal Lateral Geniculate Nucleus. *J Comp Neurol*, 508:264–285.

Blashfield RK, Aldenderfer MS (1984) Cluster Analysis, Newbury Park CA: Sage.

Brandes, J.S. (1971). Dendritic branching patterns in lateral geniculate nucleus following deafferentation. *Exp Neurol.* 31(3):444-50.

Brown, N.L., Kanekar, S., Vetter, M.L., Tucker, P.K., and Gemza, D.L. (1998). Math5 encodes a murice basic helix-loop-helix transcription factor expressed during early stages of retinal neurogenesis. *Development*, 125: 4821-4833.

Brown, N. L., Pate, S., Brzezinsk, J., and Glaser, T. (2001). Math5 is required for retinal ganglion cell and optic nerve formation. *Development*, 126: 2497-2508.

Brzezinski, J.A, Brown, N.L, Tanikawa, A, Bush, R.A, Sieving, P.A, Vitaterna, M.H, Takahashi, J.S, and Glaser, T. (2005). Loss of Circadian Photoentrainment and abnormal retinal electrophysiology in Math5 mutant mice. *Investigative Ophthalmology & Visual Science*, 46 (7): 2540-51.

Caleo, M., Medini, P., von Bartheld, C.S., and Maffei, L. (2003).Provision of brain-derived neurotrophic factor via anterograde transport from the eye preserves the physiological responses of axotomized geniculate neurons. *J Neurosci.* 23(1):287-96.

Caviness, V.S., and Frost, D.O. (1980). Tangential organization of thalamic projections to the neocortex in the mouse. *J Comp Neurol*,194:335-367.

Chase, H.B., and Chase, E.B. (1941). Studies on an anophthalmic strain of mice. I . Embryology of the eye region. *J Morph*, 68: 279-301.

Chen, C., and Regehr, W.G. (2000). Developmental remodeling of the retinogeniculate synapse. *Neuron, 28*(3): 955-66.

Chen, F., El-Dawlatly, S., Jin, R., and Oweiss. (2007). Indentifying and tracking the number of independent clusters of functionally interdependent neurons from biophysical models of population activity. Conf Proc IEEE EMBS on Neural Eng 542-545.

Cline, H., and Haas, K. (2008). The regulation of dendritic arbor development and plasticity by glutamatergic synaptic input: a review of the synaptotropic hypothesis. *J Physiol, 586*: 1509-17.

Cohen-Cory, S., and Lom, B. (2004). Neurotrophic regulation of retinal ganglion cell synaptic connectivity: from axons and dendrites to synapses. *Int J Dev Biol.* 48(8-9):947-56.

Coleman. J.E., Law, K., and Bear, M.F. (2009). Anatomical origins of ocular dominance in mouse primary visual cortex. *Neuroscience*, 161:561-571.

Crunelli, V., Leresche, N., and Parnavelas, J.G. (1987). Membrane properties of morphologically identified X and Y cells in the lateral geniculate nucleus of the cat in vitro. *J Physiol*, 390:243-56.

Crunelli, V., Lightowler, S., and Pollard, C.E. (1989). A T-type Ca^{2+} current underlies low-threshold Ca^{2+} potentials in cells of the cat and rat lateral geniculate nucleus. *J Physiol*, 413:543-61.

Cullen, M.J., and Kaiserman-Abramof, I.R. (1976). Cytological organization of the dorsal lateral geniculate nuclei in mutant anophthalmic and postnatally enucleated mice. *J Neurocytol*, 5 (4): 407-424.

Dalva, M.B., Ghosh, A., and Shatz, C.J. (1994). Independent control of dendritic and axonal form in the developing lateral geniculate nucleus. *J Neurosci*, 6:3588-602.

Dilger EK, Shin HS, and Guido, W. (2011). Requirements for synaptically evoked plateau potentials in relay cells of the dorsal lateral geniculate nucleus of the mouse. *J Physiol*., 589 (4): 919-37.

Demeulemeester, H., Arckens, L., Vandesande, F., Orban, G.A., Heizmann, C.W., and Pochet, R. (1991). Calcium binding proteins as molecular markers for cat geniculate neurons. *Exp Brain Res*, 83:513-20.

Derrington, A.M., and Lennie, P. (1984). Spatial and temporal contrast sensitivities of neurones in lateral geniculate nucleus of macaque. *J Physiol*, 357:219-240.

Ecker, J.L., Dumitrescu, O.N., Wong, K.Y., Alam, N.M., Chen, S.K., LeGates, T., Renna, J.M., Prusky, G.T., Berson, D.M., and Hattar, S. (2010). Melanopsin-expressing retinal ganglion-cell photoreceptors: Cellular diversity and role in pattern vision. *Neuron*, 67:49-6.

Eldanaf, R.N., Krahe, T.E., Dilger, E.K., Seabrook, T.A., and Guido, W.. Morphologically distinct classes of relay neurons reside in different regions of the mouse dorsal lateral geniculate nucleus (dLGN). Society for Neuroscience abstract, Chicago IL, 2009.

Erişir, A., Van Horn, S.C., Bickford, M.E., and Sherman, S.M. (1997). Immunocytochemistry and distribution of parabrachial terminals in the lateral geniculate nucleus of the cat: a comparison with corticogeniculate terminals. *J Comp Neurol,* 377(4):535-49.

Fiala, J. C., Spacek, J., and Harris, K.M. (2008). Dendrite structure. In G. Stuart, N. Spruston, and M. Häusser (Eds.), *Dendrites* (2nd ed., pp. 1-41). New York: Oxford University Press.

Fox, M.A. (2008). Novel roles for collagens in wiring the vertebrate nervous system. *Curr Opin Cell Biol*, 20(5):508-13.

Fox, M.A., and Umemori, H. (2006). Seeking long-term relationship: axon and target communicate to organize synaptic differentiation. *J Neurochem*, 97(5):1215-31.

Friedlander, M.J., Lin, C.S., Stanford, L.R, and Sherman, S.M. (1981). Morphology of functionally identified neurons in lateral geniculate nucleus of the cat. *J Neurophysiol*, 46:80-129.

Fujiyama, F., Hioki, H., Tomioka, R., Taki, K., Tamamaki, N., Nomura, S., Okamoto, K., and Kaneko, T. (2003). Changes of immunocytochemical localization of vesicular glutamate

transporters in the rat visual system after the retinofugal denervation. *J Comp Neurobiol,* 465: 234-249.

Gao, E., DeAngelis, G.C., and Burkhalter, A. (2010). Parallel input channels to mouse primary visual cortex. *J Neurosci,* 30:5912-5926.

Glitsch, M.D. (2008). Spontaneous neurotransmitter release and Ca^{2+} how spontaneous is spontaneous neurotransmitter release? *Cell Calcium,* 43(1):9-15.

Gong, S., Doughty, M., Harbaugh, C.R., Cummins, A., Hatten, M.E., Heintz, N., and Gerfen, C.R. (2007). Targeting Cre Recombinase to specific neuron populations with bacterial artificial chromosome constructs. *J Neurosci,* 27:9817-9823.

Godement, P., Salaün, J. and Imbert, M. (1984). Prenatal and postnatal development of retinogeniculate and retinocollicular projections in the mouse. *J Comp Neurol, 230*(4): 552-75.

Grubb, M.S., and Thompson, I.D. (2005). Visual response properties of burst and tonic firing in the mouse dorsal lateral geniculate nucleus. *J Neurophysiol,* 93:3224-47.

Grubb, M.S., and Thompson, I.D. (2004). Biochemical and anatomical subdivision of the dorsal lateral geniculate nucleus in normal mice and in mice lacking the beta2 subunit of the nicotinic acetylcholine receptor. *Vision Res,* 44:3365-76.

Grubb, M.S., and Thompson, I.D. (2003). Quantitative characterization of visual response properties in the mouse dorsal lateral geniculate nucleus. *J Neurophysiol,* 90:3594-607.

Guido, W. (2008). Development of retinogeniculate pathway. In L.M. Chalupa, and R.W. Williams (Eds.), *Eye, retina, and visual system of the mouse* (1st edition, p.p. 415-427). London; Cambridge: Massachusetts Institute of Technology.

Guillery, R.W., Ombrellaro, M., and LaMantia, A.L. (1985). The organization of the lateral geniculate nucleus and of the geniculocortical pathway that develops without retinal afferents. *Brain Res*. 352(2):221-33.

Hartigan, J.A., and Wong, M.A. (1979). Algorithm AS: A K-means clustering algorithm. *J Roy Stat Soc,* 28:100-108.

Harting, J.K., Huerta, M.F., Hashikawa, T., and van Lieshout, D.P. (1991). Projection of the mammalian superior colliculus upon the dorsal lateral geniculate nucleus: organization of tectogeniculate pathways in nineteen species. *J Comp Neurol,* 304:275-306.

Hattar, S., Kumar, M., Park, A., Tong, P., Tung, J., Yau, K.W,, and Berson, D.M. (2006). Central projections of melanopsin-expressing retinal ganglion cells in the mouse. *J Comp Neurol,* 497:326-349

Heumann, D., and Rabinowicz, Th. (1980). Postnatal development of the dorsal lateral geniculate nucleus in the normal and enucleated albino mouse. *Exp Brain Res*, 38: 75-85.

Hong, Y.K., Kim, I.J., and Sanes, J.R. (2011). Stereotyped axonal arbors of retinal ganglion cell subsets in the mouse superior colliculus. *J Comp Neurol*, 519:1691-711.

Huberman, A.D. (2007). Mechanisms of eye-specific visual circuit development. *Curr Opin Neurobiol, 17*(1): 73-80.

Huberman, A.D., Wei, W., Elstrott, J., Stafford, B.K., Feller, M.B., and Barres, B.A. (2009). Genetic identification of an on-off direction-selective retinal ganglion cell subtype reveals a layerspecific subcortical map of posterior motion. *Neuron*, 62:327-334

Huberman, A.D., Manu, M., Koch, S.M., Susman, M.W., Lutz, A.B., Ullian, E.M., Baccus, S.A., and Barres, B,A, (2008). Architecture and activity-mediated refinement of axonal projections from a mosaic of genetically identified retinal ganglion cells. *Neuron*, 59:425-438.

Huberman, A.D., Feller, M.B., Chapman, B. (2008). Mechanisms underlying development of visual maps and receptive fields. *Annu Rev Neurosci*. 31:479-509

Jacobs, E.C., Campagnoni, C., Kampf, K., Reyes, S.D., Kalra, V., Handley, V., Xie, Y., Hong-Hu, Y., Spreur, V., Fisher, R.S., and Campagnoni, A.T. (2007). Visualization of corticofugal projections during early cortical development in a τ-GFP-transgenic mouse. *Eur J Neurosci*, 25(1): 17-30.

Jain, A.K., Murty, M.N., and Flynn, P.J. (1999). Data clustering: a review. *ACM Computing Surveys*, 31:264-323.

Jaubert-Miazza, L., Green, E., Lo, F. S., Bui, K., Mills, J., and Guido, W. (2005). Structural and functional composition of the developing retinogeniculate pathway in the mouse. *Vis Neurosci*, 22(5): 661-76.

Kaiserman-Abramof, I. R. (1983). Intrauterine enucleation of normal mice mimics a structural compensatory response in the geniculate of eyeless mutant mice. *Brain Research*, 270: 149-153.

Kay, J.N., De la Huerta, I., Kim, I.J., Zhang, Y., Yamagata, M., Chu, M.W., Meister, M., snf Sanes, J.R. (2011). Retinal ganglion cells with distinct directional preferences differ in molecular identity, structure, and central projections. *J Neurosci*, 31:7753-62

Kim, I.J., Zhang, Y., Meister, M., and Sanes, J.R. (2010). Laminar restriction of retinal ganglion cell dendrites and axons: Subtype-specific developmental patterns revealed with transgenic markers. *J Neurosci*, 30:1452-1462.

Kim, I.J., Zhang, Y., Yamagata, M., Meister, M., and Sanes, J.R. (2008). Molecular identification of a retinal cell type that responds to upward motion. *Nature*, 452:478-482.

Kimmel, C.B., Schabtach, E., and Kimmel, R.J. (1977). Developmental interactions in the growth and branching of the lateral dendrite of mauthner's cell (Ambystoma mexicanum). *Developmental Bio., 55*: 244-59.

Krahe, T.E., and Guido, W. (2011). Homeostatic plasticity in the visual thalamus by monocular deprivation. *J Neurosci*, 31(18): 6842– 6849,

Krahe, T.E., Eldanaf, R.N., Dilger, E.K., Henderson, S.C., and Guido, W. (2011). Morphologically distinct classes of relay cells exhibit regional preferences in the dorsal lateral geniculate nucleus of the mouse. Submitted to *J Neurosci*, in review.

Land, P.W, Kyonka, E, and Shamalla-Hannah, L. (2004). Vesicular glutamate transporters in the lateral geniculate nucleus: expression of VGLUT2 by retinal terminals. *Brain Research*, 996: 251– 254.

Lennie, P. (1980). Parallel visual pathways: A review. *Vision Res*, 20:561-594.

Li, J., Erisir, A., and Cline, H. (2011). In vivo time-lapse imaging and serial section electron microscopy reveal developmental synaptic rearrangements. *Neuron*, 69(2):273-86.

Lohmann, C., Myhr, K.L., and Wong. R.O. (2002). Transmitter-evoked local calcium release stabilizes developing dendrites. *Nature,* 418(6894):177-81.

López-Bendito, G., Sturgess, K., Erdélyi, F., Szabó, G., Molnár, Z,, (2004). Preferential origin and layer destination of GAD65-GFP cortical interneurons. *Cerebral Cortex*, 14: 1122–1133.

Martin, P.R. (1986). The projection of different retinal ganglion cell classes to the dorsal lateral geniculate nucleus in the hooded rat. *Exp Brain Res*, 62:77-88.

Masland, R.H. (2001). The fundamental plan of the retina. *Nat Neurosci*, 9:877-86.

McAllister, AK. (2000). Cellular and molecular mechanisms of dendrite growth. *Cereb Cortex,* 10(10):963-73.

MacLeod ,N., Turner, C., Edgar, J. (1997). Properties of developing lateral geniculate neurones in the mouse. *Int J Dev Neurosci*, 15(2):205-24.

Menna, E., Cenni, M.C., Naska, S., and Maffei, L. (2003). The anterogradely transported BDNF promotes retinal axon remodeling during eye specific segregation within the LGN. *Mol Cell Neurosci,* 24(4):972-83.

Mooney, R., Penn, A.A., Gallego, R., and Shatz, C.J. (1996). Thalamic relay of spontaneous retinal activity prior to vision. *Neuron. 17*(1): 979-90.

Moshiri, A., Gonzalez, E., Tagawa, K., Maeda, H., Wang, M., Frishman, L.J., and Wang, S.W. (2008). Near complete loss of retinal ganglion cells in the math5/brn3b double knockout elicits severe reductions of other cell types during retinal development. *Developmental Biol*, 316: 214-27.

Nassi, J.J., and Callaway, E.M. (2009). Parallel processing strategies of the primate visual system. *Nat Rev Neurosci,* 10:360-372.

Osterhout, J.A., Josten, N., Yamada, J., Pan, F., Wu, S.W,, Nguyen, P.L., Panagiotakos, G., Inoue, Y.U., Egusa, S.F., Volgyi, B., Inoue, T., Bloomfield, S.A., Barres, B.A., Berson, D.M., Feldheim, D.A., and Huberman, A.D. (2011). Cadherin-6 Mediates Axon-Target Matching in a Non-Image-Forming Visual Circuit. *Neuron,* 71(4):632-639.

Palizvan, M.R., Sohya, K., Kohara. K., Maruyama, A., Yasuda, H., Kimura, F., and Tsumoto, T. (2004). Brain-derived neurotrophic factor increases inhibitory synapses, revealed in solitary neurons cultured from rat visual cortex. *J Neurosci.* 126(4):955-66.

Parnavelas, J.G., Mounty, E.J., Bradford, R., and Lieberman, A.R. (1977). The postnatal development of neurons in the dorsal lateral geniculate nucleus of the rat: a Golgi study. *J Comp Neurol*, 171(4): 481-99.

Rafols, J.A., and Valverde F. (1973) The structure of the dorsal lateral geniculate nucleus in the mouse: a Golgi and electron microscopy study. *J Comp Neurol*, *150*(3): 303-32.

Rajan, I., and Cline, H.T. (1998). Glutamte receptor activity is required for normal development of tectal cell dendrites in vivo. *J. Neurosci*, *18*(19): 7836-7846.

Reese, B.E. (1988). 'Hidden lamination' in the dorsal lateral geniculate nucleus: the functional organization of this thalamic region in the rat. *Brain Res*, 119-37.

Reese, B.E. (1984). The projection from the superior colliculus to the dorsal lateral geniculate nucleus in the rat. *Brain Res*, 305:162-168.

Riccio, R.V., Matthews, M.A. (1987). Effects of intraocular tetrodotoxin on the postnatal development of the dorsal lateral geniculate nucleus of the rat: a Golgi analysis. *J Neurosci Res,* 17(4):440-51.

Rivlin-Etzion, M., Zhou, K., Wei, W., Elstrott, J., Nguyen, P.L., Barres, B.A., Huberman, A.D., and Feller, M.,B. (2011). Transgenic mice reveal unexpected diversity of on-off direction selective retinal ganglion cell subtypes and brain structures involved in motion processing. *J Neurosci*. 31:8760-9.

Rocha, M., and Sur, M. (1995). Rapid acquisition of dendritic spines by visual thalamic neurons after blockade of N-methyl-d-aspartate receptors. *Proc. Natl. Acad. Sci*., 92: 8026-30.

Rotolo, T., Smallwood, P.M., Williams, J., and Nathans, J. (2008). Genetically-directed, cell type-specific sparse labeling for the analysis of neuronal morphology. *PLoS One* 3:e4099.

Sanes DH, Friauf E.(2000). Development and influence of inhibition in the lateral superior olivary nucleus. *Hear Res.*147(1-2):46-58.

Saul, S.M, Brzezinski, J.A 4th, Altschuler. R.A, Shore, S.E, Rudolph, D.D, Kabara, L.L, Halsey, K.E, Hufnagel, R.B, Zhou, J, Dolan, D.F, and Glaser T. (2008). Math5 expression and function in the central auditory system. *Mol Cell Neurosci*, 37(1):153-69.

Schoups, A.A., Elliot, R.C., Friedman, W.J., and Black, L.B. (1995). NGF and BDNF are differentially modulated by visual experience in the developing geniculocortical pathway. *Dev Brain Res*, 86: 326-34.

Seabrook, T.A., Eldanaf, R.N,, Krahe, T.E., Fox, M.A., and Guido, W. (2010), Timing of corticogeniculate innervation in the dorsal lateral geniculate nucleus (dLGN) of the mouse relies on retinogeniculate axon innervation. Society for Neuroscience abstract, San Diego CA.

Shatz, C.J. (1983). The prenatal development of the cat's retinogeniculate pathway. *J Neurosci*, 3:482-99.

Sherren, N., and Pappas, B.A. (2005). Selective acetylcholine and dopamine lesions in neonatal rats produce distinct patterns of cortical dendritic atrophy in adulthood. *J Neurosci*. 136(2):445-56.

Sherman, S.M. (2005). Thalamic relays and cortical functioning. Prog. Brain Res. 149: 107-26
Sutton, J.K, and Brunso-Bechtold, .JK. (1993). Dendritic development in the dorsal lateral geniculate nucleus of ferrets in the postnatal absence of retinal input: a Golgi study. *J Neurobiol.* (3):317-34.

Sherman, S.M. (1985). Functional organization of the W-, X-, and Y-cell pathways: a review and hypothesis. In: Progress in Psychobiology and Physiological Psychology, JM Sprague and AN Epstein (eds), Academic Press, New York, 233-314.

Sherman, S.M., and Koch, C. (1986). The control of retinogeniculate transmission in the mammalian lateral geniculate nucleus. *Exp Brain Res*, 63:1-20.

Sherman, S.M., and Spear, P.D. (1982). Organization of visual pathways in normal and visually deprived cats. *Physiol Rev*, 62:738-855.

Siegert, S., Scherf, B.G., Del Punta, K., Didkovsky, N,, Heintz, N., and Roska, B. (2009). Genetic address book for retinal cell types. *Nat Neurosci* 12:1197-1204.

Soltesz, I., Lightowler, S., Leresche, N., and Crunelli, V. (1989). On the properties and origin of the GABAB inhibitory postsynaptic potential recorded in morphologically identified projection cells of the cat dorsal lateral geniculate nucleus. J *Neurosci*, 33:23-33.

Sotelo, C., and Dusart, I. (2009). Intrinsic versus extrinsic determinants during the development of Purkenje cell dendrites. *Neuroscience*, doi:10.1016/j.neuroscience.2008.12.035.

Stanford, L.R., Friedlander, M.J., and Sherman, S.M. (1983). Morphological and physiological properties of geniculate W-cells of the cat: A comparison with X- and Y-cells. *J Neurophysiol*, 50:582-608.

Stanford, L.R., Friedlander, M.J., and Sherman, S.M. (1981). Morphology of physiologically identified W-cells in the C laminae of the cat's lateral geniculate nucleus. *J Neurosci*, 1:578-584.

Stone, J. (1983).. Parallel Processing in the Visual System. New York: Plenum.

Su, J., Haner, C.V., Imbery, T.E., Brooks, J.M., Morhardt, D.R., Gorse, K., Guido, W., and Fox, M.A. (2011). Reelin Is Required for Class-Specific Retinogeniculate Targeting. *J Neurosci*. 31(2):575–586.

Tamamaki, N., Yanagawa, Y., Tomioka, R., Miyazaki, J., Obata, K., and Kaneko, T. (2003), Green fluorescent protein expression and colocalization with calretinin, parvalbumin, and somatostatin in the GAD67-GFP knock-in mouse. *J Comp Neurol*, 467:60–79

Trune, D.R. (1982). Influence of neonatal cochlear removal on the development of mouse cochlear nucleus: II. Dendritic morphometry of its neurons. *J Comp Neurol, 209*: 425-34.

Tucker, P., Laemle, L., Munson, A., Kanekar, S., Oliver, E.R., Brown, N., Schlecht, H., Vetter, M., and Glaser, T. (2001). The eyeless mouse mutation (ey1) removes an alternative start codon from the Rx/rax homeobox gene. *Genesis.* 31(1):43-53.

Turner, J.P., and Salt, T,E, (1998). Characterization of sensory and corticothalamic excitatory inputs to rat thalamocortical neurones in vitro. *J Physiol*, 510:829–843.

Usrey, W.M., and Reid, R.C. (2000). Visual physiology of the lateral geniculate nucleus in two species of new world monkey: Saimiri sciureus and aotus trivirgatis. *J Physiol*, 523 Pt 3:755-769.

Vaughn, J.E. (1989). Review: fine structure of synaptogenesis in the vertebrate central nervous system. *Synapse, 3: 255*-85.

Vaughn, J.E., Henrikson, C.K., and Grieshaber, J.A. (1974). A quantitative study of synapses on motor neurons dendritic growth cones in developing mouse spinal cord. *J Cell Biol, 60*: 664-72.

Vaughn, J.E., Barber, R.P., and Sims, T.J. (1988). Dendritic development and preferential growth into synaptogenic fields: a quantitative study of golgi-impregnated spinal motor neurons. *Synapse, 2*: 69-78.

Verma, A.S., and Fitzpatrick, D.R. (2007). Anophthalmia and microphthalmia. *Orphanet J Rare Dis.* 26;2:47.

Wang, S.W., Kim, B.S., Ding, K., Wang, H., Sun. D., Johnson, R.L., Klein, W.H., and Gan, L. (2001). Requirement for math5 in the development of retinal ganglion cells. *Genes and Development*, 15: 24-9.

Wee, R, Castrucci, A.M, Provencio, I, Gan, L, and Van Gelder, R.N. (2002). Loss of photic entrainment and altered free-running circadian rhythms in *math5*$^{-/-}$ mice. *J Neurosci*, *22*(23):10427–10433.

Williams, A.L, Reese, B.E, and Jeffery, G. (2002). Role of retinal afferents in regulating growth and shape of the lateral geniculate nucleus. *J Comp Neurol*, 445(3):269-77.

Williams, S.R., Turner, J.P., Anderson, C.M., and Crunelli, V. (1996). Electrophysiological and morphological properties of interneurones in the rat dorsal lateral geniculate nucleus in vitro. *J Physiol*, 490:129-47.

Winkelmann, E., Garey, L.J., and Brauer, K. (1985). Ultrastructural development of the dorsal lateral geniculate nucleus of genetically microphthalmic mice. *Exp Brain Res*, 60: 527-534.

Yonehara, K., Shintani, T., Suzuki, R., Sakuta, H., Takeuchi, Y., Nakamura-Yonehara, K., and Noda, M. (2008). Expression of SPIG1 reveals development of a retinal ganglion cell subtype projecting to the medial terminal nucleus in the mouse. *PLoS One*, 3:e1533.

Zhu, H., and Luo, L. (2004). Diverse functions of N-cadherin in dendritic and axonal terminal arborization of olfactory projection neurons. *Neuron, 42*: 63-75.

Ziburkus, J., Lo, F.S., and Guido, W. (2003). Nature of inhibitory postsynaptic activity in developing relay cells of the lateral geniculate nucleus. *J Neurophysiol*, 90:1063

Appendix I

Morphologically distinct classes of relay cells exhibit regional preferences in the dorsal lateral geniculate nucleus of the mouse

Thomas E. Krahe, Rana N. El-Danaf, Emily K. Dilger, Scott C.Henderson and William Guido.
In review, Journal of Neuroscience

Abstract

A fundamental feature of the mammalian visual system is the presence of separate channels that work in parallel to efficiently extract and analyze specific elements of a visual scene. Despite the extensive use of the mouse as a model system, it is not clear whether such parallel organization extends beyond the retina to subcortical structures like the dorsal lateral geniculate (dLGN) of thalamus. To begin to address this we examined the morphology of biocytin filled relay cells recorded in dLGN of mice. Based on a quantitative assessment of their dendritic architecture we found that even at early postnatal ages relay cells could be readily classified as X-(bi-conical), Y-(symmetrical) or W-like (hemispheric) and that each cell type was regionally specified in dLGN. X-like cells were confined largely to the monocular ventral region of dLGN. Y-like cells occupied a central core that also contained ipsilateral eye projections, whereas W-like cells were found along the perimeter of dLGN. Similar to cat, Y-like cells were more prevalent than X- and W-like cells, and X-like cells tended to be smaller than other cell types. However, the dendritic fields of X- and W-like cells did not exhibit an orientation bias with respect to optic tract or boundaries of dLGN. While we found clear morphological

differences among relay cells, an analysis of their electrophysiological properties did not reveal any additional distinguishing characteristics. Overall, these data coupled with recent observations in the retina suggest that the mouse has many of the hallmark features of a system wide parallel organization.

Introduction

The visual system of many mammals consists of separate parallel pathways that are designed to analyze different aspects of the visual scene (Lennie, 1980; Stone, 1983; Nassi and Callaway, 2009). The discovery of such organization has relied heavily on anatomical and electrophysiological descriptions, but an understanding of the molecular mechanisms underlying their specification and assembly remains largely unresolved. However, the advent of mouse models, which delineate genetically encoded markers for specific cell types, has created a wealth of opportunity to explore such avenues (Gong et al., 2007; Rotolo et al., 2008; Badea et al., 2009; Siegert et al., 2009). For example, in the retina several classes of retinal ganglion cells (RGCs) have been identified, and many of these seem to comprise separate channels that have distinct molecular, morphological and functional features, as well as unique patterns of connectivity and central projections (Hattar et al., 2006; Huberman et al., 2008; Kim et al., 2008; Yonehara et al., 2008; Huberman et al., 2009; Siegert et al., 2009; Ecker et al., 2010; Kim et al., 2010; Hong et al., 2011; Kay et al., 2011; Rivlin-Etzion et al., 2011). Nonetheless, what remains unexplored in the mouse is whether these separate retinal channels are preserved and recapitulated in a parallel manner onto recipient cells in central target structures. For instance, in the dorsal lateral geniculate nucleus (dLGN) of many mammals at least three different classes of dLGN relay cells have been identified (Stone, 1983; Nassi and Callaway, 2009). Perhaps the most extensively studied have been X-, Y- and W-cells of the cat (Sherman and Spear, 1982; Sherman, 1985). These cell types are morphologically and functionally distinct, receive information from analogous classes of RGCs, and exhibit strong regional preferences within dLGN. While there is some evidence for a similar organizational scheme in the rat (Reese, 1988), it is not clear whether mouse thalamocortical cells are functionally or even

morphologically distinct (Grubb and Thompson, 2003; Jaubert-Miazza et al., 2005). In fact, it is not even known whether different classes of relay cells exist and if so, where they reside, or when during development they are specified.

To begin to address these issues, and as a prelude to understanding the bases of the morphological diversity of dLGN cells, we examined the dendritic architecture of relay cells at different postnatal ages in a commonly used pigmented strain (C57/BL6) of the mouse. We made use of an acute thalamic slice preparation in which individual cells were filled with biocytin during whole cell recordings and then reconstructed using confocal microscopy. By applying a quantitative assessment of their dendritic orientation and tracking the location of filled cells with respect to the boundaries of dLGN as well as eye-specific domains within it, we were able to assess whether morphologically distinct classes of cells resided in discrete locations of dLGN.

Materials and Methods

Animals

C57/BL6 mice between postnatal ages (P) 1-40 were used. Pups were bred in a resident colony from breeders that were obtained from commercial vendors. For all surgical procedures, animals were deeply anesthetized with isoflurane vapors. All experiments were conducted under the guidelines of the Institutional Animal Care and Use Committee at Virginia Commonwealth University.

Slice physiology, intracellular filling, and tissue preparation

To visualize eye-specific domains and the boundaries of dLGN during the recording, we first made intravitreal injections of the anterograde tracer cholera toxin B subunit (CTB, 3-5 µL 1.0% solution dissolved in distilled water) conjugated to Alexa Fluor 488 or 555 (Invitrogen). Following a 24-48 hr survival period, mice were prepared for acute in vitro thalamic slice recordings (Bickford et al., 2010). Because these mice were part of another study that involved the examination of synaptic responses, we adopted a modified sagittal slice preparation that retained retinal axonal input and intrinsic circuitry of dLGN (Chen and Regehr, 2000; Bickford et al., 2010). Typically, we were able to generate two slices through the dorsal thalamus that contained a relatively complete section of dLGN. To confirm our initial findings regarding the regional preferences of identified cell types, additional experiments were conducted in a coronal slice preparation. Individual (250-300 µm thick) slices containing dLGN were placed into a recording chamber maintained at 32°C and perfused continuously at a rate of 2.0 ml/min with oxygenated ACSF (in mM: 124 NaCl, 2.5 KCl, 1.25 NaH_2PO_4 , 2.0 $MgSO_4$, 26 $NaHCO_3$, 10 glucose, 2 $CaCl_2$, saturated with 95% O_2 /5% CO_2 , pH=7.4). In vitro intracellular recordings

were done in the whole-cell current clamp configuration with the aid of IR-DIC and fluorescence optics (Olympus VX51) on a fixed stage, visualized recording apparatus. Patch electrodes (3-7 MΩ) made of borosilicate glass were filled with a 5% biocytin solution containing (in mM): 130 K Gluconate, 10 HEPES, 8 NaCl, 2 ATP-Mg, and 0.1 GTP-Na (pH=7.25). Once whole cell recording was established, neurons were filled with biocytin by passing alternating positive and negative current pulses (+ 0.5 nA, 200 msec) through the recording electrode. For some cells, we examined their membrane properties and firing characteristics by recording the voltage responses to intracellular injections of square wave current pulses (+0.01 nA steps, 900 ms duration). After recording, slices were fixed overnight with 4% paraformaldehyde in 0.1 M phosphate buffer solution (pH=7.2) and then incubated for 24 hrs in a 0.1% solution of Alexa Fluor 647 conjugated to streptavidin (Invitrogen) dissolved in PBS with 0.1% Triton X-100. Slices were washed with PBS and then mounted with ProLong Gold (Invitrogen), cured overnight at room temperature and stored in a freezer at -20°C. Sections were initially visualized and photographed with an upright epi-fluorescence microscope (Nikon E6000) to select labeled cells that were suitable for confocal laser scanning microscopy. Relay neurons were readily distinguished from interneurons by the appearance of round somata, radially oriented dendritic trees, and axons that exited the dLGN (Parnavelas et al., 1977).

Cellular imaging and reconstruction

Reconstructions were done using a multi-photon/confocal laser scanning microscope (Zeiss LSM510 NLO Meta). Fluorescence from labeled dLGN neurons was excited using a 633 nm HeNe laser and emission was detected over a range of 651–694 nm. Targeted neurons were imaged with a Plan-Neofluar 40x (1.3 n.a.) oil immersion objective or a C-Apochromat 40x (1.2 n.a.) water immersion objective at a scan resolution of 2048x2048 pixels. 3-D datasets, collected

through a depth of 20-100 µm were compiled from a sequential series of optical slices with a step size through the z-axis of 0.48 µm (40x, 1.2 n.a.) or 0.5 µm (40x, 1.3 n.a.). Z-stack datasets were rendered and analyzed offline using Volocity software (Improvision, version 4.3.2). Image stacks were collected in a plane that was orthogonal to the slice and were then deconvolved using an iterative restoration technique to reduce signal noise generated from outside the focal plane of interest. Threshold values were set according to signal intensity and background noise. For cells in which it was not possible to obtain a complete reconstruction of their dendritic field (e.g., cut dendrites that exited the slice), or where neighboring cells had overlapping dendritic arbors, or where there was an excessively high background due to apparent leakage of dye in the surrounding neuropil were excluded from the study. The location of labeled cells was noted by examining their position with respect to boundaries of dLGN and eye-specific domains, delineated by CTB labeled retinal projections. Regional preferences were statistically assessed by performing chi-square (χ^2) analyses on the expected and observed frequencies. To confirm the statistical power of χ^2 tests, Monte Carlo simulations (n=1000) were run whenever observed frequencies were less than 5.

Results

A total of 98 relay neurons in mice ranging in age from P1-40 were filled with biocytin during intracellular recording and then reconstructed using confocal microscopy (Fig. 1). Representative examples are shown in Fig. 2A. Relay cells had type I or class A morphology (Parnavelas et al., 1977) which consists of a thick unbranched axon, relatively large round somata and multipolar dendritic arbors comprised of 6-7 primary dendrites. In fact, even cells at early postnatal ages had fairly large somata and complex dendritic trees with a distinct architecture. Nonetheless, we did observe a substantial change in dendritic architecture after the first postnatal week (Fig. 2B-C). Between P1-5, dendritic trees contained about 40 branches. At these ages, the majority of branching was confined to the 2 nd through 4 th order, but some neurons displayed branches up to the 6 th -8 th order (Fig. 2C). However as shown in Fig. 2B, after P7, dendritic complexity showed a significant increase (one-way ANOVA, $F=7.154$, Bonferroni post hoc test, $P<0.01$ for all comparisons) but then stabilized, such that the total number of branches (80-100) and degree of higher order branching (3^{rd} - 9^{th}) were similar for cells across a wide range of postnatal ages (P7-40, Fig. 2C). By contrast as shown in Fig. 2D, soma surface area while somewhat variable did not show any significant changes with age. Thus, similar to the observations made in the developing rat dLGN (Parnavelas et al., 1977), relay cells in mouse undergo a rapid growth spurt during early postnatal life. By P7, dendritic branching stabilized and profiles took on a highly stereotypic architecture. All subsequent analyses were conducted on cells between ages P7-40.

To assess whether these dendritic patterns could be quantified and used as a means to distinguish different morphological subtypes of dLGN cells, we employed a Sholl ring analysis (Friedlander et al., 1981). For 73 cells we compiled a Z-stack, and on the projection image,

placed five concentric rings at equidistant intervals (range: 15-27 μm) centered on the soma. The radius of the innermost ring (the most proximal from the soma) was based on the breadth of the total dendritic field, so that the outermost ring (the most distal from the soma) encompassed all but the tips of the longest dendrites. The rings were divided into four quadrants (a1 , a2 and b1, b2) by passing two lines through the center of the soma at right angles to one another (Fig. 3A). In studies that employ Sholl rings, these axial lines are oriented perpendicular (vertical) and parallel (horizontal) to eye-specific laminar borders within dLGN (Friedlander et al., 1981; Stanford et al., 1981; Stanford et al., 1983). Such positioning ensures that the Sholl ring analysis captures the strong orientation biases in dendritic architecture of some classes of dLGN cells. However, the mouse dLGN lacks such lamination (Jaubert-Miazza et al., 2005). Instead retinal projections from the ipsilateral eye occupy only about 10-15% of the nucleus and form an irregularly shaped patch that courses through the anteromedial region. Thus, in keeping with previous strategies (Friedlander et al., 1981; Stanford et al., 1981; Stanford et al., 1983), the lines delineating the quadrants of the Sholl rings were arranged to maximize the difference in dendritic intersections between the two axial planes. For a given cell, the number of dendritic intersections passing through each ring was counted and grouped by axial plane (a1 +a2 or b1 +b2). The ratio of the minimum number of intersections in one plane versus the maximum number in the other was taken as an index of dendritic orientation (DOi). A DOi of 1.0 represents a cell with equal number of intersections in both axial planes, whereas a cell with intersections in just one plane would have a DOi of 0.0.

A k-means cluster analysis (Hartigan and Wong, 1979; Blashfield and Aldenderfer, 1984) was then conducted to examine the independent grouping of cells by their pattern of dendritic orientation. Since the algorithm requires that k, the number of expected clusters, must be

specified a priori, we used the "elbow criterion" as a convenient heuristic to estimate the optimal number of clusters, if any (Jain et al., 1999; Chen et al., 2007). Briefly, this criterion is based on the plot of the ratio of the between-group variance to the total variance (total sum of squares) as a function of cluster number (Fig. 3B). As the number of clusters increases the total variance explained by the data increases monotonically until a further increase in the number of clusters reaches a plateau. Thus, the location of the "elbow" is used to delineate the appropriate number of clusters within a given dataset. In other words, the elbow identifies the optimal number of clusters up to the point where adding additional ones would not significantly account for a change in the total variance. Finally, it should be noted that the absence of an elbow may be an indication that there is no cluster structure in the data.

When these analyses were applied to DOi values of biocytin filled cells, three clusters were identified (Fig. 3B). As illustrated in the frequency distribution of DOi values (Fig. 3C), three distinct groups existed (Kruskal-Wallis test, χ^2 =60.94, P<0.0001). Representative cells from each group are shown in Fig. 3D. The group on the far left of the DOi distribution (Fig. 3D, left panel) represents cells with dendritic intersections that were restricted to only one axial plane, while those in the middle of the distribution (Fig. 3D, middle panel), had values that reflected intersections that were found in one plane and the quadrant of the other, whereas those on the far right (Fig. 3D, right panel) had an equivalent number of intersections in one axial plane or the other.

To better illustrate the dendritic architecture of cells in each of these groups, we generated polar plots that were based on the outermost dendritic intersections occurring within each one of the rings (Fig. 3E). For each of these intersections we then measured the radial length and the corresponding angle using the soma center as the point of origin. Summary

histograms (Fig. 3F) which plot these lengths as a function of angle, further underscore the existence of three morphological subtypes. Indeed, each group bears a striking resemblance to X, Y- and W-cells of the cat (Friedlander et al., 1981; Stanford et al., 1981; Stanford et al., 1983). Cells with X-like morphology had a bi-conical shape and orientation preferences that were 180° apart from each other. Cells with W-like morphology had a hemispheric profile with orientation preferences that occupied all but one quadrant. Finally, cells with Y-like morphology had a profile that was radially symmetric, and showed no orientation preference in their dendritic tree. The relative proportions in which each of these subtypes was encountered were also similar to values reported in the cat. From a total of 73 cells close to half (49%) were Y-like, 22% X-like, and 29% W-like (χ^2 =11.53, df=2, p<0.01; Y-cell, z=2.77, P<0.01). Moreover, we found that X-like cells tended to be smaller than W- and Y-like cells. For example, Table 1 reveals that dendritic and soma surface area, as well as the spatial extent of their dendritic fields, was comparatively smaller for X-like cells. Indeed, these differences do not appear related to the postnatal age of cells in each group (one-way ANOVAs, F= 0.406 for surface area, F=0.629 for dendritic field, P>0.53 for both comparisons).

In the absence of eye-specific lamination, we instead investigated whether dendritic architecture of X- and W-like cells exhibited a particular orientation bias with respect to the borders of dLGN. Interestingly, unlike the cat (Friedlander et al., 1981; Stanford et al., 1981; Stanford et al., 1983), X- and W-like cells in the mouse did not exhibit a particular orientation preference. Fig. 4 provides examples of how the dendritic trees of X- and W-like cells were aligned either with respect to optic tract (X-like) or the boundaries of dLGN (W-like). These references points were chosen based on the strong regional preferences each cell type displayed (see below). For X-like cells roughly half had their bi-conical shape arranged perpendicular to

the optic tract, while the others were aligned in parallel (Fig. 4C left, χ^2 =0.2, df=1, P=0.66). For W-like cells, just as many were likely to have their hemispheric dendritic profile facing towards as away from the borders of dLGN (Fig. 4C right, χ^2 =0.04, df=1, P=0.84). It is important to note that the analysis of W-like cells was restricted to those with a soma that was within 100 µm of a border, indicating that the boundaries of the nucleus did not pose as a physical determinant of morphological subtype.

While we found clear morphological differences among relay cells, an analysis of their active and passive membrane properties showed no additional distinguishing characteristics. For 44 biocytin filled cells (X- n=12, W- n=10, Y-like n=22) we recorded whole-cell voltage responses evoked by intracellular current injection. Fig. 5A provides representative examples of voltage responses and I-V relations for each of the identified groups. X-, W-, and Y-like cells possessed the full complement of voltage-gated conductances that are typically reported for dLGN relay cells (Crunelli et al., 1987; Crunelli et al., 1989; Williams et al., 1996; MacLeod et al., 1997; Ziburkus et al., 2003; Jaubert-Miazza et al., 2005). For example, membrane hyperpolarization activated a mixed cation conductance (H) that led to strong inward rectification (i.e., depolarizing sag). The cessation of hyperpolarizing current steps and passive repolarization of membrane levels evoked large triangular "rebound" low threshold Ca^{2+} spikes (LT) and burst firing (B). Membrane depolarization activated an outward rectifying K^+ conductance, which delayed the onset of spike firing (A). Finally, strong levels of membrane depolarization produced spike trains that exhibited frequency accommodation (AHP). As shown in Fig. 5B, values of resting membrane potential (Vm), input resistance (IR), and membrane time constant (τ 0) were also not different among X-, W-, and Y-like cells (one-way ANOVAs, F=1.031 for resting Vm, F=0.532 for I R , F=0.199 for τ 0 , P>0.36 for all comparisons).

To examine whether these morphologically defined cell types reside in specific regions of the dLGN we tracked the location of 61 cells from a total of 36 slices in which they were recorded (Fig. 6). An example of a typical slice along with CTB labeled terminal fields delineating the boundaries of dLGN and eye-specific domains are shown in Fig. 6A. Because dLGN slices varied in size and shape, we normalized each one with respect to its maximum height and width. Outlines of each slice along with the relative position of filled cells are shown in Fig. 6B. While cells of each group were not completely segregated within dLGN, clear regional preferences were apparent. For example, the majority of X-like cells were located near the ventral-posterior border of dLGN, adjacent to the intrageniculate leaflet (IGL) and ventral lateral geniculate nucleus (vLGN) in a region that corresponds to the monocular segment (Coleman et al., 2009). W-like cells were dispersed along the outer boundaries of dLGN, in regions that lie near the optic tract or the opposing border of the nucleus. Y-like cells were broadly distributed throughout dLGN but were most prevalent within a central band that coursed throughout its length in a plane that was roughly parallel to the optic tract.

To assess these preferences statistically we divided the cell location plot of Fig. 6B into the patterns shown in Fig. 6C (a-c, three vertical sectors; d-f, three horizontal sectors; and g-h, inner and outer sectors). We then compared the observed and expected frequencies for a given cell type within each of these sectors (Fig. 6C). X-like cells showed a significant regional preference in sectors a,e, and h largely because of the clustering noted in the monocular segment (a-c: χ^2 =12.40, df=2, P<0.01, Monte Carlo 0.1%; a: z=2.68, P<0.01; d-f: χ^2 =19.6, df=2, P<0.0001, Monte Carlo 0.0%; e: z=4.32, P<0.0001; g-h: χ^2 =4.26, df=1, P<0.05, Monte Carlo 2.7%). W-like cells exhibited a significant preference for sector h, which corresponds to the perimeter of dLGN (g-h: χ^2 =5.06, df=1, P<0.05, Monte Carlo 1.7%). Y-like cells showed a

significant preference for sector e, which corresponds to a central strip within dLGN (d-f: χ^2 =10.94, df=2, P<0.01, Monte Carlo 0.5%; e: z=2.71, P<0.01). Typically, this region was occupied by projections arising from the ipsilateral eye (Fig. 6A). Indeed as shown in Fig. 7, in slices where the eye-specific domains were labeled with CTB, we found that 11 of 15 cells (73%) that had their soma within this region were Y-like (χ^2 =12.88, df=2, P<0.01, Monte Carlo 0.1%; Y-like, z=2.89, P<0.01). Moreover, similar to the arrangement of Y-cells in the cat (Friedlander et al., 1981), for many Y-like cells in mouse, their dendritic fields extended beyond the boundaries of the ipsilateral eye into regions occupied by contralateral eye terminal fields. Finally, as shown in Fig. 6D, the regional preferences noted above were also apparent in thalamic slices cut in the coronal plane (21 slices, n=31 cells; a-b: X-like, χ^2 =4.16, df=1, P<0.05, Monte Carlo 3.5%; W-like χ 2 =8.64, df=1, P<0.01, Monte Carlo 0.1%; Y-like, χ^2 =0.00, df=1, P=1.0).

To better illustrate the spatial relations of identified cell types we generated summary diagrams (Fig. 8) that incorporated cell locations from slices cut in the parasagittal and coronal plane. Overall, X-like cells resided in the monocular segment of dLGN near the ventral border separating dLGN from IGL. W-like cells seemed to form a ring around the perimeter of dLGN. In fact, for most (79%, 22/28) their soma was located with 100 µm of the boundaries of the nucleus (χ^2 =8.04, df=1, P<0.01). Finally Y-like cells were more evenly dispersed throughout a central core of dLGN, and compared to X- and W-like cells, they showed a strong preference for the binocular region of dLGN (Caviness et al., 1980; Coleman et al., 2009).

Figure 1

Recording preparation, cellular labeling, and confocal reconstruction of mouse dLGN cells.

A. Panels depict actual fluorescence and DIC images taken through the upright microscope during in vitro slice recording. Left and middle panels show anterograde labeling of retinal projections with CTB conjugated to Alexa Fluor 488 or 555. Far right panel is a DIC image of the same slice showing a patch pipette filled with biocytin. B. Same sections as in (A) but here the slice is fixed and photographed through an upright epi-fluorescence microscope. Shown are crossed (left panel, green) and uncrossed (middle panel, red) retinal projections along with three biocytin-filled cells (right panel, pseudo-colored in blue but labeled with far-red Alexa Fluor 647). The solid blue line delineates the boundaries of dLGN. Scale bar, 200 µm. C. Higher-magnification of far right panel in (A) showing DIC image of a dLGN relay cell with the tip of the patch pipette. Scale bar, 5 µm. D. Same relay cell shown in (C) and (B, far right panel, middle cell) after fixation and streptavidin reaction. A-D are from the same slice taken from a P17 mouse. E. Example of a biocytin-labeled interneuron from another dLGN slice of a P14 mouse. Relay cells and interneurons have distinct morphology and can be readily distinguished. Scale bar, 20 µm. F. Confocal sequential series of optical slices of a dLGN neuron (at P15) with a step size through the Z-axis of 0.48 µm. G. Projection image of the 3-D rendered cell shown in (F). Scale bar, 50 µm.

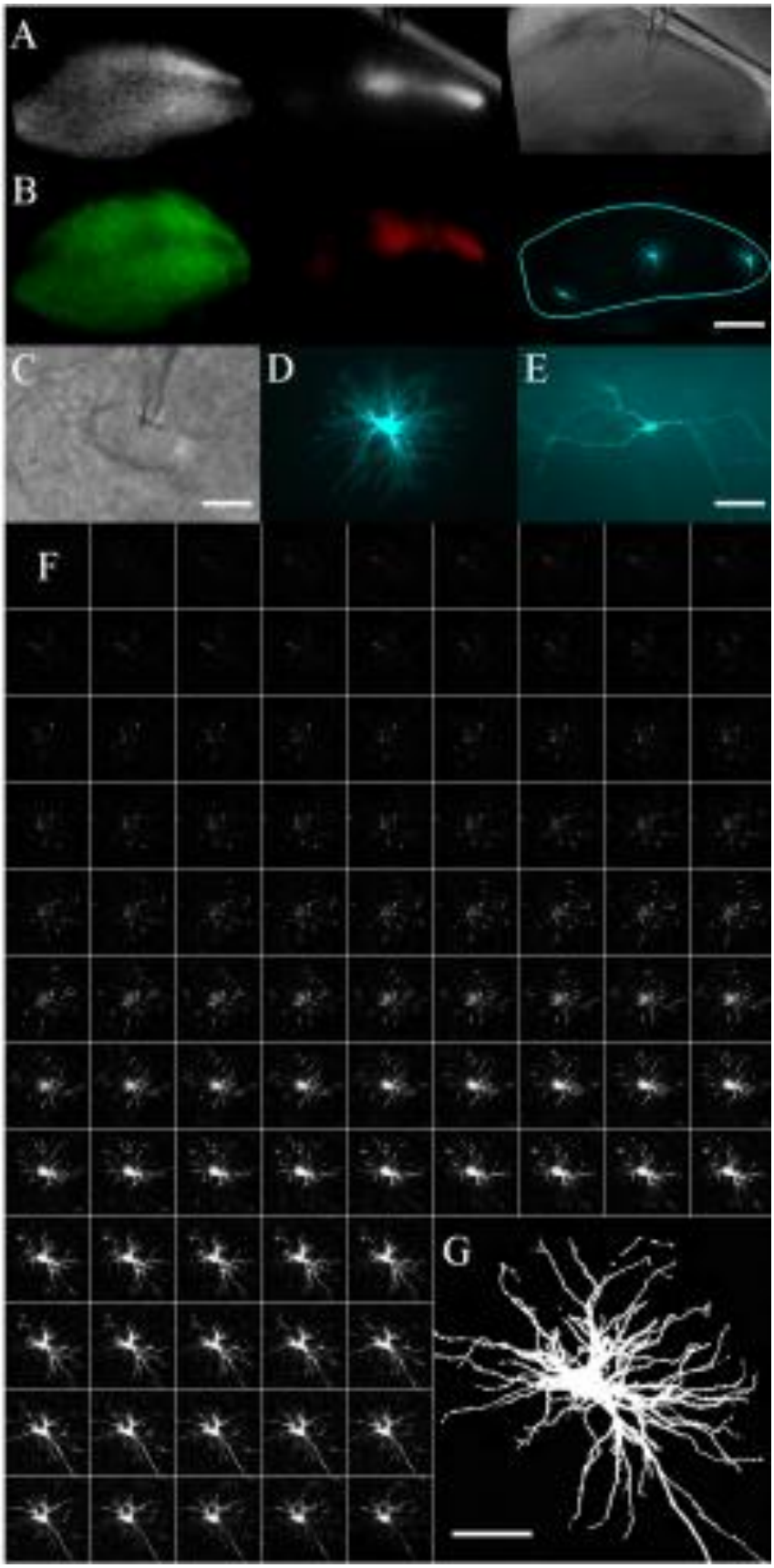

Figure 2

Morphology of developing dLGN relay cells.

A. Reconstructions are based on the Z-stack images of representative relay neurons filled with biocytin at different postnatal ages. Neurons are grouped by dendritic architecture (top: radially symmetric, middle: hemi-spherical, bottom: bi-conical) and arranged within a row by increasing postnatal age (P, lower right corner of each cell). Scale bar, 50 µm. B-C. Summary plots showing the mean number of branches (B) and branch order (C) at different postnatal ages. At P1-5 the complexity of relay cells is not fully mature. (P1-5, n=5 cells; P7-11, n=9; P13-19, n=7; P21-40, n=11) Error bars represent SEM. D. Scatter plot showing soma cell surface area at different postnatal ages (P1-40). Each point represents a single neuron (n=56). Linear regression is shown as the best fit line and did not reveal any correlation between soma size and postnatal age (df=56, R^2 =0.0009, P=0.83).

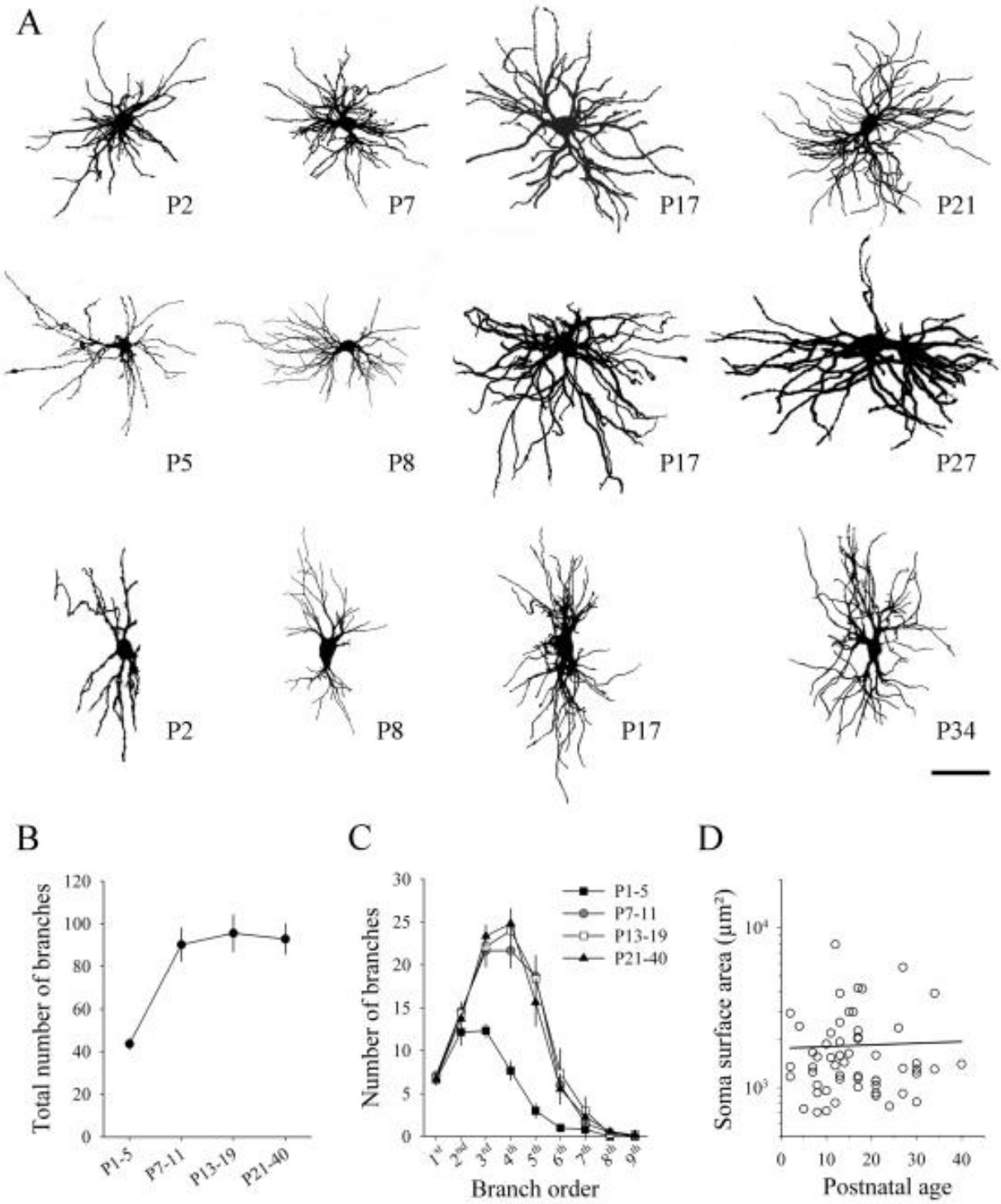

Figure 3

Quantitative assessment of dendritic architecture.

A. Example of a Sholl ring superimposed on the dendritic tree of a relay cell. The dendritic tree spans across two axial planes and four quadrants (a1, a2 and b1 , b2) quadrants. The concentric rings have equidistant intervals centered on the soma. For each cell we computed an index of dendritic orientation (DO*i*), the ratio of the minimum to maximum number of intersections in each axial plane (a1 +a2 or b1 + b2). B. Plot depicts the percentage of variance in the DO*i* values for all cells (n=73) as explained by the number of clusters. The percentage of variance explained is the ratio of the between-group variance to the total variance (see Results). The red dotted line delineates the point in the graph (three clusters) where a further increase in the number of clusters does not yield a significant change in the percent of variance explained. C. Histogram that plots the distribution of DO*i* values for all cells. Solid lines represent Gaussian fits and dotted vertical lines delineate the three clusters determined in (B). The group on the far left (0-0.49) are cells (n=16) with the least amount of intersections in one plane or the other (a1 +a2 or b1 + b2); the middle group (0.50-0.79) are cells (n=21) that had intersections in one plane and the quadrant of the other, and on the far right (0.80-1.0) are cells (n=36) that had roughly the same number of intersections in one axial plane or the other. D. Representative examples of cells in each of the defined groups from (B-C). Dashed lines illustrate the dendritic architecture. Note that each profile resembles the dendritic architecture of X-, W-, and Y- cells of the cat. Scale bar, 50 µm. E. Superimposed polar plots of the dendritic profiles (thin gray lines) for cells in each of the defined groups as determined by the analyses in (A-C). Polar plots were generated by using the outermost dendritic intersections and the soma center as the point of origin. For X-like cells, plots were arranged so their bi-conical shape was oriented vertically; for W-like cells, plots were

arranged such that the quadrant with the fewest dendritic branches appeared on top. Colored lines (red, blue, and green) depict the dendritic profiles of X-, W-, and Y-like cells shown in (D). Thick white lines are the median profiles for each group. F. Summary histograms of the average radial length of the outermost intersections at different angles depicted in plots shown in (E). Angles increase in a clockwise manner with 0° corresponding to the right horizontal axis of plots shown in (E). Bin size, 22.5°.

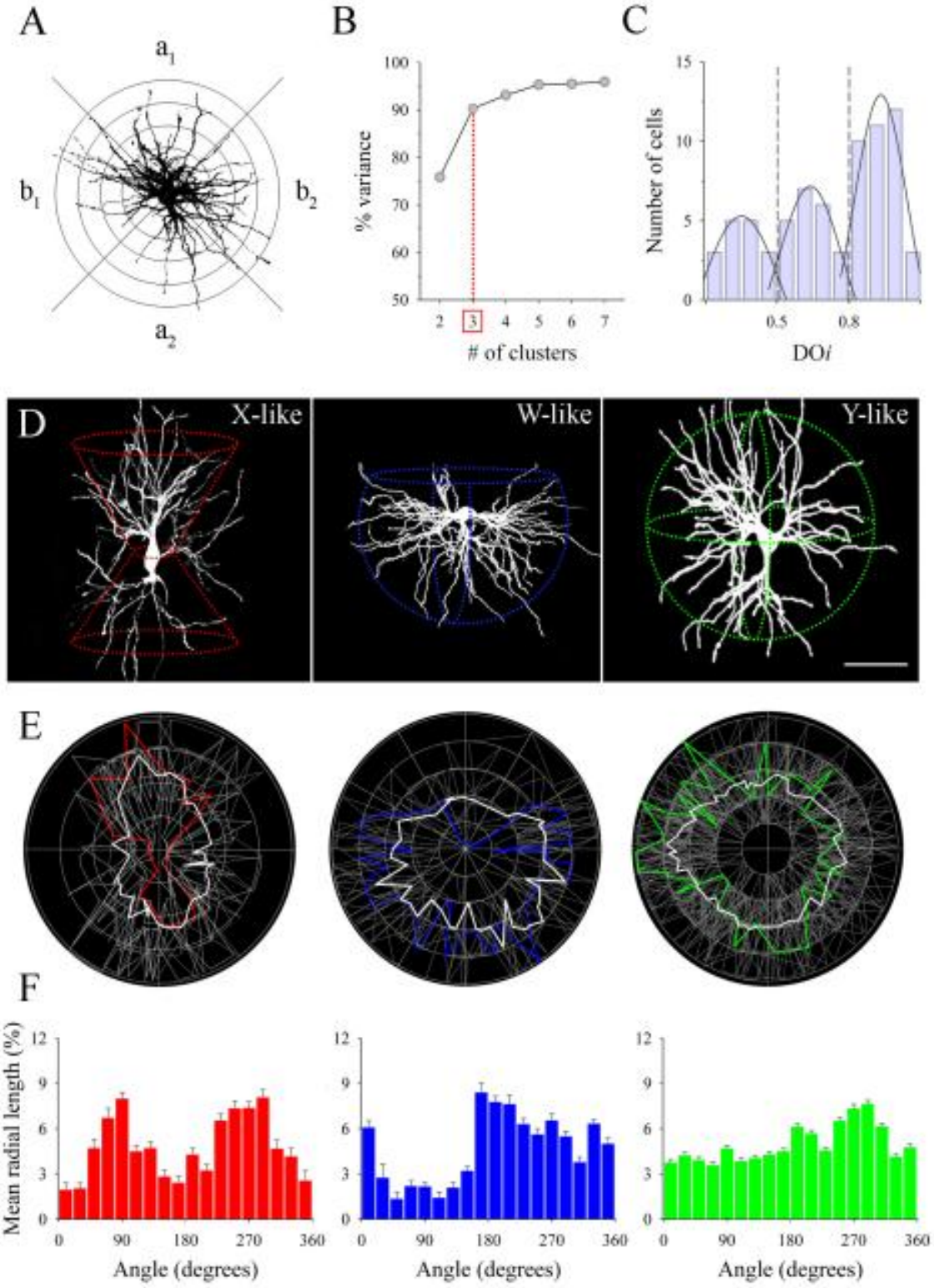

Table 1. Morphological parameters of relay cells from the mouse dLGN

Cell	Dendrite SA (μm^2) $x10^3$	Soma SA (μm^2) $x10^3$	Age	DF (μm^3) $x10^6$	Age
X	22.92 ±3.64 [57.74 ± 9.17]	1.53 ±0.17 [74.92 ± 8.42]	17.1 ± 2.87 (12)	1.55 ±0.25 [63.96 ±10.24]	17.4 ±2.5 (14)
W	39.46 ±5.92 [99.40 ± 14.90]	2.04 ±0.46 [100.00 ± 22.53]	15.9 ± 1.8 (17)	1.95 ±0.26 [80.37 ±10.84]	15.9 ±1.7 (19)
Y	39.70 ±5.47 [100.00 ± 13.79]	1.71 ±0.20 [83.73 ± 9.66]	18.2 ± 1.5 (27)	2.42 ±0.24 [100.00 ±9.98]	18.5 ±1.4 (31)

Data are presented as mean±SE. Numbers in [ ] are averaged percentages ±SE and numbers in parenthesis represent number of cells. Percent-wise, X-like cells are significantly smaller than W- and Y-like cells (Univariate ANOVA, F=3.54, *P<0.05). DF, dendritic field; SA, surface area. Age values are in postnatal days.

Figure 4

Pattern of dendritic orientation for X- and W-like cells.

A-B. Representative reconstructions of X- and W-like cells in relation to the optic tract (OT) or boundaries of dLGN. For X-like cells dendritic orientation was examined relative to OT (perpendicular or parallel, solid line). For W-like cells, orientation was examined relative to the boundaries of the dLGN (dendritic arbor away or towards, dotted line). Reconstructions are based on the Z-stack images of relay neurons filled with biocytin. Schematic drawings depict dendritic orientation for X- (red) and W-like (blue) cells (dLGN border, dotted line; OT, solid line). Scale bar, 50 µm. C. Bar graphs showing the orientation preferences for X- and W- like cells. For the latter, those cells that had their soma within 100 µm from dLGN border were included (22/28). Numbers in parenthesis depict cell counts. Schematic drawings are the same as in (A-B).

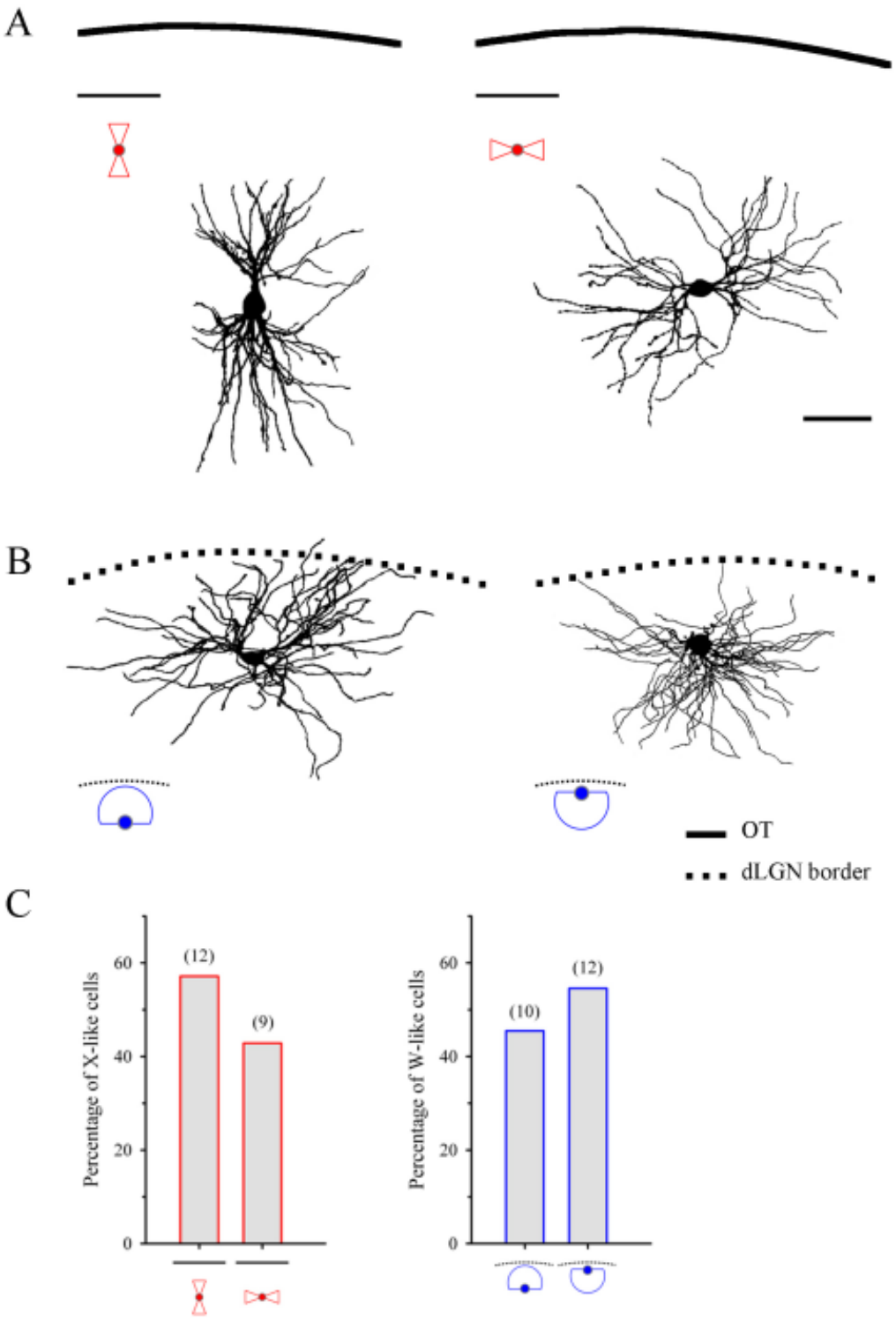

Figure 5

Membrane properties of morphologically identified cells types in dLGN.

A. Representative examples of voltage (V) responses to current (I) injections for a X- (left column, P14), W- (middle column, P24), and Y- (right column, P17) like cell. Plots below traces depict the corresponding I-V relations for each cell (±0.01 nA square-wave current pulses; 900 ms long). Note the presence of a depolarizing sag (H) during membrane hyperpolarization, the large rebound low threshold Ca^{2+} spike (LT) and burst (B) firing following the termination of the hyperpolarizing current pulse, the delay in spike firing (A) and spike frequency accommodation (AHP) during membrane depolarization. Corresponding I-V plots depict similar forms of inward and outward rectification. B. Bar graphs showing the averages for resting membrane potential, input resistance, and decay time (τ 0) for X- (n=12), W- (n=10), and Y-like cells (n=22). Error bars represent SEM.

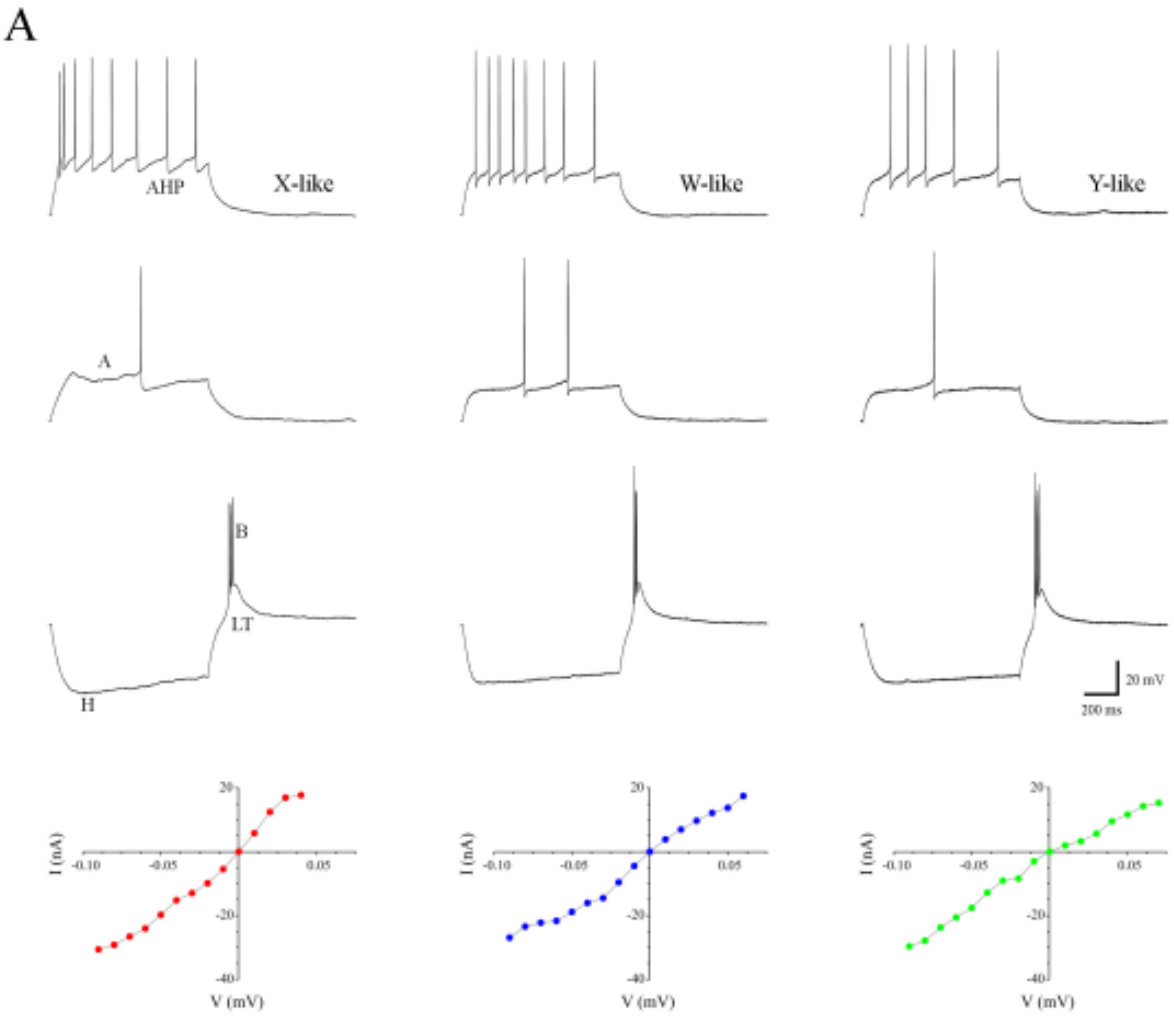

Figure 6

Location of identified cell types in dLGN.

A. An example of CTB filled section of dLGN, showing crossed (green) and uncrossed (red) retinal projections. Adjacent to the optic tract (OT) is the intrageniculate leaflet (IGL) and ventral lateral geniculate nucleus (vLGN). For purposes of orientation, a schematic of a sagittal section through the dorsal thalamus is provided (D, dorsal; A, anterior; CA3, field of hippocampus; V1, primary visual cortex; LV, lateral ventricle). B. Outlines of dLGN slices (n=36, thin gray lines) along with the relative position of each identified cell type (colored symbols: X-like, red, n=15; W-like, blue, n=14; and Y-like, green, n=32). Outlines and cell location have been normalized with respect to maximum height and width of dLGN (A). Thick black line reflects the median of all outlines. C. Cell location was assessed by dividing dLGN plot of (B) into the following sectors: a-c three vertical sectors, d-f three horizontal sectors, g-h inner and outer sectors. Below each pattern are the corresponding observed (number of cells and corresponding percentages in parenthesis) and expected frequencies (E freq) for a given cell type. Locations showing a significant spatial preference for a given cell type are marked with an asterisk (all P values <0.01 to 0.05). D. Outlines of dLGN slices (n=21) cut in the coronal plane along with the relative position of 31 identified cell types. All other conventions are the same as (B). D, dorsal; M, medial. For B and D, a total of 18 cells were classified qualitatively (X- n=5, W- n=7, and Y-like n=6).

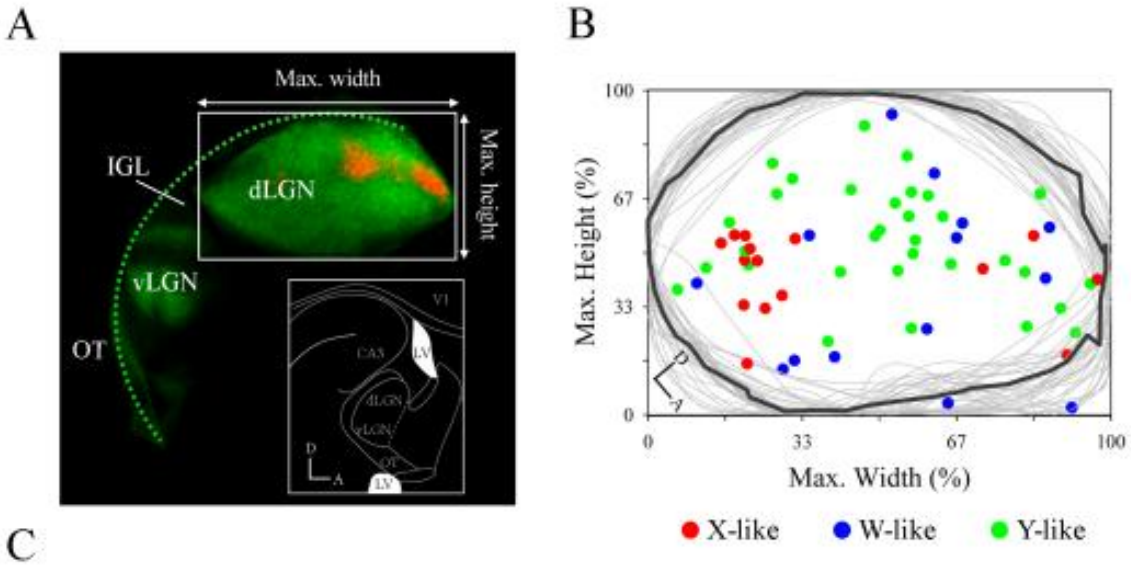

C

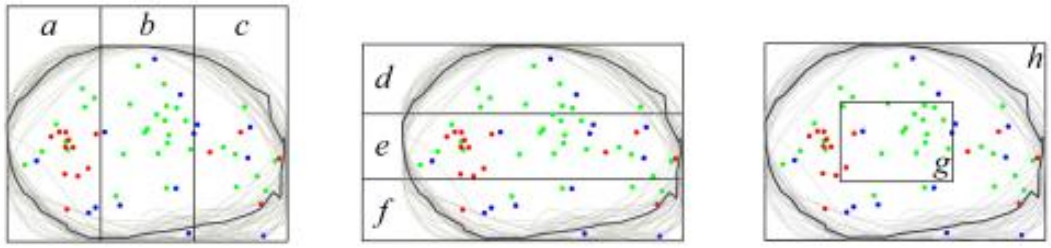

	a	b	c	d	e	f	g	h
X	11 (73)*	0 (00)	4 (27)	0 (00)	13 (87)*	2 (13)	2 (13)	13 (87)*
W	3 (21)	6 (43)	5 (36)	2 (14)	6 (43)	6 (43)	2 (20)	12 (80)*
Y	8 (25)	17 (53)	7 (22)	9 (28)	19 (59)*	4 (13)	14 (44)	18 (56)
E_{Req}	$\frac{1}{3}$(33.3)	$\frac{1}{3}$(33.3)	$\frac{1}{3}$(33.3)	$\frac{1}{3}$(33.3)	$\frac{1}{3}$(33.3)	$\frac{1}{3}$(33.3)	$\frac{1}{2}$(50)	$\frac{1}{2}$(50)

D

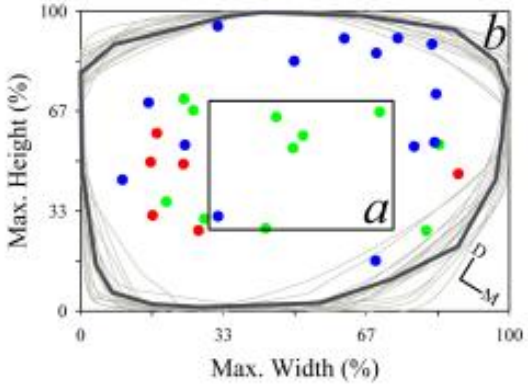

Figure 7

Location of identified cell types relative to eye-specific domains in dLGN.

A-C. Panels illustrate representative CTB-filled sections of dLGN taken from a P12 (top row) and P17 mouse (bottom row). A-B. Crossed projections are shown in green (A) and uncrossed ones from the same section in red (B). C. Higher-magnifications of insets in (B) depict relay cells located within (top panel) or on the border (bottom panel) of the uncrossed retinal projections region (red lines). Biocytin filled relay cells in A-C are in blue. Scale bars, 200 µm for (A-B) and 100 µm for (C). D. Outlines of normalized dLGN slices (n=11) containing cells located inside or near the borders of uncrossed retinal projections. Green lines represent the boundaries of dLGN and red lines the domains of uncrossed retinal projections. Filled circles represent cell soma location and the line around them the corresponding dendritic field. Bottom-right panel depicts all dLGN outlines and cell somas. The majority of cells (11/15) located in or near the ipsilateral eye terminal domain,are Y-like. Note also that in several cases dendritic fields extend beyond the boundaries into regions innervated by the contralateral eye.

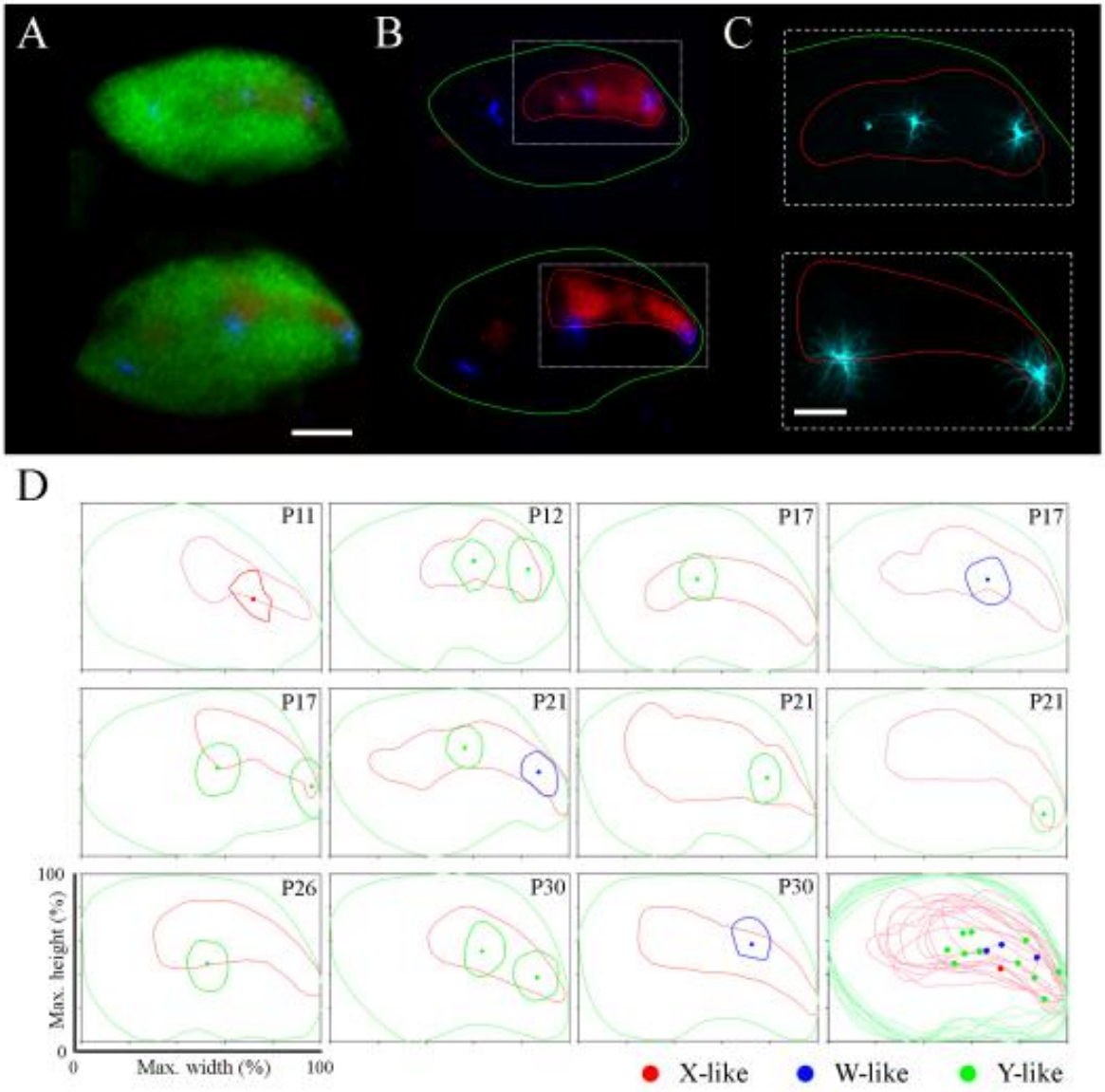

Figure 8

Summary diagrams showing the regional preferences of different cell types in dLGN.

A. Drawing illustrating the relative position of X- (red), W- (blue), and Y-like cells (green) in parasagittal (filled circles, see Fig. 5B) and coronal (filled triangles, see Fig. 5D) planes of dLGN. Both planes were intersected and rotated to provide a 3-D rendering of the dLGN. OT, optic tract; A, anterior; D, dorsal; L, lateral. B. Similar diagrams to (A) where each color highlights the preferred location of each cell type in the dLGN.

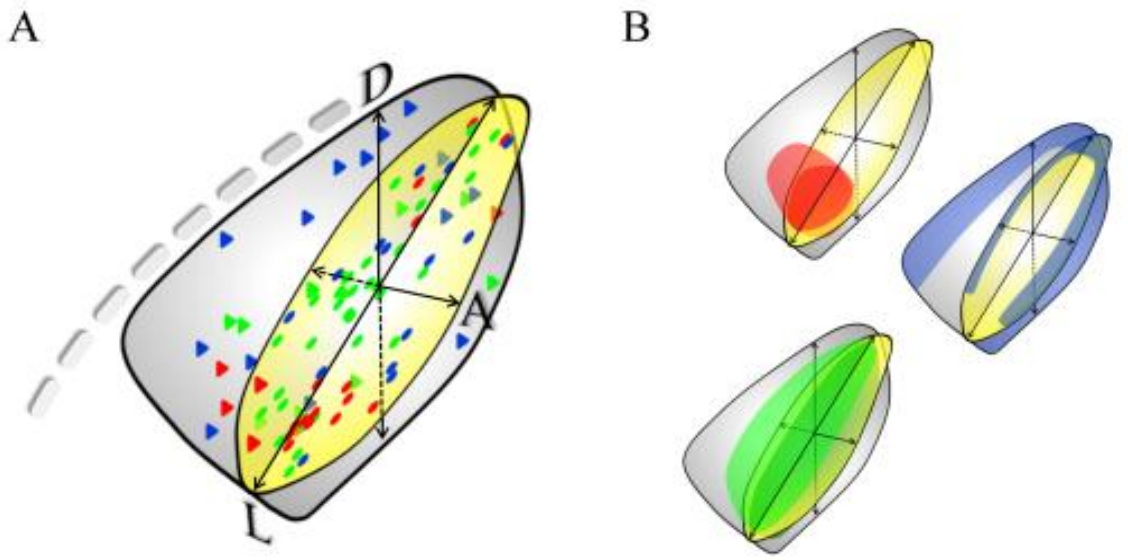

Discussion

A key element of parallel pathway organization is the presence of separate cell types at all levels of processing. While such organization is readily apparent in carnivores and primates it is unclear whether the mouse has separate channels that remain segregated beyond the retina. Here we report that relay cells in the mouse dLGN are morphologically distinct and have dendritic architecture that closely resembles X-, Y- and W-cells of the cat. Moreover, these cell types showed regional preferences within dLGN, with Y- and X-like cells displaying an anterior to posterior gradient and W-like cells surrounding the perimeter of dLGN. In fact, these regional preferences are consistent with studies done in the rat suggesting that the rodent dLGN is organized into two separate domains; a rostro-ventral central core comprised of cells that receive input largely from fast conducting, large, type I RGCs; and an outer caudo-dorsal shell comprised of cells that receive input from slowly conducting, smaller type II and III RGCs (Reese, 1988). Additional anatomical evidence seems to support the presence of a third domain, located in the postero-dorsal region (i.e., monocular segment) that serves as a recipient zone for subset of smaller type II and III RGCs (Martin, 1986).

Thus, our results in the mouse add to the growing list of evidence in support of a system wide parallel organization for the rodent. Nonetheless, it is important to consider them in the context of the following unresolved issues. First, while morphologically distinct, are relay cells in the mouse functionally distinct? Second, do the regional preferences of mouse relay cells in dLGN correspond to the reported axon terminal domains for different subtypes of RGCs? Finally, are mouse relay cells positioned to serve as a parallel conduit of information for certain regions of visual cortex? Each of these questions is considered below.

In the mouse, it remains unclear if morphologically defined subtypes of relay cells possess different functional properties. Indeed, an analysis of their membrane properties did not reveal any obvious differences, a trend that has also been noted in the rat and cat (Sherman and Koch, 1986; Crunelli et al., 1987; Crunelli et al., 1989; Soltesz et al., 1989; Williams et al., 1996; Ziburkus et al., 2003). Moreover, what little evidence there is on the structure-function relations of mouse dLGN cells, suggests that the receptive field properties of mouse dLGN cells are known more for their homogeneity rather than their diversity (Grubb and Thompson, 2003; 2005). In general, mouse dLGN cells display a center-surround organization (on-center or off-center) and linear spatial summation. Most notable is the lack of non-linear spatial summation, since the latter is a distinguishing characteristic of Y-cells recorded in the cat (Friedlander et al., 1981). Instead, in this regard the mouse dLGN seems more like the primate. In the latter, all cells, including M-cells the homologue of Y-cells, show linear spatial summation (Derrington and Lennie, 1984; Usrey and Reid, 2000). Also noteworthy is the reported absence of direction selectivity in mouse dLGN, since this is a defining feature for a number of identified RGC types that form lamina-like projection domains especially in the dorso-lateral tier of dLGN (Kim et al., 2008; Huberman et al., 2009; Kim et al., 2010; Rivlin-Etzion et al., 2011). However until these regions have been properly sampled during in vivo recordings, the possibility still exists that relay cells located here may in fact exhibit some form of direction selectivity. Perhaps as suggested by Huberman et al. (2009), mouse dLGN cells are more broadly tuned for direction selectivity and receive convergent input from more than one type of direction selective RGC.

While morphologically distinct groups of mouse relay cells showed strong regional preferences in dLGN, they do not seem positioned to serve as an exclusive recipient zone for any one class of RGCs. For example, we found that Y-like cells occupy a central core in dLGN, a

region that serves as the primary terminal domain for transient Off-α-cells and a group of On/Off direction-selective cells that responds to posterior motion (Huberman et al., 2008; Kim et al., 2010; Kay et al. 2011). These RGC cell types also terminate in ventro-medial regions of dLGN, an area where some W-like cells were located. Additionally, we found that X-like cells which showed perhaps the strongest regional preference residing almost exclusively in the ventro-posterior region of dLGN just dorsal to the intrageniculate leaflet (IGL), seem to represent just a small portion of much larger terminal domains for several indentified RGC types that vary both in morphology and receptive field structure (Hattar et al., 2006; Huberman et al., 2008; Kim et al., 2008; Badea et al., 2009; Huberman et al., 2009; Siegert et al., 2009; Ecker et al., 2010; Kim et al., 2010; Kay et al., 2011). Indeed, such overlap between RGC projections and the spatial preferences of dLGN cells is to be expected given the wide diversity of RGC types (Masland, 2001). Perhaps, a more likely scenario is one where multiple classes of RGCs that either share a common property, or are broadly tuned for one, converge onto a specific cell type in dLGN. Most notable in this regard may be the location of a subset of W-like cells that occupied a dorso-lateral strip adjacent to the optic tract. This area, also known as the dorsal lateral shell, is distinct from other regions of dLGN because it contains a high concentration of calbindin positive cells and serves as the as the recipient zone for the collilculo-geniculate projection (Reese, 1984; Grubb and Thompson, 2004). This region shares a similar homology to the tecto-recipient zones noted in the C-laminae of carnivores (Demeulemeester et al., 1991) and the konicellular division of some primates (Harting et al., 1991). At least 3 classes of identified direction selective RGCs project to this area: a group of Off-cells that respond to upward motion (Kim et al., 2008; Kim et al., 2010) and two groups of On/Off cells that prefer posterior motion (Huberman et al., 2009; Rivlin-Etzion et al., 2011). Interestingly, these cell types also project to superior colliculus, and

thus may be part of a unique colliculo-geniculate feedback loop that involves information conveyed by these RGC types. Thus, a major challenge of future experiments is to delineate the pattern of retinal convergence that exists between and within different groups of dLGN cells.

Finally it is important to consider how the regional specification of identified cell types in dLGN relates to the functional organization of visual cortex. Most notable was the discovery that X-cells resided primarily within the monocular portion of dLGN while Y-cells were in the binocular segment. Such apparent segregation has important functional implications since thalamocortical afferents from these regions project in parallel to monocular and binocular regions of visual cortex (Caviness and Frost, 1980; Coleman et al., 2009). While the response properties of visual cortical neurons show some evidence of parallel channels especially in the spatiotemporal domain (Gao et al., 2010), it remains unclear how such organization relates to monocular and binocular regions of V1 or to the reported homogeneity of dLGN receptive field properties.

In sum, our experiments provide a potential substrate for parallel organization in the mouse visual system and pave the way for future studies to explore how functional cell class specificity originating in the retina is recapitulated in dLGN and then relayed to visual cortex

Vita

Rana Naja El-danaf was born on July, 24 1984 in Kharkov, Ukraine and is an American citizen. She graduated from John Randolph Tucker High School, Richmond, Virginia in 2002. Graduating Magna Cum Laude, she received her Bachelor of Science in Chemistry and French, with Biology minor from Virginia Commonwealth University, Richmond, Virginia in 2006. She subsequently entered graduate school at Virginia Commonwealth University in 2006 and received her Master of Science in Physiology and Biophysics in 2008.

Publications in Preparation

1. Krahe TE*, **El-Danaf RN***, Dilger EK, Henderson SC, Guido W. Morphologically distinct classes of relay cells exhibit regional preferences in the dorsal lateral geniculate nucleus of the mouse.

2. El-Danaf RN, Krahe TE**,** Fox MA, Dilger EK, Guido W. Developmental remodeling of relay neurons in the dorsal lateral geniculate nucleus (dLGN) of the mouse and the role of retinal innervation.

Awards

Best Abstract Award, Central Virginia Chapter Society for Neuroscience, annual poster session, 2010

Phi Kappa Phi Honor Society, 2010